Theoretical Study of Chemical Vapor Deposition of Transition Metal Compounds

Dissertation
zur
Erlangung des Doktorgrades
der Naturwissenschaften
(Dr. rer. nat.)

dem
Fachbereich Chemie
der Philipps-Universität Marburg
vorgelegt von

Magdalena Siódmiak
aus Olsztyn/Polen

Marburg/Lahn 2001

Vom Fachbereich Chemie der Philipps-Universität Marburg
als Dissertation angenommen am 24.01.2001

Erstgutachter	Prof. Dr. G. Frenking
Zweitgutachter	Prof. Dr. G. Boche
Tag der mündlichen Prüfung:	07.02.2001

This work was completed at the group of Prof. Dr. Gernot Frenking whom I would like to thank for providing an excellent working environment. To Anatoli Korkin I thank very much for very interesting topic of my research and very fruitful cooperation. All my colleagues from AK Frenking I would like to thank for help and time we spent together at the university, and not only there ....

Results of this thesis have been published in following papers:

1. Siodmiak, M; Frenking, G., and Korkin, A. *J. Phys. Chem. A* **2000**, *104*, 1186.
2. Siodmiak, M; Frenking, G., and Korkin, A *Materials Science in Semiconductor Processing* **2000**, *3*, 65.
3. Siodmiak, M; Frenking, G., and Korkin, A *J. Mol. Model.* **2000**, *6*, 413.
4. Umanskii, S. Ya.; Novoselov, K. P.; Minushev, A. Kh.; Siodmiak, M; Frenking, G., and Korkin, A *J. Comp. Chem.* in press.

Table of contents:

1. Introduction

The formation of metal-containing thin-film materials is currently an area of immense interest and research activity. These materials have found increasing application to a wide variety of technological solutions within optoelectronic devices, electronic materials, heterostructures, superconductive materials and device interconnects. Other applications of metal-containing thin films use their high hardness and inertness. Thus one finds these materials in chemically taxed aerospace components, high energy optical systems, high temperature devices or as coating films in cutting tools.

Metal-containing thin films have been prepared traditionally by a number of techniques which can be classified according to the film formation environment: electrolysis (e.g. electrolytical anodisation, electroplating), vacuum (vacuum evaporation, ion beam deposition, molecular beam epitaxy, ion implantation), plasma (sputtering deposition, ion plating), liquid phase (liquid-phase epitaxy), solid state (solid-state epitaxy), and chemical vapor (substrate chemical vapor conversion, chemical vapor deposition). Each of these techniques due to its advantages and limitations is used in fabrication of metal-containing thin films for different applications. In semiconductor devices and integrated circuits technology the best quality thin films with very low defect density are provided by Chemical Vapor Deposition (CVD).

The technique of CVD is a relatively old chemical process, dating from the 1880s in the productions of carbon filaments for the incandescent lamp industry.[1] Shortly after the initial use of CVD for making carbon films, organometallic compounds found application in the formation of metal containing solid-state materials in vapor-phase processes.[2]

Chemical vapor deposition, as its name implies, is a processes in which gaseous species are employed in formation of stable solid state materials. In the CVD process chemical reactions may occur in the gas phase, at the surface of the substrate, or both. After entering the depositon zone gaseous reactants start to diffuse to the substrate due to the mass gradient. Since they become heated at some point of their transport, reaction often begin already in the gas phase rather than occurring entirely on the substrate surface. The products of these reactions are usually more reactive with the substrate than are the source gases themselves. The next step during CVD process is adsorption of reactants or products of gas phase reaction at the surface. To describe adsorption few steps must be considered (Fig. 1.1). First, a molecule is trapped in a weak-adsorbed state known as a physisorption. The physisorbed molecule is mobile at the surface and may desorb after a while by gaining enough energy or may undergo a further interaction consisting of formation chemical bonds with the surface atoms, called chemisorption. Chemisorption involves sharing electrons in new molecular orbitals and thus is much stronger than physisorption, which involves only dipole interactions. Chemisorbed molecules can further migrate along the surface and are finally incorporated to the lattice. On the other side, byproducts of surface reactions and physisorbed molecules can desorb and diffuse to the bulk of the gas stream and leave the deposition zone.

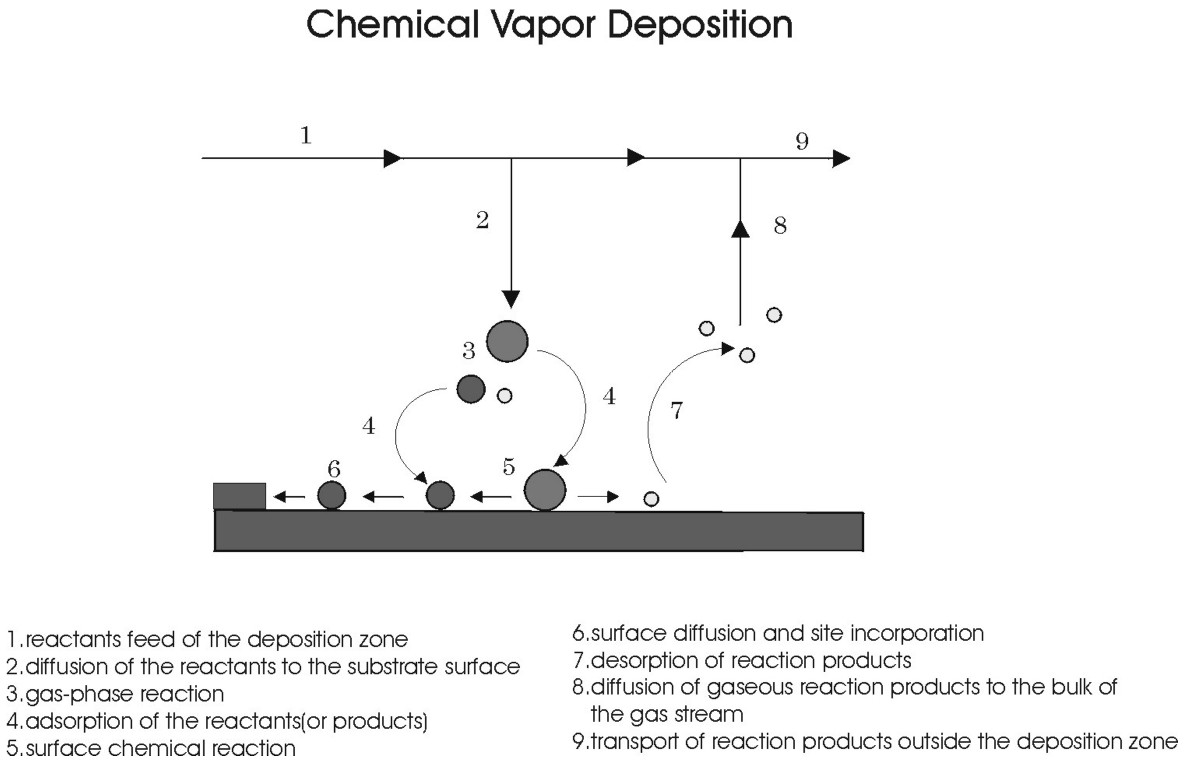

Fig.1.1 CVD scheme

The advantages of CVD technique over other deposition methods include better kinetic control of deposition, selective area and pattern deposition capabilities, controllable stoichimetric composition of films, formation of high purity materials, superior thin film uniformity and step coverage, a wide pressure range, and facility for large scale production processes.

The optimization of the CVD condition for obtaining higher quality films, better conformity or higher (optimal) film growth rate requires knowledge of the deposition chemistry, which can be obtained from specially designed experiments or/and modeling and simulation. Experiments provide the most reliable results, but they are expensive and time and material consuming. Recent developments of quantum chemical methods, particularly density functional theory (DFT), and fast progress in software and hardware development have provided first principles (*ab initio*) theoretical quantum chemistry approaches as an alternative to experiments and empirical simulations in some areas of CVD modeling.

This work presents quantum chemical studies of initial processes involved in CVD of two materials: tantalum pentoxide and titanium nitride, both being detailed described in the course of the work. Quantum chemical methods and computational techniques applied in the reported calculations are briefly introduced in chapter 2. Thermochemistry and mechanism of selected dihydrochlorination and dehydration reactions occurring in the $TiCl_5/H_2O$ system, which lead to the deposition of Ta_2O_5 are discussed in chapter 3. Chapter 4 contains study of complex formation, ammonolysis and imido compounds formation reactions present during CVD of TiN from $TiCl_4$ and NH_3. The quantum chemical calculations for this system are extended by kinetic calculations of the leading processes in typical CVD conditions. The solid state calculations of TiN surface together with study of surface chemistry of hydrogen atom are the contents of chapter 4. The work closes with concluding remarks to calculated gas phase and surface processes and a discussion of the application of the obtained results in modeling of entire CVD process.

2. Theoretical background

2.1 Schrödinger equation

According to quantum mechanics, the energy and many properties of stationary state of a molecule can be obtained by solution of the Schrödinger equation[3]:

$$\hat{\boldsymbol{H}}\ \Psi(x) = E\ \Psi(x) \qquad 2.1$$

$\hat{\boldsymbol{H}}$ is the Hamilton operator which represents the total energy of the system, E, an eigenvalue of the Hamiltonian is a numerical value of the energy. The wave function $\Psi(x)$ is the eigenfunction of $\hat{\boldsymbol{H}}$ and in stationary case depends on the cartesian space coordinates $\boldsymbol{r}$ and spin coordinates ω of all particles.

The Hamiltonian $\hat{\boldsymbol{H}}$, like the energy in classical mechanics is the sum of the kinetic $\hat{\boldsymbol{T}}$ and the potential $\hat{\boldsymbol{V}}$ parts and thus can be written in atomic units as:

$$\hat{\boldsymbol{H}} = \frac{1}{2}\sum_{i}^{n}\nabla_i^2 - \frac{1}{2}\sum_{A}^{N}\frac{1}{\mathrm{M}_A}\nabla_A^2 - \sum_{i}^{n}\sum_{A}^{N}\frac{\mathrm{Z}_A}{r_{iA}} + \sum_{i}^{n}\sum_{j>i}^{n}\frac{1}{r_{ij}} + \sum_{A}^{N}\sum_{B>A}^{N}\frac{\mathrm{Z}_A\mathrm{Z}_B}{R_{AB}} \qquad 2.2$$

M_A is the ratio of the mass of nucleus A to the mass of an electron and Z_A is the atomic number of the nucleus A; r_{ij}, r_{iA} and R_{AB} are the distance between ith and jth electrons, between ith electron and the nucleus A, and between the nucleus Ath and Bth, respectively. The first two terms in this expression are operators for the kinetic energy of electrons and nuclei, respectively. The third term describes the electrostatic attraction between nuclei and electrons, while the last two terms represent the electrostatic repulsion between electrons and between nuclei, respectively. This Hamiltonian is a nonrelativistic. It becomes inappropriate as the velocities of particles approach the velocity of light.

Since nuclei are much heavier than electrons they move more slowly, thus it is a reasonable approximation to consider that the electron distribution depends only on the positions of the nuclei. Quantitatively, this approximation introduced by Born and Oppenheimer[4] may be formulated by writing the Schrödinger equation for electrons in the field of fixed nuclei:

$$\hat{\boldsymbol{H}}^{el}\ \Psi^{el}(x,\boldsymbol{R}) = E^{tot}(\boldsymbol{R})\ \Psi^{el}(x,\boldsymbol{R})$$

Ψ^{el} is the electronic wave function which depends explicitly on the electronic coordinates x and parametrically on the nuclear coordinates $\boldsymbol{R}$. The total energy E^{tot} for fixed nuclei includes the electronic energy and the constant nuclear repulsion. The electronic Hamiltonian is:

$$\hat{\boldsymbol{H}}^{el} = \hat{\boldsymbol{T}}^{el} + \hat{\boldsymbol{V}} \tag{2.3}$$

where $\hat{\boldsymbol{T}}^{el}$ is the kinetic energy of the electrons and $\hat{\boldsymbol{V}}$ is the coulomb potential as previously.

2.2 Hartree-Fock approximation

The Schrödinger equation for many-electron systems can be solved only approximately. The main approximation follows the assumption that all electrons in the system posses individual one-electron wave functions which are called spin orbitals. The many-electron wave function can be written then as a single Slater determinant[5]:

$$\Psi_0(x_1, x_2, \dots, x_N) = \frac{1}{\sqrt{N!}} \begin{vmatrix} \chi_i(x_1) & \chi_j(x_1) & \dots & \chi_k(x_1) \\ \chi_i(x_2) & \chi_j(x_2) & \dots & \chi_k(x_2) \\ \vdots & \vdots & & \\ \chi_i(x_N) & \chi_j(x_N) & \dots & \chi_k(x_N) \end{vmatrix} \tag{2.4}$$

Or in short form:

$$|\Psi_0\rangle = |\chi_1\chi_2 \ldots\ldots \chi_a\chi_b \ldots\ldots \chi_N\rangle \qquad 2.5$$

This asymmetric form of the wave function Ψ_0 is the best approximation to the ground state of the N-electron system described by the Hamiltonian $\hat{\boldsymbol{H}}$. According to the variational principle[6] this approximate wave function has an energy which is above or equal to the exact energy of the system:

$$E_0 = \langle \Psi_0 | \hat{\boldsymbol{H}} | \Psi_0 \rangle \geq E_{exact} \qquad 2.6$$

This characteristic can be used to determine optimal spin orbitals in Ψ_0 by minimizing the electronic energy E_0. A set of N equations derived for this purpose was proposed by Hartree and Fock[7] in the form of:

$$\hat{\boldsymbol{f}}\,(i)\,\chi\,(x_i) = \varepsilon\,\chi(x_i) \qquad 2.7$$

where $\hat{\boldsymbol{f}}$ is an effective one-electron energy operator, called Fock operator. It describes via the $\hat{\boldsymbol{h}}$ operator the kinetic energy of the electron and the attraction to all nuclei. The repulsion to all the other electrons is expressed via the Coulomb operator $\hat{\boldsymbol{J}}$ and the exchange operator $\hat{\boldsymbol{K}}$.

$$\hat{f}(i) = \hat{h}(i) + \sum_{j=1}^{N} \left(\hat{J}(j) - \hat{K}(j) \right) \qquad 2.8$$

where:

$$\hat{\boldsymbol{h}}(i) = -\frac{1}{2}\nabla_i^2 - \sum_{A} \frac{Z_A}{r_{iA}} \qquad 2.9$$

The two electrons operators $\hat{\boldsymbol{J}}$ and $\hat{\boldsymbol{K}}$ are defined by their effect on a spin orbital as follows:

$$\hat{\boldsymbol{J}}_b(x_i)\chi_a(x_i) = \int dx_j \chi_b^*(x_j)\frac{1}{r_{ij}}\chi_b(x_j)$$

$$\hat{\boldsymbol{K}}_b(x_i)\chi_a(x_i) = \int dx_j \chi_b^*(x_j)\frac{1}{r_{ij}}\chi_a(x_j) \qquad 2.10$$

The idea of the Hartree-Fock approximation is thus to replace the complicated many-electron problem by a one-electron model in which electron-electron repulsion is treated in average way. This is a consequence of the assumption that the spatial distribution of electrons is described by a set of orbitals and correlation between their motion is not included.

The specific spin orbitals can only be determined if all the other occupied orbitals are known. Because of this the Hartree-Fock equations are not linear and must be solved iteratively. The procedure of solving the Hartree-Fock equation is called the self-consistent-field (SCF) method. For an initial set of spin orbitals one calculates the avarage interaction of each electron with the other electrons and solves the eigenvalue equation for a new set of spin orbitals. These new spin orbitals are used to obtain a new avarage field for each electron. The procedure is repeated until the self-consistancy is reached and spin orbitals used to construct the Fock operator are the same as its eigenfunctions.

The Hartree-Fock approximation to many-electron systems is an important starting point for more accurate approximations, which include the effect of correlation between electrons.

2.3 Basis sets expansion and pseudopotentials

A further approximate method for solving the Schrödinger equation is based on the introduction of a basis set. An unknown function, such as a molecular orbital Ψ_i can be expressed as a linear combination of a finite set of N one-electron basis functions ϕ_i:

$$\Psi_i = \sum_{\mu=1}^{\mathrm{N}} c_{\mu i}\phi_\mu \qquad 2.11$$

where $c_{\mu i}$ are the molecular orbital expansion coefficients. This approach is not an approximation if the basis set is complete. A complete basis requires an infinite number of basis functions what in actual calculation cannot be fulfilled. In simple versions of molecular orbital theory, a finite number of atomic orbitals of the constituent atoms is used as basis functions. Such a treatment is described as *linear combination of atomic orbitals theory* (LCAO).[8]

To provide a basis set that is well defined for any atoms configuration, it is convenient to define a particular set of basis functions associated with each atom. Such functions may have symmetry properties of atomic orbitals and may be classified as *s*, *p*, *d*, *f* etc. types according to their angular properties. There are two types of atomic basis functions commonly used in electronic structure calculations. *Slater-type* atomic orbitals[9] (STOs) are of the form:

$$\chi_{\zeta,n,l,m}(r,\theta,\varphi) = NY_{l,m}(\theta,\varphi)r^{n-1}\mathrm{e}^{-\zeta r} \qquad 2.12$$

where r is the distance between the nucleus and the electron, N is a normalization constant and $Y_{l,m}$ are the spherical harmonic functions of the polar angles θ and φ. The exponential radial part of STOs ensures rapid convergence with increasing number of functions. However, STOs are not well suited to numerical work required for calculations of two-electron integrals and thus their use is limited to calculations of atomic and diatomic systems.

The second type of basis consists of *gaussian-type* atomic functions[10] (GTO). In normalized form they are written as follows:

$$\chi_{\zeta,n,l,m}(r,\theta,\varphi) = NY_{l,m}(\theta,\varphi)r^{(2n-2-l)}\mathrm{e}^{-\zeta r^2} \qquad 2.13$$

GTO are less satisfactory than STOs as a representation of atomic orbitals, particularly because they do not describe properly the behavior near the nucleus and fall off too rapidly far from the origin. Nevertheless, they have an important advantage that all integrals in computations can be evaluated explicitly and therefore are preferred in terms of computational efficiency.

A third possibility is to use numerically generated atomic basis sets. In this case basis functions χ_μ are given numerically as values on an atom centered spherical polar mesh. The angular portion of each function is the appropriate spherical harmonic $Y_{lm}(\theta,\varphi)$ and the radial portion F(**r**) is obtained by solving atomic HF equations numerically. The use of the exact spherical atomic orbitals has several advantages. For one, the molecule can be dissociated exactly to its constituent atoms. Due to the quality of these orbitals also an excellent description of weak bonds is possible.

The formation of chemical bonds and most physical properties are governed by the valence electrons of atoms, not by the core electrons of inner closed shells. For systems involving heavy-atoms it is necessary to use a large number of basis functions to expand the orbitals, otherwise valence shells will not be properly described. This implies in the LCAO approximation a large number of two-electron integrals, which scales with N^4, where N is the number of basis functions. Additionally relativistic effects must be taken into account for accurate calculations of molecules involving atoms from lower half of the periodic table. Both problems can be solved by introducing pseudopotentials to represent chemically innert core electrons.

There are two qualitatively different methods for deriving pseudopotentials. One is based on the concept of a core pseudowave function which represents a reasonable repulsive potential to the valence region.[11] This potential is fitted to a set of analytical functions, e.g. of the form of Gaussian functions:

$$U_{ECP}(r) = \sum_i a_i r^{n_i} \mathrm{e}^{-\alpha_i r^2} \qquad 2.14$$

where a_i, n_i and α_i depand on the angular momentum. This type of pseudopotential is refered as *effective core potential.*

The other approach rests on a *model potential*, which mimics the potential of the core electrons. Introducing so-called energy level shift operator assures on the other hand that the the correct nodal structure of valence orbitals is preserved.

2.4 Møller-Plesset perturbation theory

The main deficiency of Hartree-Fork theory is the inadequate treatment of the correlation between motions of electrons due to replacement of a real electron-electron interaction by an average interaction. In particular, a single-determinant wave function does not take into account a correlation between electrons with opposite spin. These limitations imply that the calculated Hartree-Fock energies are above the exact values. The difference between the HF and exact nonrelativistic energy is the correlation energy[12]:

$$\mathrm{E}_{corr}=\varepsilon_{exact} - \mathrm{E}_{HF} \tag{2.15}$$

One of the systematic procedure for finding the correlation energy is the perturbation theory of Møller and Plesset,[13] closely related to the many-body perturbation theory. In this approach the total Hamiltonian of the system is divided into two parts: the unperturbated zero-order operator $\hat{\boldsymbol{H}}_0$, and the perturbation operator $\hat{\boldsymbol{V}}$:

$$\hat{\boldsymbol{H}}_\lambda = \hat{\boldsymbol{H}}_0 + \lambda\hat{\boldsymbol{V}} \tag{2.16}$$

where $\hat{\boldsymbol{H}}_0$ is the Hartree-Fock Hamiltonian:

$$\hat{\boldsymbol{H}}_0 = \sum_i f(i) = \sum_i [h(i) + \upsilon^{HF}(i)] \tag{2.17}$$

and λ is a parameter, which controls the strength of the perturbation.

The eigenfunction Ψ_λ and the eigenvalue E_λ corresponding to the Hamiltonian $\hat{\boldsymbol{H}}_\lambda$ may be written as a Taylor expansion in powers of the perturbation parameter λ as follows:

$$\begin{aligned} \Psi_\lambda &= \Psi^{(0)} + \lambda\Psi^{(1)} + \lambda^2\Psi^{(2)} + \ldots \\ E_\lambda &= E^{(0)} + \lambda E^{(1)} + \lambda^2 E^{(2)} + \ldots \end{aligned} \tag{2.18}$$

The leading terms in these expansions are the eigenfunction Ψ_0

$$\Psi^{(0)} = \Psi_0 \tag{2.19}$$

which is Hartree-Fock wave function of $\hat{\boldsymbol{H}}_{\boldsymbol{0}}$ Hamiltonian and the energy $E^{(0)}$:

$$\begin{gathered} E^{(0)} = \sum_{i}^{occ} \varepsilon_i \\ E^{(0)} + E^{(1)} = \int \ldots \int \Psi_0 \hat{H} \Psi_0 dx_1 dx_2 \ldots dx_n \end{gathered} \tag{2.20}$$

with ε_i as the one-electron energies. The Møller-Plesset energy to first-order is thus the Hartree-Fock energy. The first order contribution to the wave function is:

$$\Psi^{(1)} = \sum_{n>0} \left(E_0 - E_n\right)^{-1} V_{n0} \; + \Psi_{\mathrm{n}} \tag{2.21}$$

where $V_{n0} = \langle 0 | \hat{\boldsymbol{V}} | \mathrm{n} \rangle$ are matrix elements involving the perturbation operator $\hat{\boldsymbol{V}}$.

The first correction to the Hartree-Fock energy occurs in the second order of perturbation theory. The general result for the second-order energy is:

$$\mathrm{E}^{(2)} = \sum_{n}{}' \left(E_0 - E_n\right)^{-1} \left|V_{n0}\right|^2 \tag{2.22}$$

where summation runs over all but the ground state of the system. The energy $E^{(2)}$ can also be expressed as a sum of contributions from each pair of electrons in occupied orbitals *a,b* which are promoted to virtual orbitals *r,s*:

$$E^{(2)} = \sum_{a<b}^{occ}\sum_{b}^{occ}\sum_{r<s}^{vir}\sum_{s}^{vir}\frac{\left|\langle ab\|rs\rangle\right|^{2}}{\varepsilon_a + \varepsilon_b - \varepsilon_r - \varepsilon_s} \qquad 2.23$$

This represents the simplest approximate expression for the correlation energy.

The second order Møller-Plesset[14] (MP2) energy typically accounts for ~80-90% of correlation energy. The fourth-order energy matches 95-98%. Calculating higher-order corrections becomes computationally very expensive.

The main limitation of perturbation methods is the assumption that the zero-order wave function is a reasonable approximation to the real wave function, i.e. that the perturbation operator is sufficiently small. The worse the HF function which describes the system, the larger the corrections and the higher order terms must be included to achieve a desired level of accuracy.

2.5 Coupled Clusters methods

As it was presented in the previous chapter, perturbation methods include all types of corrections (single, double, triple etc.) to the reference function to a given order (2, 3, 4 etc.). Coupled Cluster methods[15] are based on the other idea – including all corrections of a given type to infinite order. For this purpose the cluster operator T is introduced:

$$\mathbf{T} = \mathbf{T}_1 + \mathbf{T}_2 + \mathbf{T}_3 + \ldots + \mathbf{T}_N \qquad 2.24$$

The operator $\mathbf{T}_i$ acting on a HF reference wave function Φ_0 generates all i^{th} excited Slater determinants according to the template:

$$\begin{aligned} \mathbf{T}_1\Phi_0 &= \sum_{i}^{\mathrm{occ}}\sum_{a}^{\mathrm{vir}} t_i^a \Phi_i^a \\ \mathbf{T}_2\Phi_0 &= \sum_{i<j}^{\mathrm{occ}}\sum_{a<b}^{\mathrm{vir}} t_{ij}^{ab} \Phi_{ji}^{ab} \end{aligned} \qquad 2.25$$

with expansions coefficients t, which are referred in this approach as amplitudes. Applying the **T** operator we can introduce the coupled cluster wave function as:

$$\Psi_{cc} = e^{\mathbf{T}}\Phi_0 \qquad 2.26$$

with

$$e^{\mathbf{T}} = \mathbf{1} + \mathbf{T} + \frac{1}{2}\mathbf{T}^2 + \frac{1}{6}\mathbf{T}^3 + \ldots = \qquad 2.27$$

$$\mathbf{1} + \mathbf{T}_1 + \left(\mathbf{T}_2 + \frac{1}{2}\mathbf{T}_1^2\right) + \left(\mathbf{T}_3 + \mathbf{T}_2\mathbf{T}_1 + \frac{1}{6}\mathbf{T}_1^3\right) + \left(\mathbf{T}_4 + \mathbf{T}_3\mathbf{T}_1 + \frac{1}{2}\mathbf{T}_2^2 + \frac{1}{2}\mathbf{T}_2\mathbf{T}_1^2 + \frac{1}{24}\mathbf{T}_1^4\right) + \ldots$$

Having the HF reference function Φ_0 and using above expressions for operators $\mathbf{T}_i$ (eq. 2.25) one obtains the coupled cluster wave function Ψ_{cc} and corresponding energy E_{cc} by solving the set of equations for amplitudes t_i^j, t_{ij}^{ab}, t_{ijk}^{abc}, ...

In the latter form of the exponential operator $e^{\mathbf{T}}$ (eq.2.27) all terms are collected according to the excitation they generate. The first term generates the reference wave function and the second all singly excited states. Each of the operators in following parenthesis generates all the excited states of the corresponding higher order. According to the Brillouins theorem,[16] which states that singly excited determinants do not interact directly with HF reference determinant, the effect of the operator $\mathbf{T}_1$ will be small, although still not zero since singles enter indirectly via higher excited states. It is known that the most important contribution comes from double excitations $\mathbf{T}_2$, not only in case of coupled cluster methods. The contribution of the operator $\mathbf{T}_3$ is also quite significant. This implies that in higher excitations all terms appearing as powers and products of operators $\mathbf{T}_2$ and $\mathbf{T}_3$ are dominating. Higher order terms $\mathbf{T}_i$ where i>4 have small effect, although they become more and more important as the number of electrons increases. Considering all $\mathbf{T}_N$ operators is anyway impossible for all but the smallest systems, and several approximations of coupled cluster approach had to be introduced. The lowest level approximation limits cluster operator only to $\mathbf{T}=\mathbf{T}_2$ and is referred as Coupled Cluster Doubles (CCD). The slightly more demanding CCSD approach with $\mathbf{T}=\mathbf{T}_1 + \mathbf{T}_2$ results in a more complete model. The main limitation of this method is the neglect of triples associated with $\mathbf{T}_3$ operator. Including directly the operator $\mathbf{T}_3$ in the CCSDT model requires however much more computational effort. As an alternative the triple contribution can be calculated using perturbation theory which results in the CCSD(T) approach.

2.6 Density Functional Theory

In contrast to the Hartree-Fock picture, which begins conceptually with a description of individual electrons interacting with the nuclei and all other electrons in the system, *density functional theory* starts with a consideration of the entire electron system. The basis for this theory is the Hohenberg-Kohn theorem,[17] which states that all ground-state properties are functions of the electron density ρ. The total energy functional $E_t[\rho]$ may be decomposed then into three contributions, a kinetic energy $T[\rho]$, Coulomb energy $U[\rho]$ due to a classical interactions among all charged particles in the system, and a term called exchange-correlation energy $E_{xc}[\rho]$ that captures all many-body interactions.

$$E_t[\rho] = T[\rho] + U[\rho] + E_{xc}[\rho] \qquad 2.28$$

This decomposition is formally exact, but the actual expression for the many-body exchange and correlation interaction is unknown. When Kohn and Sham introduced splitting of the kinetic energy into two parts,[18] one of which can be calculated exactly, and other being a small correction term, the exchange-correlation part was further enlarged by the remaining kinetic energy which cannot be calculated explicitly. The difference between DFT methods is the choice of the functional form of the exchange-correlation energy.

In the *Local Density Approximation (*LDA), the exchange-correlation energy is taken from the known results of the many electron interactions in homogeneous electron gas. The assumption is made that the density is a locally slowly varying function. The extension of LDA distinguishes α and β spin densities, which in general may not be equal. This approach is referred as *Local Spin Density Approximation* (LSDA). Both methods are exact for perfect metals.

Application to other systems requires a model which is developed for a non-uniform electron gas. In so called *non-local* approximation the exchange and correlation energies E_x and E_c, depend not only on the electron density but also on its gradient:

$$\mathrm{E}_{xc}(\rho) \cong \mathrm{E}_{xc}^{non-loc}(\rho,\nabla\rho) = \mathrm{E}_{x}^{non-loc}(\rho,\nabla\rho) + \mathrm{E}_{c}^{non-loc}(\rho,\nabla\rho) \qquad 2.29$$

The use of gradient corrections has little influence on local properties such as bond lengths or vibration frequencies, but leads to a significant improvement in global changes in the energy.

Hybrid methods define exchange energy as a suitable combination of LSDA, gradient corrections and exact exchange given by the Hartree-Fock theory. Correlation energy is taken also from LSDA approach together with gradient corrections. Introduced by Becke the B3LYP[19] functional is an example of such hybrid model where:

$$\mathrm{E}_{xc}^{B3LYP} = (1-c_0)\mathrm{E}_{x}^{LDA} + c_0\mathrm{E}_{x}^{HF} + c_x\Delta\mathrm{E}_{x}^{B88} + (1-c_c)\mathrm{E}_{c}^{VWN3} + \mathrm{c_c}\mathrm{E}_{c}^{LYP} \qquad 2.30$$

One of the form of exchange-correlation energy can be used further to determine a set of orthogonal orbitals which minimize the energy in Kohn-Sham equations:

$$\left(-\frac{1}{2}\sum_i \nabla_i^2 - \sum_i\sum_A \frac{Z_A}{r_{iA}} + \int \frac{\rho(i)}{r_{ij}}dx_i + \upsilon_{xc}(j)\right)\psi_i = \varepsilon_i\psi_i \qquad 2.31$$

where the exchange-correlation potential υ_{xc} is given as the derivative of the energy with respect to the density:

$$\upsilon_{xc}(\mathbf{r}) = \frac{\partial E_{xc}[\rho]}{\partial\rho(\mathbf{r})} \qquad 2.32$$

The Solution of Kohn-Sham equations (eq.2.31) is obtained in the same procedure as in case of the Hartree-Fock method. The important difference between HF and DFT is that DFT include correlation energy, at a computational effort similar to that of calculating the uncorrelated HF energy. If the exact $E_{xc}[\rho]$ was known, DFT would provide the exact total energy.

2.7 Periodic systems and Bloch's theorem

Studies of the electronic structure of a crystal are based on finding the wave function for an infinite number of electrons. This wave function must be expressed in terms of an infinite basis because of the infinite extent of the system. The large number of atoms in a crystal (of the order of 10^{23}) implies that quantum calculations of the solid state properties are not currently feasible because of the limitations of computer hardware. This problem can be overcome by performing calculations on periodic systems. Periodic conditions are determined by a translational symmetry of a macrocrystal and allow calculations of an infinite piece of matter to be reduced to calculations of so called unit cell. The unit cell can be defined in terms of three real-space primitive translation vectors $\mathbf{R}_1$, $\mathbf{R}_2$ and $\mathbf{R}_3$. (Fig.2.1). A general vector in the lattice can be written then as:

$$\mathbf{R}=n_1\mathbf{R}_1+n_2\mathbf{R}_2+n_3\mathbf{R}_3, \qquad 2.33$$

where n_1, n_2 and n_3 are arbitrary integers.

In the study of periodic systems, extensive use is made of the concept of the reciprocal lattice. A set of primitive reciprocal-space translational vectors $\mathbf{G}_i$ can be defined using real-space primitive vectors according to the relation:

$$\mathbf{R}_i \bullet \mathbf{G}_j=2\pi\delta_{ij} \qquad 2.34$$

for i and j in the range 1 to 3. They can also be written in explicit form, e.g.:

$$\mathbf{G}_1 = 2\pi \frac{\mathbf{R}_2 \times \mathbf{R}_3}{\mathbf{R}_1 \cdot (\mathbf{R}_2 \times \mathbf{R}_3)} \qquad 2.35$$

Similar expressions hold for $\mathbf{G}_2$ and $\mathbf{G}_3$, which can be obtained by cyclic permutation of the subscripts.

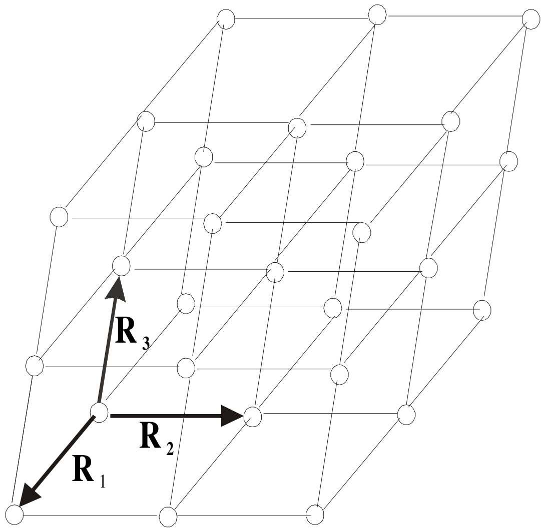

Fig.2.1 Crystal, unit cell, and basis vectors of lattice

Solutions of the Schrödinger equation for a periodic structure obey Bloch's theorem, which states that the wave function in a periodic system can be written as the product of a wave-like part and a cell-periodic part:

$$\Psi_i(\mathbf{r}) = \exp[i\,\mathbf{k} \cdot \mathbf{r}]\,u_i(\mathbf{r}) \qquad 2.36$$

The cell-periodic part can be written as a discrete sum of plane-waves with reciprocal lattice vectors

$$u_i(\mathbf{r}) = \sum_{\mathbf{G}} c_{i,\mathbf{G}} \exp[i\mathbf{G} \cdot \mathbf{r}] \qquad 2.37$$

so that each wave function, commonly referred to as Bloch function, can be given as

$$\Psi_i(\mathbf{r}) = \sum_{\mathbf{G}} c_{i,\mathbf{k}+\mathbf{G}} \exp[i(\mathbf{k}+\mathbf{G}) \cdot \mathbf{r}]. \qquad 2.38$$

On invoking Bloch's theorem the Schrödinger equation can be regarded as restricted to a single unit cell, with an extended nature of the orbitals described by boundary conditions at the edges of the cell. Thus any vectors, differing from each other by an integral number of periods of the reciprocal lattice, correspond to one and the same Bloch function, so that the **k** vectors from any segment of the reciprocal lattice length are sufficient to describe all Bloch functions. It is convenient to take as this segment the one that is symmetrically located at both sides of the coordinate origin of the reciprocal lattice. This segment, containing *N* vectors of **k** space, is called the first Brillouin zone.

In distinction to the molecular case where the spectrum of eigenvalues is discrete and each eigenfunction can be given a discrete label, Bloch functions are characterized by a discrete label, called the band-index, plus a continuous label, the Bloch wavevector **k**.

2.8 The k-points integration

The Bloch's theorem implies that the avarage for some operator $\hat{Q}$ over all wavefunctions can be written as:

$$Q = \frac{\Omega_{\mathbf{cell}}}{(2\pi)^3} \int_{\mathbf{BZ}} Q_{\mathbf{k}} \mathbf{d}^3\mathbf{k} \qquad 2.39$$

where Ω_{cell} is the volume of a unit cell and:

$$Q_{\mathbf{k}} = \left\langle \Psi_{\mathbf{k}n} \middle| \hat{Q} \middle| \Psi_{\mathbf{k}n} \right\rangle \qquad 2.40$$

Calculations of the total energy require several integrals in reciprocal space. In practice, a sampling technique must be used to approximate these integrals by numerical summation over a finite number of k points. The primary special k-point approach to select an optimal set of points that the greatest possible accuracy is achieved from the number of points used was proposed by Monkhorst and Pack.[20] The uniform mesh of k-points in the Brillouin zone to sample the $Q_{\mathbf{k}n}$ function is generated by a set of three integers N_1, N_2 and N_3. These integers determine the density of k-points in each of the primitive reciprocal-lattice directions. A general point in the mesh is then given by:

$$\mathbf{k}_{rst}=u_{1r}\mathbf{G}_1+u_{2s}\mathbf{G}_2+u_{3t}\mathbf{G}_3 \qquad 2.41$$

with:

$$u_{ip} = \frac{(2p-N_i-1)}{2N_i} \qquad 2.42$$

where p runs from 1 to N_i. This mesh defines $N_1 \cdot N_2 \cdot N_3$ k-points in the full zone. Thus, the average for operator is replaced by a sum over a discrete set of k-points:

$$Q = \frac{1}{N_1 N_2 N_3} \sum_{\mathrm{rst}} Q_{\mathbf{k}_{rst}} \qquad 2.43$$

The quality of the k-point set can be quantified in terms of a real-space cutoff. A reciprocal-space periodic function, such as $Q_{\mathbf{k}}$, has a representation as a real-space Fourier series. We might write:

$$Q_{\mathbf{k}} = \sum_{\mathbf{R}} B_{\mathbf{R}} e^{i\mathbf{k}\cdot\mathbf{R}} \qquad 2.44$$

where $B_{\mathbf{R}}$ are the expansion coefficient, which fall off quite rapidly as $|\mathbf{R}|$ increases. The shortest $|\mathbf{R}|$ as for which the error in the estimate of Q approaches 0 is an estimate of the quality of the Monkhorst-Pack mesh. The quality of this representation can be verified by increasing the density of k-points used in the mesh. Nonmetallic systems typically require an order of magnitude fewer points than metallic ones because electronic properties of nonmetals vary much more slowly in the Brillouin zone.

2.9 Chemical equilibrium

An established method for evaluating chemical equlibrium is the element-potential method, which follows the assumption that the gas-phase is a mixture of ideal gases. The basic theory for this method of determining equilibrium is based on the minimization of Gibbs free energy. The Gibbs function of a system is:

$$G = \sum_{k=1}^{K} \overline{g}_k N_k \qquad 2.45$$

where $\overline{g}_k$ is the partial molar Gibbs function and N_k is the number of moles of each species k in the system. K is the total number of species. For ideal-gas mixtures the partial molar Gibbs functions are given by:

$$\overline{g}_k = g_k(T,P) + RT \ln X_k \qquad 2.46$$

where $g_k(T,P)$ is the Gibbs function for the pure species k, evaluated at the system temperature T and pressure P; R is the universal gas constant; and X_k is the mole fraction of the k^{th} species.

The equilibrium solution at a given temperature and pressure is the distribution of N_k of the different components that minimizes the system Gibbs function, G. The atomic population constraints are:

$$p_j = \sum_{k=1}^{K} n_{jk} N_k \qquad j=1,\dots, M \qquad 2.47$$

where n_{jk} is the number of the j^{th} atoms that appear in the k^{th} molecule, p_j is the total population of the j^{th} atom in the system given in moles, and M designates the total number of different elements that are present in the system.

2.10 Well-mixed reactor

Simulations of the kinetics of CVD processes can be performed using a model of a well-mixed reactor. In this approach system is described by conservation of mass, energy and species. Fig.2.2 illustrates the conceptual representation of a reactor chamber.

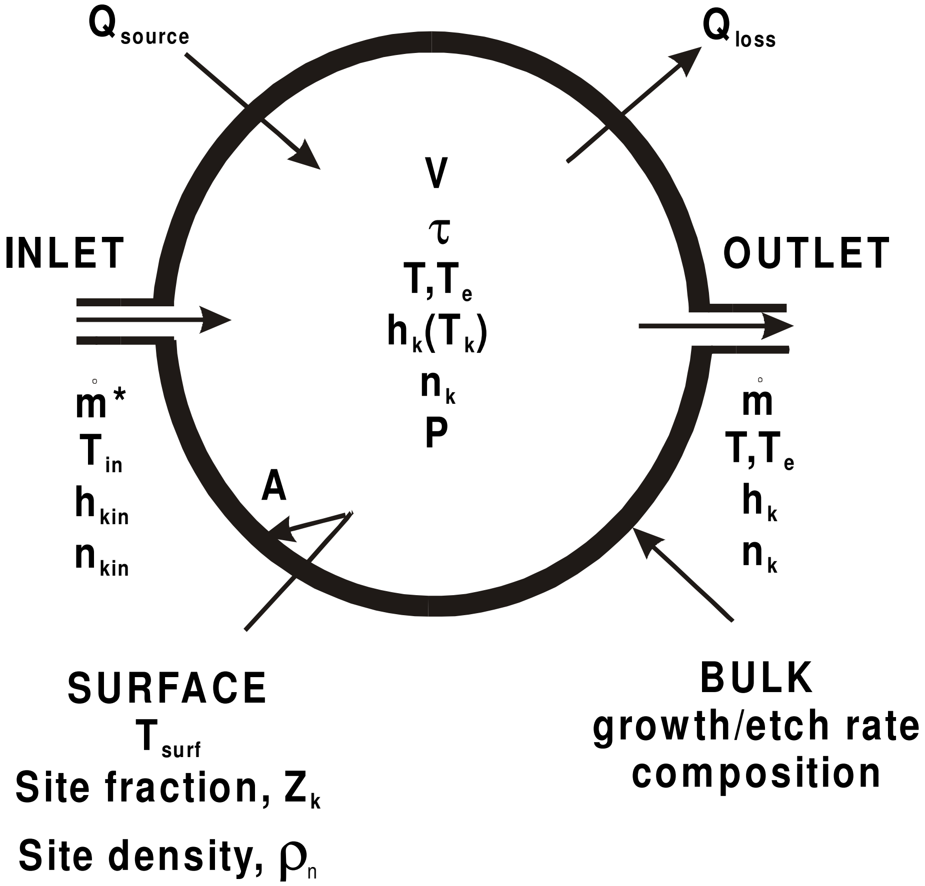

Fig 2.2 Schematic represenatation of a well-mixed reactor

A steady flow of reactants is introduced with a given species composition $n_{k\mathrm{in}}$ and temperature $T_{k\mathrm{in}}$. The mass flow rate into the reactor, $\dot{m}^*$, may not be equal to the mass flow rate out of the reactor, $\dot{m}$, due to deposition or etching of surface materials. The system is characterized additionally by h_k – specific enthalpy of k^{th} species, volume V, residence time τ, surface area of all materials in the reactor A, electron temperature T_e and specified pressure P.

The consideration starts with global mass conservation in the reactor volume, where the time-rate of change of the mass in the reactor is equal to the difference between the mass flow in and the mass flow out, plus any material that is added to or substracted from the surface within the chamber. The equation is stated as:

$$\frac{d(\rho V)}{dt} = \dot{m}^* - \dot{m} + \sum_{m=1}^{M} A_m \sum_{k=1}^{K_g} \dot{s}_{k,m} W_k \qquad 2.48$$

where ρ is the mass density, A_m is the surface area of the m^{th} material defined within reactor, and is the molar surface production rate of k^{th} species on the m^{th} material per unit surface area. W_k denotes molecular weight of k^{th} species. There are K_g gas-phase species and M materials in the system.

The time-dependent equation for mass conservation of each gas-phase species, ignoring the implicit time dependance of ρ through it dependance on the temperature and molecular weight, is:

$$pV\frac{d(Y_k)}{dt} = \dot{m}^*(Y_k^* - Y_k) + \dot{\omega}_k W_k V + \sum_{m=1}^{M} \dot{s}_{k,m} W_k A_m - Y_k\left(\sum_{m=1}^{M} A_m \sum_{j=1}^{K_g} \dot{s}_{j,m} W_j\right) \qquad 2.49$$

$$for \;\; k=1,...,K_g$$

In this equation Y_k is the mass fraction of the k^{th} species and $\dot{\omega}_k$ is the molar rate of production of the k^{th} species by gas-phase chemical reaction per unit volume. The subsript * indicates inlet stream quantities.

The nominal residence time τ in the reactor is related to the reactor volume and the inlet mass flow rate as follows:

$$\tau = \frac{\rho V}{\dot{m}^*} \tag{2.50}$$

Density ρ is related to the pressure, gas temperature and electron temperature through the multi-fluid ideal gas equation of state.

References

[1] Sawyer, W.E., and Mann, A. *U.S. Patent*, **1880**, *229*, 335.

[2] Mond, L., Langer,C.; Quincke, F. *J. Chem. Soc.* **1890**, *57*, 749.

[3] Schrödinger, E. a) *Ann. Physik*, **1926**, *79*, 361 b) *ibid* **1926**, *80*, 437 c) *ibid* **1926**, *81*, 109.

[4] Born, M.; Oppenheimer, J.R. *Ann. Physik* **1927**, *84*, 457.

[5] Slater, J.C. *Phys. Rev.* **1929**, *34*, 1293 b) *ibid* **1930**, *35*, 509

[6] Eckart, C.E. *Phys. Rev.* **1930**, *36*, 878.

[7] (a) Hartree, D.R. *Proc. Camb. Phil. Soc.* **1928**, *24*, 89, (b) Fock, V. *Z. Phys.* **1930**, *61*, 161.

[8] (a) Roothaan, C.C *Rev. Mod. Phys.* **1951**, *23*, 69, (b) Hall, G.G. *Proc. R. Soc. London* **1951**, *A 205*, 541.

[9] Slater, J.C. *Phys. Rev.* **1930**, *36*, 57.

[10] Boys, S.F. *Proc. Roy. Soc.* **1950**, *A200*, 542.

[11] Cohen, M.L.; Heine, V. *Solid State Phys.* **1970**, *24*, 38.

[12] Löwdin, P.-O. *Rev. Modern Phys.* **1955**, *27*, 1509.

[13] Møller, C.; Plesset, M.S. *Phys. Rev.***1934**, *46*, 618. .

[14] Binkley, J.S.; Pople, J.A. *Int. J. Quantum Chem.* **1975**, *9S*, 229.

[15] (a) Cizek, J.; *J. Chem. Phys.* **1966**, *45*, 4256; (b) Pople, J. A.; Krishnan, R.; Schlegel, H.B.; Binkley, J.S. *Int. J. Quantum Chem.* **1978**, *14*, 545; (c) Bartlett, R.J.; Purvis, G.D. *Ibid.* **1978**, *14*, 561; (d) Purvis, G.D; Bartlett, R.J. *J. Chem. Phys.* **1982**, *76*, 1910; (e) Raghavachari, K.; Trucks, G.W.; Pople, J.A.; Head-Gordon, M. *Chem. Phys. Lett.* **1989**, *157*, 479; (f) Bartlett, R.J.; Watts, J.D.; Kucharski, S.A.; Noga, J. *Ibid.* **1990**, *165*, 513.

[16] Brilloiun, L. *Actualities Sci. Ind.* **1934**, *71*, 159.

[17] Hohenberg, P.; Kohn, W. *Phys. Rev. B*, **1964**, *136*, 864.

[18] Kohn, W., Sham, L.J. *Phys. Rev.* **1965**, *140*, A1133.

[19] Becke, A.D. *J. Chem. Phys.* **1993**, *98*, 5648.

[20] Monkhorst, H.J.; Pack, J.D. *Phys. Rev. B*, **1976**, *13*, 5188.

3. Initial Reactions in CVD of Ta_2O_5 from $TaCl_5$ and H_2O

3.1 Introduction

Tantalum pentoxide thin films, a high-quality dielectric material, have been intensively studied for different applications in microelectronic industry, e.g. as capacitors for dynamic random access memories, gate insulator for metal-oxide-semiconductor devices and integrated optical devices.[21,22,23,24,25,26,27]

Several precursors such as TaF_5,[28] $TaCl_5$, $Ta[N(CH_3)_2]_5$, $Ta(OCH_3)_5$, and $Ta(OC_2H_5)_5$[29] have been applied in the Ta_2O_5 CVD. Tantalum pentachloride has the advantage of avoiding carbon contamination in growing films.[29] It is also suitable for model experimental and theoretical studies of the CVD mechanism since the number and type of intermediate species and reactions involved are expected to be smaller compared to tantalum compounds with alkylamino and alkoxi ligands. A study of atomic layer deposition (ALD) of Ta_2O_5 from $TaCl_5$ and H_2O revealed important details of the deposition mechanism.[30] Since in ALD the active components are introduced into the reaction zone subsequently, it allows a homogeneous distribution of reactants throughout the surface area. It also separates certain deposition reaction steps, which provides films with high precision thickness control and facilitates the study of the deposition mechanism. According to Aarik and coworkers[30] formation of intermediate volatile $TaOCl_3$ explains etching, which occurs at high $TaCl_5$ doses and increased temperature. The reactivity of $TaCl_5$ towards H_2O-treated tantalum oxide has been shown to be higher than the reactivity of H_2O towards $TaCl_5$-treated oxide surfaces.[30]

In this chapter a quantum chemical study of initial reactions in tantalum pentoxide deposition from the $TaCl_5/H_2O$ system[31] are presented. Although this study only concerns selected reactions of gas phase molecules, it helps to understand the molecular mechanism of Ta_2O_5 CVD.

3.2 Computational Methods

Molecular geometries have been optimized using three different theoretical methods: HF, MP2[32] and B3LYP[33] as implemented in the Gaussian98 program package.[34] Analytical harmonic frequencies have been computed at the B3LYP level of theory for all stationary structures and at the HF and MP2 levels for selected molecules. HF vibrational frequencies are scaled by 0.89.[35] Single point coupled cluster CCSD(T)[36] calculations have been done at the B3LYP optimized geometries. All relative energies include zero-point energy (ZPE) corrections. If not specified otherwise relative energies presented here are given at the CCSD(T)//B3LYP level and the structural parameters for the B3LYP optimized geometries.

All calculations were performed using a quasi-relativistic effective core potential (ECP) for tantalum with a valence basis set (441/2111/21), which was derived from the [55/5/3] valence basis set of Hay and Wadt[37]. Also for chlorine an ECP with a valence basis set (4/5)/[2s3p][38] extended by a d-type polarization function[39] was used. For oxygen and hydrogen atoms 6-31G** basis sets[40] was applied. It has been demonstrated for a representative set of transition metal complexes[41] that ECP's generated for *ab initio* methods can be applied in DFT-based calculations as well. In order to confirm the accuracy of the ECP in the reaction mechanism study, B3LYP calculations of tantalum oxochloride formation (see below) with a 6-31G* all-electron basis set[40] for the chlorine atom were performed. The difference in the calculated reaction energies using both kinds of basis sets for chlorine atom is only 3 kcal/mol.

3.3 Results and Discussion

Considering the mechanism of initial reactions leading to formation of tantalum pentoxide from tantalum pentachloride and water we have computed a series of tantalum containing molecules: $TaCl_5$, $TaOCl_3$, TaO_2Cl, $TaCl_4OH$ and $TaCl_3(OH)_2$. For $TaCl_4OH$ and $TaCl_3(OH)_2$ several geometric isomers can be visualized based on different possible locations of Cl and OH in a trigonal bipyramide (axial and equatorial) and H-bonding pattern. Since a detailed conformational analysis of tantalum hydroxichlorides is beyond the scope of our paper we have only considered a few geometric isomers and conformations, which apparently have low energies or are located on a minimum energy pathway toward a reaction transition state. Conformational processes in those molecules are accompanied with small energy changes and thus should be very fast.

3.3.1 Structure, bonding and vibrational frequencies of $TaCl_5$, $TaOCl_3$ and TaO_2Cl

The calculated geometries of $TaCl_5$, $TaOCl_3$ and TaO_2Cl at B3LYP, HF and MP2 are shown at Fig.3.1. The corresponding vibrational frequencies are presented in Tables 3.1-3.3. Experimental data are available only for $TaCl_5$.[42] The experimental value for the equatorial TaCl bond length (2.227Å) is shorter and for the axial bond it is longer (2.369 Å) than the corresponding calculated values. However, the computational values are within standard deviations estimated for the experimental values (see Fig. 3.1a). The B3LYP method provides longer axial and equatorial bonds compared to the other two computational approaches, HF and MP2. In an earlier *ab initio* HF pseudopotential study of $TaCl_5$ 2.369Å and 2.326Å values were reported for the axial and equatorial TaCl bonds, respectively.[43] The B3LYP calculation of $TaCl_5$ with a 6-31G* basis set for chlorine atom gives a bond length of 2.346Å for the axial Ta-Cl bond, which is close to the experimental value. The calculated equatorial Ta-Cl bond length (2.290Å) has a larger deviation from experiment.

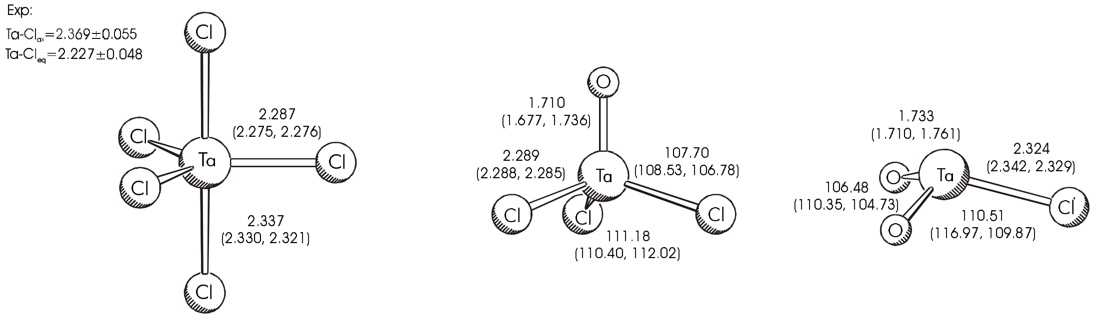

a) $TaCl_5$ b) $TaOCl_3$ c) TaO_2Cl

Fig. 3.1 Optimized geometries of (a) $TaCl_5$, (b) $TaOCl_3$, (c) $TaCl_2O$ at B3LYP level. Values at HF followed by MP2 data are given in perentheses. Bond lengths are given in Å, angles in degrees.

The computed and experimentally assigned[42] vibrational frequencies of $TaCl_5$ are in good agreement except for ν_6 and ν_8, where theory and experiment show opposite values. Similar disagreement between theory and experiment in the symmetry assignment of these two modes has been pointed by Albright et al.[43] The e" mode is formally symmetry forbidden but coupling of vibrational modes may let the ν_8 mode mix with other vibrations. This may lead to an erroneous symmetry assigment based on experimental IR and Raman intensities. The calculated value of 1.7 kcal/mol for the energy of pseudorotation barrier in $TaCl_5$ computed in this work at B3LYP coincides with an earlier estimate at QCISD(T)[43]. It is also in good agreement with an experimental value[42] of 1.2 kcal/mol estimated using electron diffraction data obtained at 100°C.

TABLE 3.1 Computed and experimental vibrational frequencies (in cm^{-1}) and IR intensities (in % to the most active mode) for $TaCl_5$.

Frequency	HF	MP2	B3LYP	Exp.[a)]
$\nu_1(a'_1)$	383 (0)	415 (0)	400 (4)	406
$\nu_2(a'_1)$	294 (0)	330 (0)	319 (0)	324
$\nu_3(a''_2)$	329 (100)	376 (100)	359 (100)	371
$\nu_4(a''_2)$	161 (8)	176 (7)	166 (6)	155
$\nu_5(e')$	371 (55)	413 (50)	399(54)	402
$\nu_6(e')$	138 (4)	147 (3)	139 (3)	181
$\nu_7(e')$	55 (1)	58 (3)	59 (2)	54
$\nu_8(e'')$	182 (0)	198 (0)	187 (0)	127

a) Ref. 16

There are no experimenatal data available for the geometries and vibrational frequencies of $TaOCl_3$. The calculated molecular geometries (Fig. 3.1b) can only be compared with the data obtained from earlier theoretical studies at Hartree-Fock and MP2[44] and at the DFT (local density approximation - LDA)[45] levels of theory. In these and other calculations the ∠OTaCl angle is smaller than ∠ClTaCl in $TaOCl_3$. Similar results were obtained for the other group 5 oxichlorides, $VOCl_3$[45,46] (∠OVCl=107.6°, ∠ClVCl=111.3°) and $NbOCl_3$[45,47] (∠ONbCl=106.0°, ∠ClNbCl=112.7°). This is in contrast to main-group 15 oxochlorides, for example $POCl_3$ (∠OPCl=114.8°, ∠ClPCl=103.7°)[48]. The calculated harmonic frequencies for $TaOCl_3$ are given in Table 3.2 along with experimental frequencies for $VOCl_3$[49] and $NbOCl_3$.[47,50] The frequency pattern is very similar for all three molecules. Vibrational frequencies diminish with increasing atomic mass ($\omega \sim M^{-1/2}$) and the reduced masses of vibrations approach the masses of light ligand atoms, O or Cl, if the mass of the central heavy atom grows. According to this simple extrapolation the $TaOCl_3$ vibrational frequencies suggests them to be 10-20 cm^{-1} smaller than the correspoding values for $NbOCl_3$.

TABLE 3.2 Computed harmonic vibrational frequencies (in cm^{-1}) and IR intensities (in % to the most active mode) for $TaOCl_3$ and experimental vibrational freqiencies for $VOCl_3$ and $NbOCl_3$.

Freq.	HF	MP2	B3LYP	Assignment	$VOCl_3$[a)]	$NOCl_3$[b)]
$\nu_1(a_1)$	1010(100)	949 (31)	1017 (100)	TaO bond stretch	1043	997
$\nu_2(a_1)$	372 (9)	405 (13)	398 (10)	TaCl symmetric bond stretch	411	395
$\nu_3(a_1)$	120 (2)	123 (2)	123 (2)	ClTaCl symmetric bending	160	133
$\nu_4(e)$	377 (57)	420 (100)	410 (80)	TaCl asymmetric bond stretch	508	448
$\nu_5(e)$	216 (4)	223 (2)	227 (3)	OTaCl bending	246	225
$\nu_6(e)$	103 (1)	106 (1)	108 (1)	ClTaCl asymmetric bending	124	106

[a)] Ref. 33 [b)] Ref. 31, 34

An NBO analysis for $TaOCl_3$ at B3LYP is presented in Table 3.3. The Ta-Cl and Ta-O bonds are very polar. The σ and π bonds have a maximum localization of only 26% at the tantalum end. Thus, Ta carries always a large positive charge. The metal *s* orbital contributes more to the Ta-Cl bonds than to the Ta-O σ bonds.

There are neither theoretical nor experimental data available for TaO_2Cl. According to computations presented in this work the molecule is non-planar with Ta-Cl and Ta-O bond lengths being larger than in $TaOCl_3$ (Fig. 3.1c). The non-planar structure is a result of a compromise between ligand-ligand repulsion, which would lead to a planar structure, and the overlap between metal and ligand orbitals, which according to Landis[51] favors smaller than 120° angles for any sd^n hybridization. If the planar structure is imposed in the geometry optimization all bonds become longer (TaO=1.737 Å, TaCl=2.361 Å) and the energy raises by 5.7 kcal/mol at B3LYP.

TABLE 3.3 Results of the NBO analysis at B3LYP: Bond polarity (%Ta), relative contribution of *s, p* and *d* orbitals of tantalum and atomic charges (q).

Bond	%Ta	%s (Ta)	%p (Ta)	%d (Ta)	q(Ta)	q(O)	q(Cl)
			$TaOCl_3$ C_{3v}				
TaCl	18	27	1	72	1.66	-0.71	-0.32
TaO σ	21	18	1	81			
TaO π^a	23	0	1	99			
			TaO_2Cl C_{2v} (planar)				
TaCl	8	68	10	23	2.23	-0.83	-0.56
TaO σ	15	4	12	84			
TaO $\pi_\perp$	26	0	3	97			
TaO $\pi_{\|\|}$	11	5	26	69			
			TaO_2Cl C_s (non-planar)				
TaCl	14	50	2	48	2.06	-0.79	-0.47
TaO σ	18	19	8	74			
TaO π_1	24	3	3	95			
TaO π_2	13	1	29	70			

a) There are two degenerated π orbitals in the C_{3v} symmetric $TaOCl_3$.

In accord with the bond elongation in TaO_2Cl the corresponding Ta-O and Ta-Cl bond stretch vibrations have lower frequencies compared to $TaOCl_3$ (see Table 3.4). The predicted IR spectrum of TaO_2Cl has four intense bands: two modes around 1000 cm^{-1}, which correspond to symmetric and asymmetric Ta-O bond stretching, one mode with a frequency 370 cm^{-1} corresponding to Ta-Cl bond stretching mixed with ∠OTaO bond angle bending. Finally, the vibration at about 100 cm^{-1} corresponds to the ∠TaOCl bond angle bending.

The NBO analysis (see Table 3.3) shows a similar Ta hybridization character in the σ(Ta-O) and Ta-Cl bonds of $TaOCl_3$, while in TaO_2Cl the Ta *d*-orbitals dominate in the σ(Ta-O) bonds and the *s*-orbital mainly contributes to the Ta-Cl bond. In the non-planar TaO_2Cl molecule the Ta AO has almost exact *sd* hybridization in the TaCl bond. There is a significant difference between the charge distribution in the planar and non-planar form of TaO_2Cl. In the non-planar form the Ta atom is less positive (+2.06) than in the planar form (+2.23). Thus bending of the molecule increases the covalent contribution to the chemical bonding in TaO_2Cl.

TABLE 3.4 Computed vibrational frequencies (in cm^{-1}) and intensities (in % to the most active mode) for TaO_2Cl.

Frequency	HF	MP2	B3LYP	Assignment
$\nu_1(a')$	986 (43)	917 (23)	999 (42)	TaO bond symmetric stretch
$\nu_2(a')$	367 (25)	390 (61)	392 (34)	TaCl stretch
$\nu_3(a')$	293 (3)	316 (5)	329 (4)	OTaO bending
$\nu_4(a')$	102 (28)	155 (28)	156 (20)	$ClTa(O_2)$ symmetric bending
$\nu_5(a'')$	925 (100)	904 (100)	946 (100)	TaO bond asymmetric stretch
$\nu_6(a'')$	153 (2)	176 (<1)	180 (<1)	$ClTa(O_2)$ asymmetric bending

3.3.2 Energies and Structures of $TaCl_4OH$ and $TaCl_3(OH)_2$

Tantalum hydroxitetrachloride [$TaCl_4OH$] and tantalum dihydroxitrichloride [$TaCl_3(OH)_2$] are intermediate species in the hydrolysis of tantalum pentachloride yielding tantalum pentoxide. Two geometric isomers can be visualized for $TaCl_4OH$, with equatorial and axial positions of the hydroxyl group, respectively. The two isomers apparently can be converted into each other via a square pyramidal transition state (Berry pseudorotation) – Scheme 1.

Both geometric isomers and the energetically low lying transition state shown in Scheme 3.1 (see Fig 3.2 a-c and Table 3.5) were located. The isomer with an equatorial position of the OH group (Fig. 3.2a) is more stable.

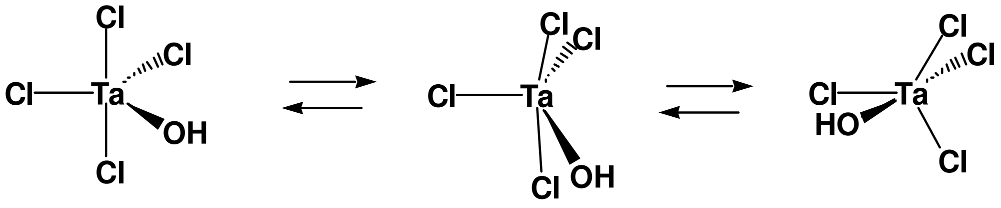

Scheme 3.1

All methods predict that the OH-ax isomer (see Fig. 3.2c) is ca. 1 kcal/mol higher in energy. The barrier for interconversion of OH-eq into OH-ax is ~2 kcal/mol. In all three structures the OH group forms an H-bond with the nearest chlorine atom. The average OH…Cl *intramolecular* H-bond distance is 2.932 Å at B3LYP, which can be compared with 2.56 (2.57) Å *intermolecular* H-bond in $(HCl)_2$ dimer computed at the B3LYP (MP2) level with 6-31+G** basis set.[52] According to Del Bene et al.[52] the B3LYP method somewhat overestimates binding energies of H-bonds and give shorter than experimental bond distances, particularly for small basis sets.

TABLE 3.5 Relative energies of $TaCl_4OH$ and $TaCl_3(OH)_2$ conformers (in kcal/mol).

	HF	MP2	B3LYP	CCSD(T)
		$TaCl_4OH$		
OH-eq	0.0	0.0	0.0	0.0
TS	1.9	1.9	2.0	1.9
OH-ax	1.2	0.9	1.1	0.9
		$TaCl_3(OH)_2$		
OH, OH-eq	0.0	0.0	0.0	0.0
TS	2.8	2.9	2.8	3.1
OH-eq, OH-ax	1.3	0.4	0.8	0.9

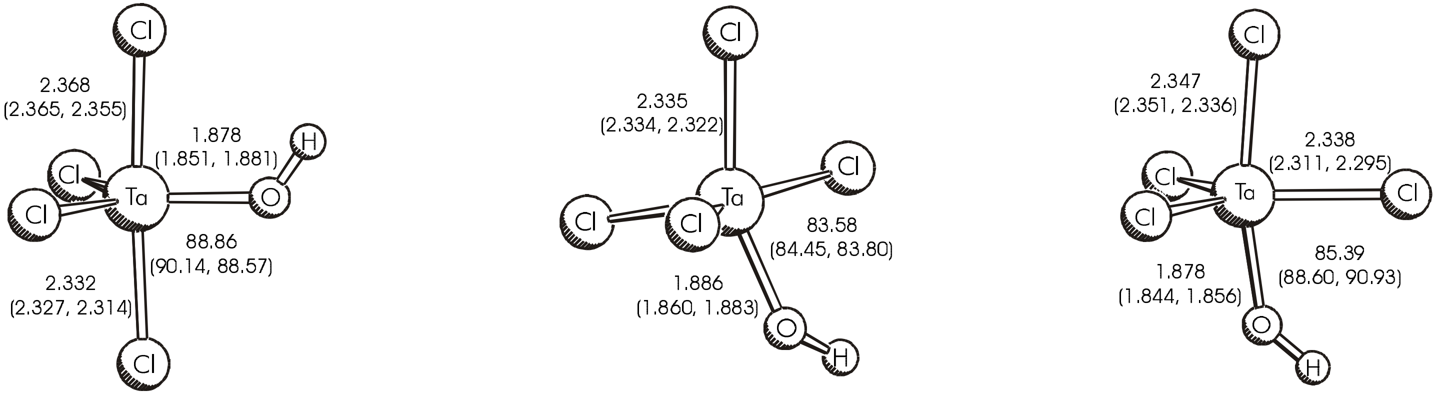

a) $TaCl_4OH$-eq

b) $TaCl_4OH$-TS

c) $TaCl_4OH$-ax

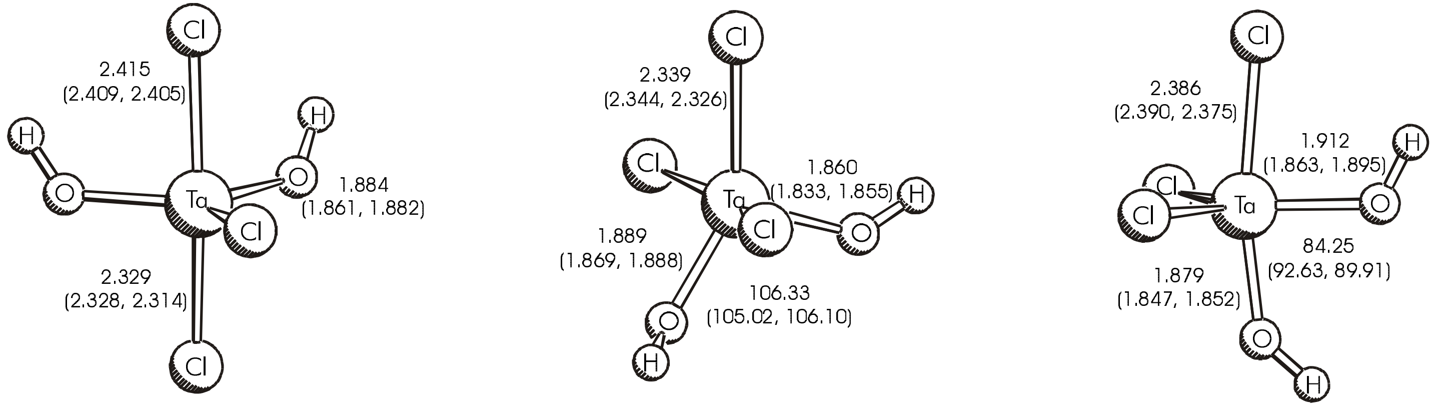

d) $TaCl_3(OH)_2$-eq,eq

e) $TaCl_3(OH)_2$-TS

f) $TaCl_3(OH)_2$-eq,ax

Fig.3.2 Optimized geometries of $TaCl_4OH$ and $TaCl_3(OH)_2$ conformers at the B3LYP level. Values at HF followed by MP2 are given in paretheses.

For $TaCl_3(OH)_2$ the product of the second step of $TaCl_5$ hydrolysis, three isomers with respect to the position of OH and Cl in the trigonal bipyramide can be visualize (Scheme 3.2).

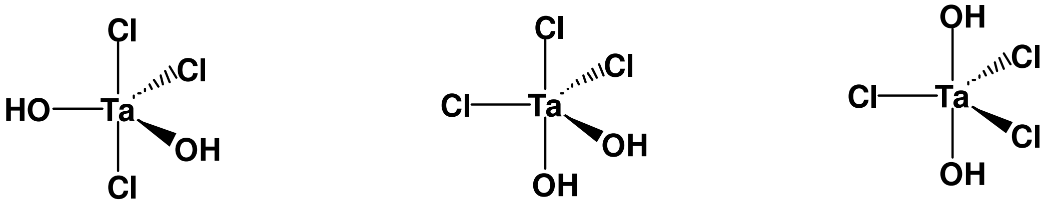

OH,OH-eq **OH-eq, OH-ax** **OH,OH-ax**

Scheme 3.2

All three isomers were computed at the B3LYP level. As expected from the results of the $TaCl_4OH$ computations, stability of isomers with axial OH groups is lower. Thus the relative energy of the least stable isomer with two axial OH groups (**OH,OH-ax**) is 1.8 kcal/mol above the energy of the most stable isomer with two equatorial OH groups (**OH,OH-eq**). We have computed only the first two geometric isomers on Scheme 3. 2 and the transition state between them at all four levels of theory. (see Fig. 3.2d-f and Table 3.5. The barrier for pseudorotation is ~3 kcal/mol for $TaCl_3(OH)_2$, which is 1 kcal/mol higher than the barrier in $TaCl_4(OH)$. According to the results derived for $TaCl_4OH$ two patterns in the H-bond should be favorable (Scheme 3.3).

It was found at B3LYP that the *trans* H-bond conformation is less favorable than the *cis* conformation by 0.7 kcal/mol. Since an extensive conformational analysis is beyond of the scope of this work we have not considered the *trans* H-bond conformation.

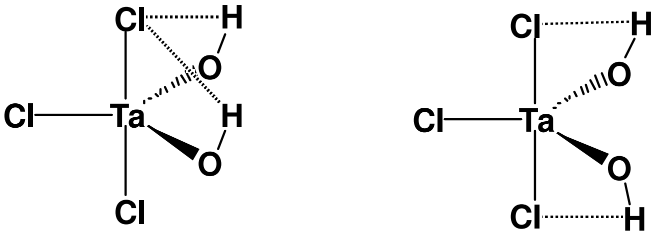

OH,OH-eq- *cis* **OH,OH-eq- *trans***

Scheme 3.3

3.3.3 Thermochemistry of gas phase reactions in the system $TaCl_5/H_2O$

Hydrolysis of $TaCl_5$ and deposition of Ta_2O_5 include a series of elementary reactions of substitution of chlorine by oxygen in the coordination sphere of tantalum. Some initial reactions between $TaCl_5$ and H_2O, which may occur in the tantalum pentoxide CVD process in the gas phase or on the growing Ta_2O_5 surface terminated by Cl and OH groups were studied in details. Zero Kelvin heats of reactions are presented in Table 3.6. The first and second steps of $TaCl_5$ hydrolysis have similar reaction energies at all levels of theory. Since the coordination of tantalum remains the same on the left and right sides in equations 1 and 2, correlation effects probably compensate in the reaction energies of the two reactions. Such a compensation effect is not observed in the last three reactions, where the coordination number of Ta becomes lower in the reaction course and strong correlation effects may be expected. Note that even in the nonisodesmic equations 3-5 in Table 3.6 the B3LYP reaction energies are close to CCSD(T) values within a 3 kcal/mol range, while MP2 values differ by about 8 kcal/mol from CCSD(T).

TABLE 3.6 Zero Kelvin heats of initial reactions of $TaCl_5$ hydrolysis and Ta_2O_5 deposition (in kcal mol).[a)]

Reaction	HF	MP2	B3LYP	CCSD(T)
(1) $TaCl_5 + H_2O \rightarrow TaCl_4OH + HCl$	-8.0	-7.6	-8.6	-7.3
(2) $TaCl_4OH + H_2O \rightarrow TaCl_3(OH)_2 + HCl$	-8.0	-6.8	-7.4	-6.8
(3) $TaCl_4OH \rightarrow TaOCl_3 + HCl$	11.7	0.1	9.2	8.0
(4) $TaCl_3(OH)_2 \rightarrow TaOCl_3 + H_2O$	19.7	6.9	16.6	14.9
(5) $TaOCl_3 + H_2O \rightarrow TaO_2Cl + 2HCl$	90.0	76.6	78.7	82.0

[a)] Lower energy conformers of $TaCl_4OH$ and $TaCl_3(OH)_2$ have been used used in computation of heats of reactions (1)-(4).

While the substitution of Ta-Cl bonds by Ta-OH in reactions 1 and 2 is *exothermic*, the formation of a Ta=O double bond is *moderately endothermic* in reactions 3 and 4 and *strongly endothermic* in reaction 5, what certainly makes tantalum oxichlorides, particularly TaO_2Cl, difficult for experimental observation. The B3LYP calculation of the energy of the reaction $TaCl_5 + H_2O \rightarrow TaCl_3O + 2HCl$ (sum of the energies of reactions 1 and 3 in Table 6) using a 6-31G* basis set for chlorine gives 3.6 kcal/mol which is in a reasonable agreement with 0.6 kcal/mol obtained in the calculations using an ECP for Cl .

The calculated reaction energies presented in Table 3.6 allow to estimate heats of formation of all tantalum containing molecules in Table 3.6, based on ΔH^o_f values available for $TaCl_5$ (-182.8 kcal/mol), H_2O (-57.8 kcal/mol) and HCl (-22.1 kcal/mol)[53]- see Table 3.7. For the estimation of the heats of formation the most reliable CCSD(T) values for the reaction energies were applied. Using these data and known heats of formation[53] for gaseous Ta (186.9 kcal/mol), Cl (29.0 kcal/mol), O (59.6 kcal/mol) and OH (9.3 kcal/mol) also the Ta-O bond dissociation energies can be estimated. For this purpose a simple additivity approach was used together with the assumption that the Ta-Cl bonds have the same (average) energy of 102.9 kcal/mol in all tantalum containing molecules, which can be estimated from the heat of atomization of $TaCl_5$ (Table 3.7). It is seen that the Ta-O single bond energies are similar in $TaCl_4OH$ and in $TaCl_3(OH)_2$, which can be (tentatively) used for validating an additivity approach in calculating bong energies in other $TaCl_x(OH)_{5-x}$ molecules. Note that the Ta=O double bond in $TaOCl_3$ has a higher bond energy than in TaO_2Cl indicating a partial triple bond character in C_{3v} symmetric oxotrichloride. The computed TaO bond energies can also be compared with Ta-C (67 kcal/mol), Ta=C (126 kcal/mol) and Ta-I (62.9 kcal/mol) avarage bond energies.[54] Probably the ionic character makes the TaO bond much stronger than the less polar (more covalent) TaC and TaI bonds. This is particularly displayed in the Ta-O *single* bond, which is predicted to have similar bond energy as the Ta=C double bond.

TABLE 3.7 Estimated heats of formation and Ta-O bond dissociation energies in tantalum containing molecules.

	$TaCl_4OH$	$TaCl_3(OH)_2$	$TaOCl_3$	TaO_2Cl
ΔH^o_f [kcal/mol]	-225.8	-268.3	-195.7	-127.3
E_{TaO} [kcal/mol]	126.4	126.1	220.5	179.8

Assuming that the further hydrolysis steps have similar (~ -7 kcal/mol) reaction energies as for reactions 1 and 2 in Table 3.6, the difference in the estimated heats of formation for $TaCl_4OH$ and $TaCl_3(OH)_2$ as an increment to calculate ΔH^o_f for completely hydrolyzed $Ta(OH)_5$ can be used. This gives a value of ΔH^o_f = -395.8 kcal/mol, which can be used further to estimate the heat of reaction for conversion of hypothetical gaseous $Ta(OH)_5$ into solid Ta_2O_5:

$$2Ta(OH)_5 \rightarrow Ta_2O_5 + 5H_2O \qquad \Delta H^o_r = 13.6 \text{ kcal/mol}$$

A calculation based on tabulated heats of formation of gaseous $TaCl_5$ and H_2O and solid Ta_2O_5 (-489.0 kcal/mol)[53] gives a negative (exothermic) value of the reaction heat for the formation of Ta_2O_5:

$$2TaCl_5 + 5H_2O \rightarrow Ta_2O_5 + 10HCl \qquad \Delta H^o_r = -55.4 \text{ kcal/mol}$$

Entropy effects favor formation of tantalum pentoxide for both reactions particularly at higher temperatures applied in CVD.

Although thermodynamic calculations are important in estimating the "chemical driving force", energy balance and relative stability of the intermediates and products of deposition, in most cases CVD processes occur at conditions which are far from thermodynamic equilibrium. The film structure and composition are governed by other factors: chemical kinetics, surface and gas diffusion and mass transfer. To reveal important details of potential energy surfaces for the types of reactions, which may occur in tantalum pentachloride CVD, transition states and intermediate complexes for the first step of $TaCl_5$ hydrolysis (eq 1 in Table 3.6) and for $TaCl_3(OH)_2$ dehydration and for $TaCl_4OH$ dehydrochlorination (eq 1, 4 and 3, respectively, in Table 3.6) were computed.

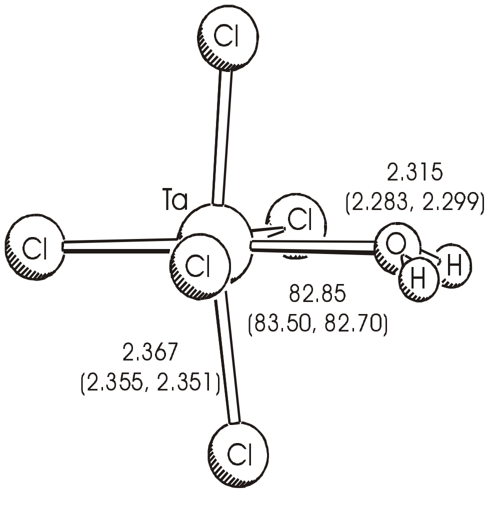

a) $TaCl_5$-H_2O

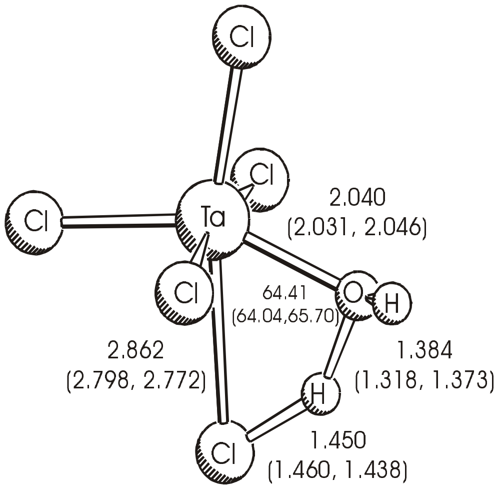

b) $TaCl_5$-H_2O transition state

Fig.3.3 Geometries of $TaCl_5$-H_2O complex and $TaCl_5$-H_2O TS optimized at B3LYP level. Values at HF and MP2 are given in parentheses.

3.3.4 Mechanism of hydrolysis of $TaCl_5$

High valent transition metal compounds easily form complexes with electron donors increasing the coordination number of the central atom. According to the calculated results $TaCl_5$ forms a strong donor-acceptor complex with H_2O (see Fig. 3.3a and Fig. 3.4). The stabilization energy of the complex varies within a 6 kcal/mol range between 20 kcal/mol value at HF and 26 kcal/mol at MP2, with the B3LYP value being close to the HF value and MP2 matching CCSD(T). The Ta-O distance in the $TaCl_5$-H_2O complex is about 0.5 Å longer than in tantalum hydroxichlorides: $TaCl_4OH$ and $TaCl_3(OH)_2$ (Fig.2). The calculated 2.315 Å at B3LYP can be compared with experimental Ta-OH_2 distance in Cp*Ta(OH2)(p-tert-butylcalix[4]arene), which is equal 2.188 Å.[55]

The transition state energy in the reaction of $TaCl_5$ hydrolysis is lower than the energy of the separated $TaCl_5$ and H_2O molecules at all but the HF level. Overestimation of the reaction barrier is typical for the Hartree-Fock method, while B3LYP and CCSD(T) give similar barriers within a reasonable 3 kcal/mol range. Thus these calculations predict that in the gas phase $TaCl_5$ hydrolysis should occur without a barrier. However, considering the same reaction of $TaCl_5$ adsorbed on the surface (or similar reaction for a $TaCl_x$ surface fragment), one must take into account the surface as a part of the reacting system. The energy released in formation of $TaCl_5$-H_2O complex (~26 kcal/mol) dissipates in surface and bulk film vibrational modes. Thus the barrier for the reaction on the surface is not equal to the energy difference between separated $TaCl_5/H_2O$ and the transition state but the one between $TaCl_5$-H_2O complex and TS (~20 kcal/mol).

The Ta-Cl distance in the transition state (see Fig. 3.3b), which corresponds to a leaving Cl atom, is about 0.5 Å longer than in the $TaCl_5$-H_2O complex, while the Ta-O distance is intermediate between the values in the complex and in $TaCl_4OH$.

It was not possible at applied levels of theory to locate a $TaCl_4OH$-HCl complex with six-coordinated tantalum on a „product site“ similar to the $TaCl_5$-H_2O complex on the „reactant site“. At each level the optimization did collapse to a hydrogen bonded form $TaCl_4OH$...ClH without formation of a donor-acceptor bond between Ta and Cl.

The structures and energies along the path of hydrolysis of tantalum hydroxitetrachloride were considered as next. $TaCl_4OH$ forms a strong complex with water (-21.6 kcal/mol at B3LYP), in which H_2O is positioned at the back side of the OH group. The Ta-O bond length in $TaCl_4OH$-H_2O is 2.289 Å at B3LYP, which is 0.026 Å shorter than in $TaCl_5$-H_2O. The hydrolysis of $TaCl_4OH$ proceeds similar to the hydrolysis of $TaCl_5$ with transition state energy close to the energies of separated $TaCl_4OH$ and H_2O molecules : -2.4 kcal/mol at B3LYP.

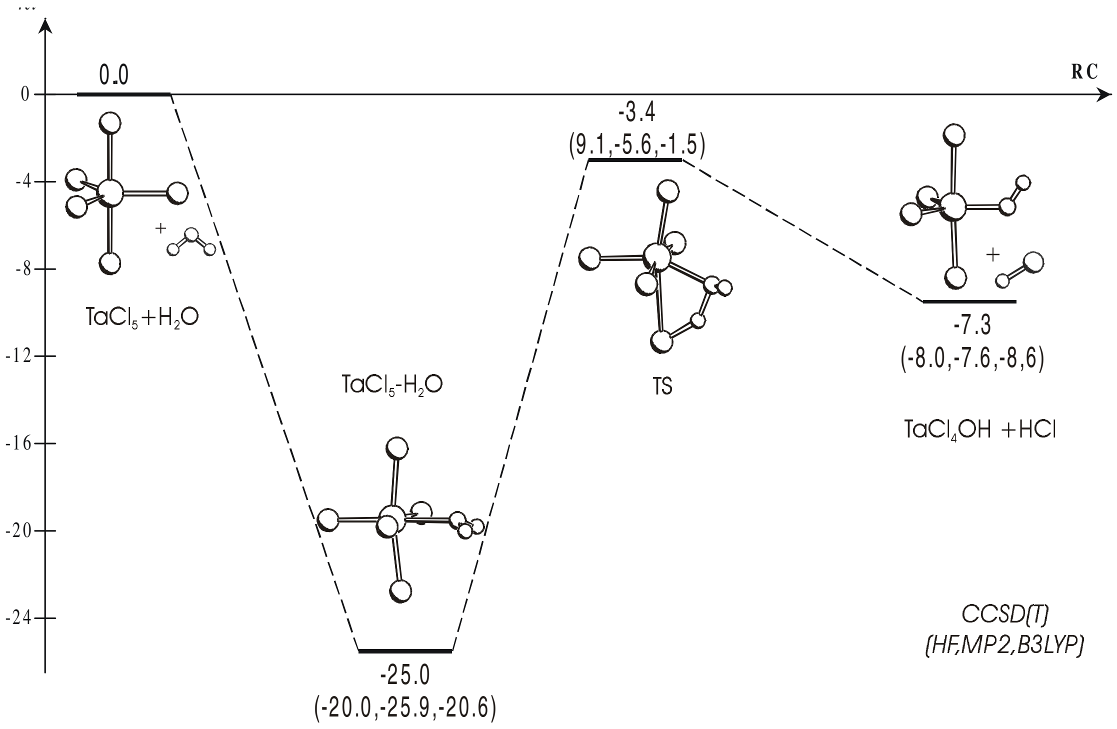

Fig. 3.4 Calculated reaction path for the hydrolysis of $TaCl_5$ at CCSD(T). Relative energies at HF, MP2 and B3LYP are given in parentheses.

3.3.5. Mechanism of dehydration of tantalum $TaCl_3(OH)_2$

The termination of tantalum pentoxide film surface by the OH group is most plausible under atmospheric condition or exposure to water under deposition condition, which include H_2O as a precursor (oxygen source). According to Aarik and coworkers[30] the film etching, which occurs at higher $TaCl_5$ concentrations and elevated temperature, can be explained by the formation of intermediate volatile tantalum oxichlorides, e.g. $TaOCl_3$. Formation of TaO_2Cl is unfavorable because of a very high endothermicity for its formation (see Table 3.6).

Optimized stationary structures, minima and transition states, for $TaOCl_3$ formation from $TaCl_3(OH)_2$ are presented at Fig. 3.2d-f and Fig. 3.5. The most stable isomer of $TaCl_3(OH)_2$ (both OH- groups in equatorial positions, Fig. 3.2d) was used as the starting point of the study of dehydration of tantalum dihydroxytrichloride.

However, the direct minimum energy path from the transition state (see Fig. 3.6) to the reactant shows that another isomer with one axial and one equatorial OH group (Fig. 3.2f) is the direct product of the reverse reaction. It was possible to find computationally a transition state between two TaCl$_3$(OH)$_2$ isomers (Fig. 3.2e), which is discussed above. Since the transition state between the TaCl$_3$(OH)$_2$ isomers has a much lower energy than the transition state for H$_2$O elimination, Berry pseudorotation does not play a significant role in the reaction of TaCl$_3$(OH)$_2$ dehydration and can be ignored in most of the kinetics modeling studies.

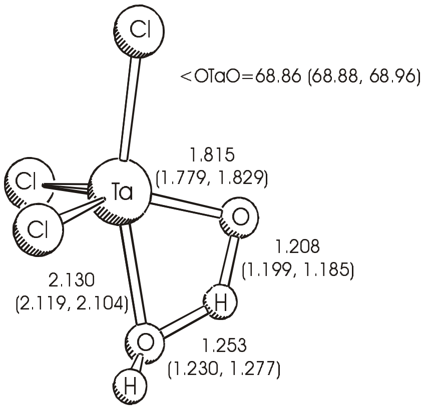

a) TaCl$_3$(OH)$_2$ transition state

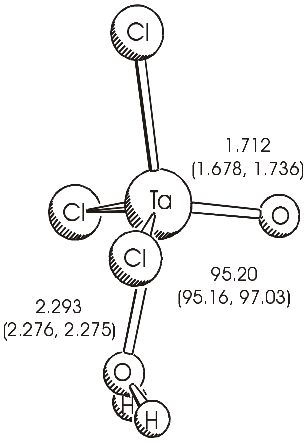

b) TaCl$_3$O-H$_2$O

Fig. 3.5 Geometries of the TaOCl3-H2O TS and the TaOCl3-H2O complex optimized at B3LYP. HF and MP2 data are given in parentheses.

Also TaOCl$_3$ forms a strong complex with water with a stabilization energy at ~20 kcal/mol. The water molecule is positioned trans to the Ta-Cl bond. The relative energy of TaOCl$_3$-H$_2$O with respect to TaCl$_3$(OH)$_2$ depends substantially on the computational method. MP2 shows the largest deviation from CCSD(T).

Since in a TaCl$_5$/H$_2$O → Ta$_2$O$_5$ CVD process water vapor is used as a precursor, also the dehydration of TaCl$_3$(OH)$_2$ assisted by one water molecule was considered. The catalytic effect of external H$_2$O is provided by increasing polarity (microsolvation) and decreasing the strain in the transition state for dehydration. The energy of two H- bonds in the intermediate TaCl$_3$(OH)$_2$-H$_2$O complex (see Fig. 3.6 and 3.7a) is 9.6 kcal/mol at CCSD(T). The transition state in the H$_2$O assisted dehydration of TaCl$_3$(OH)$_2$ (Fig. 3.7b) qualitatively corresponds to the complex of negatively charged TaCl$_3$(OH)O$^-$ with H$_3$O$^+$ cation. The actual charge transfer between these two

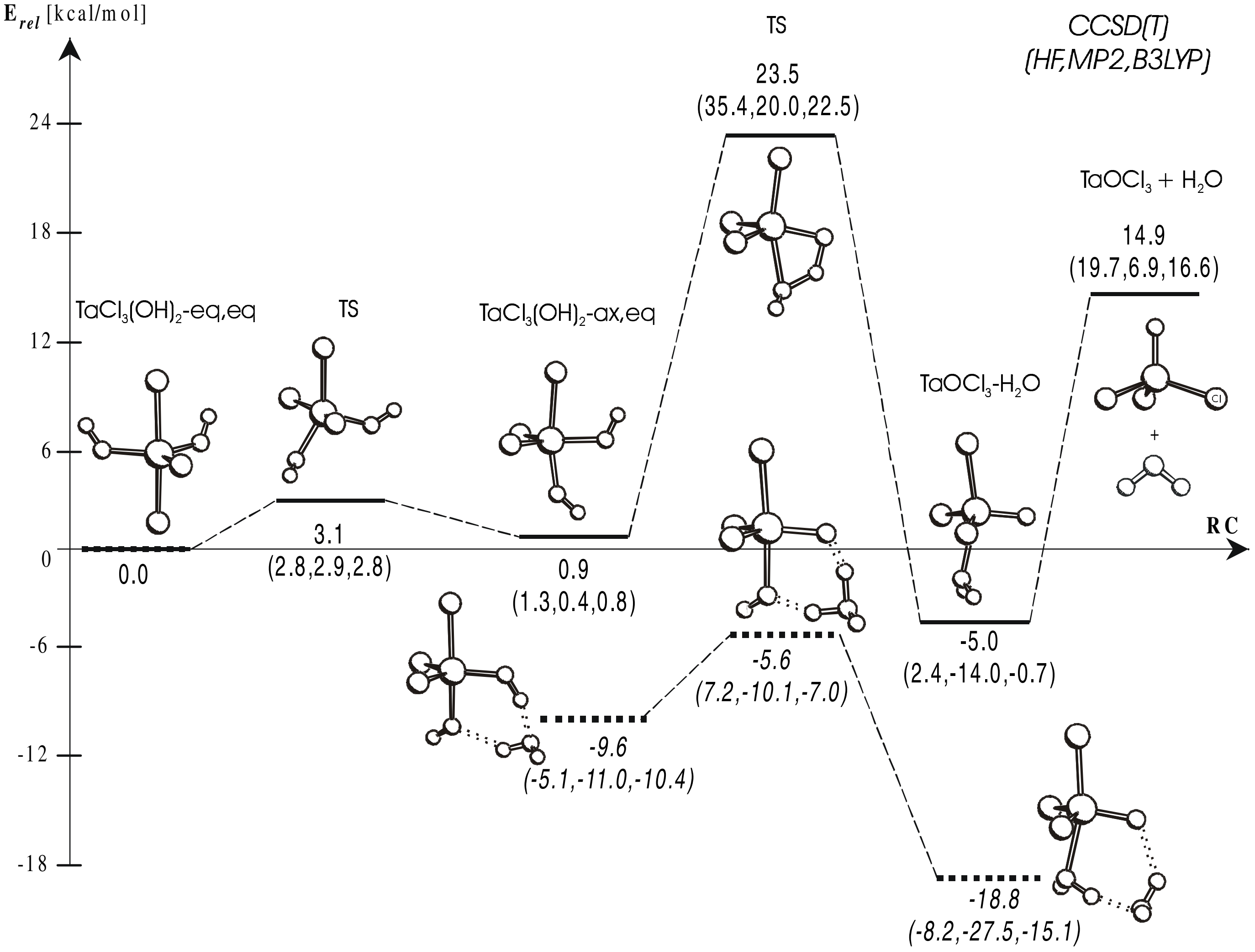

Fig. 3.6 Calculated reaction path for the dehydration of $TaCl_3(OH)_2$ at CCSD(T) without (top) and with (bottom) water assistance .Relative energies at HF, MP2 and B3LYP are given in parentheses. Relative energies for the water-assisted reaction are calculated with respect to separated $TaCl_3(OH)_2$ and H_20.

fragments is 0.69 electrons in NBO analysis. The barrier for the water-assisted hydrogen transfer to $TaCl_3O$-H_2O complex is now reduced from 22.6 kcal/mol to 4 kcal/mol at CCSD(T). Such phenomenon of microsolvation in the gas phase has already been reported [56].

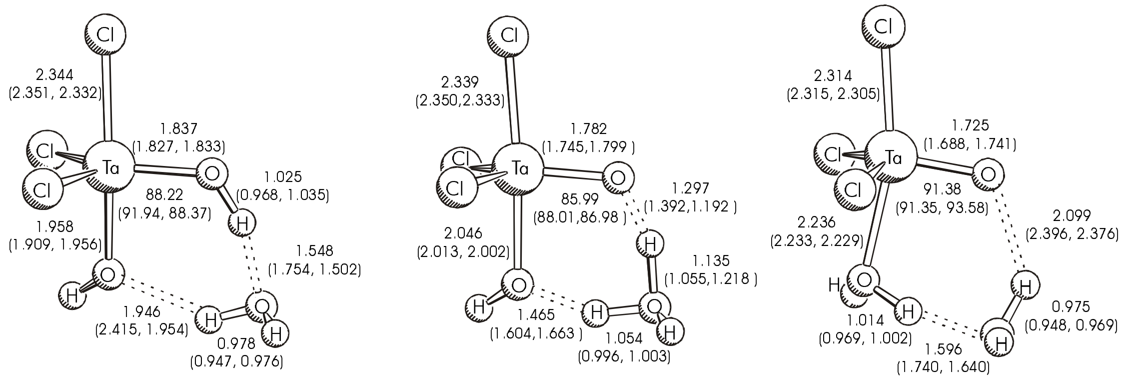

a) TaCl3OHOH-H2O

b) TS

c) TaCl3O-2H2O

Fig.3.7 B3LYP geometries of $TaCl_3(OH)_2$, transition state and $TaCl_2O$-H_2O complex with assisting water molecule. Values at HF followed by MP2 data are given in parentheses.

3.3.6 Mechanism of HCl loss of $TaCl_4OH$

Another reaction which may lead to the formation of $TaOCl_3$ is dehydrochlorination of $TaCl_4OH$ (reaction 3 in Table 3.6). This reaction presents a simplified model of HCl chemical desorption from the Ta_2O_5 surface. An unimolecular (direct) and bimolecular (water assisted) decomposition of $TaCl_4OH$ into $TaOCl_3$ and H_2O were considered. The energy diagrams for both reactions are shown on Fig. 3.8. The barriers for an unimolecular decomposition of $TaCl_4OH$ with elimination HCl (20.4 kcal/mol) and $TaCl_3(OH)_2$ with H_2O elimination (23.5 kcal/mol) are similar. In the transition state for the HCl elimination (see Fig. 3.9a) the TaCl bond is elongated by

~0.5 Å. Compared to the equilibrium positions in HCl (1.295 Å) and in $TaCl_4OH$ (0.968 Å) the corresponding ClH and OH bond lengths are elongated by 0.354 Å and 0.283 Å, respectively.

Water assistance significantly reduces the reaction barrier for HCl elimination from $TaCl_4OH$. However, in contrast to the $TaCl_3(OH)_2/H_2O$ system, where the transition state structure resembles the complex of $TaCl_3(OH)O^-$ with H_3O^+ (Fig 3.7b), the TS for water assisted HCl elimination is product like (see Fig. 3.9b) and closely corresponds to the H-bonded complex of $TaCl_3O$, H_2O and HCl. The TS for H_2O assisted HCl elimination was located only at the HF level. The dominating component in the imaginary frequency vector corresponds to the proton transfer between H_2O and HCl, while the corresponding vector in the TS for water assisted H_2O elimination from $TaCl_3(OH)_2$ shows synchronous motion of two protons.

Neither transition state nor the subsequent H-bonded complex of $TaCl_3O/H_2O/HCl$ have been located at the correlated levels, B3LYP and MP2 (Fig.3.8b). This suggests the water assisted decomposition of $TaCl_4OH$ occurs without a barrier, when correlation energy is included. This is also (indirectly) confirmed by a very low single point CCSD(T) energy (-10 kcal/mol) computed at the HF optimized structure of the TS (see Fig. 3.9b).

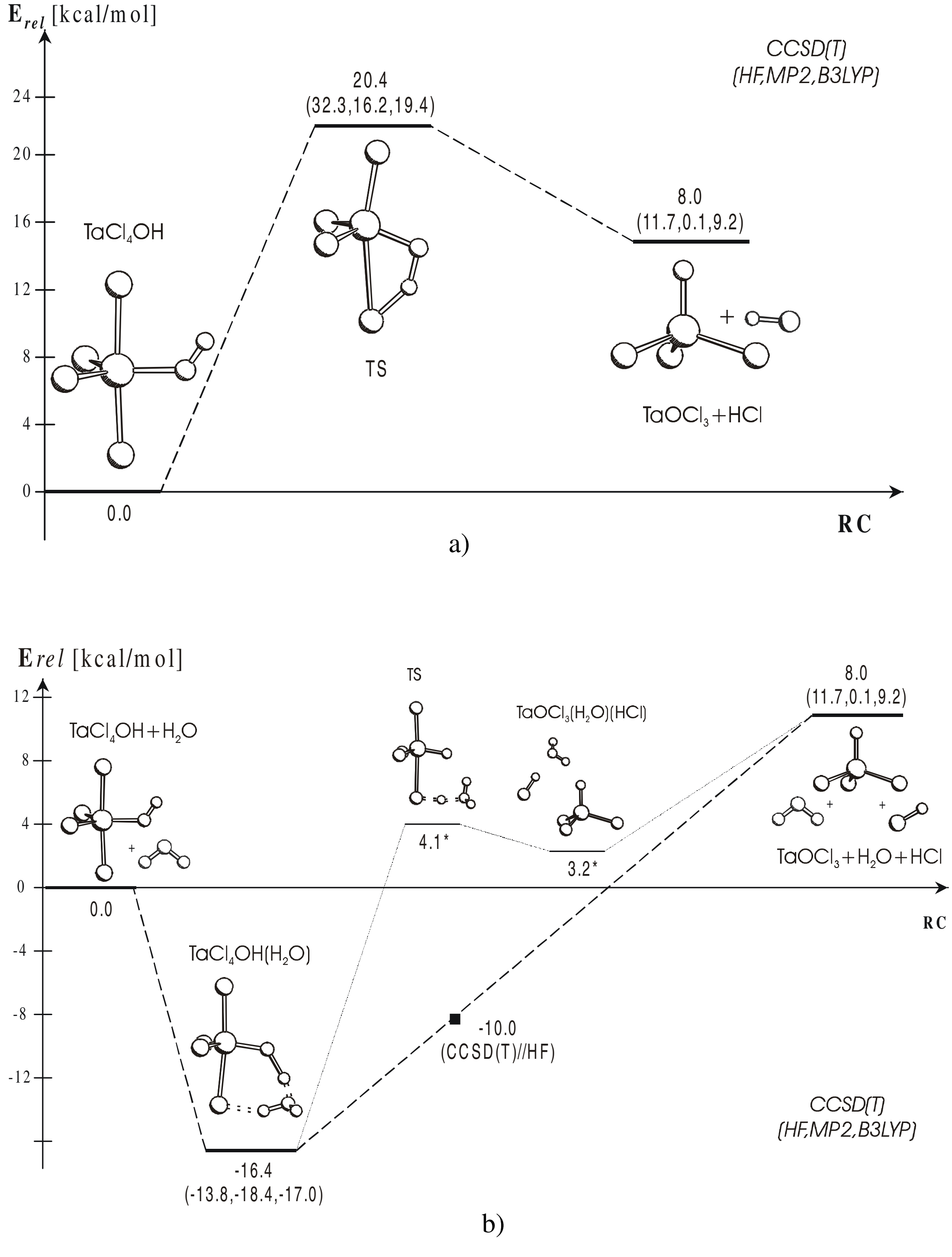

Fig. 3.8 Calculated reaction path for dehydrochlorination of $TaCl_4OH$ at CCSD(T) : (a) direct decomposition (b) water-assisted reaction. Relative energies at HF, MP2 and B3LYP are given in parentheses.

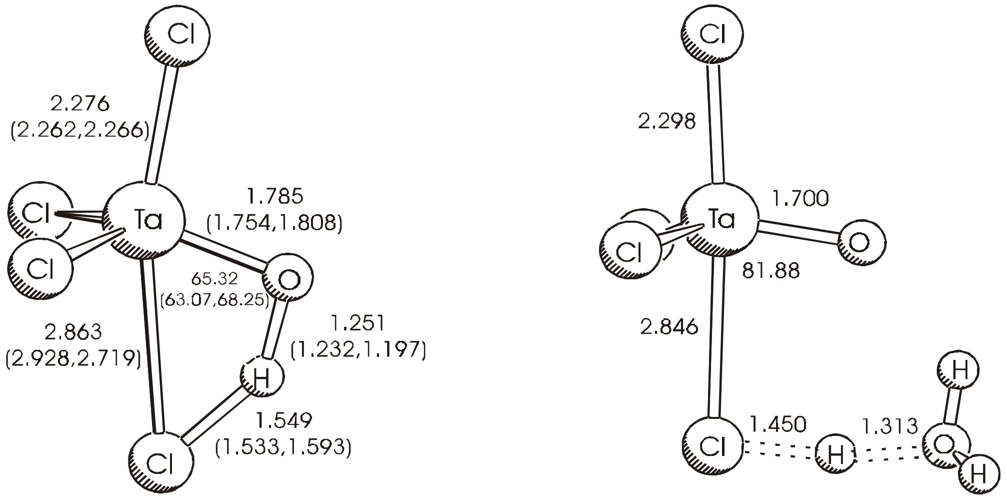

a) $TaCl_3O$-HCl transition state

b) $TaCl_3O$-HCl transition state with assisting water*

Fig. 3.9 B3LYP optimized geometries of TS for elimination of HCl from TaCl4OH in (a) direct decomposition, (b) water assisted reaction. Hf and MP2 values are given in parentheses. *values only at HF level.

3.4 Summary and Conclusions

The results of theoretical investigation presented in this chapter can be summarized as follows:

1. The calculated geometries and vibrational frequencies of the high-valent tantalum compounds which are predicted at the HF, MP2 and B3LYP levels of theory are in good agreement with experimental results of known species. The reaction energies and complex formation energies which are obtained at the CCSD(T) and B3LYP levels do not exhibit large deviations from each other, while the MP2 energies appear to be less reliable.

2. The experimentally yet unknown compounds $TaOCl_3$ and TaO_2Cl have been characterized theoretically. The formation of TaO_2Cl from $TaCl_5$ and $TaOCl_3$ is a thermodynamically disfavored process.

3. The calculations predict that $TaCl_5$ hydrolysis in the gas phase should take place with a small or no barrier at all. The first step of the reaction is the formation of strongly bonded water complex, which eliminates HCl with a substantial barrier with respect to the complex.

4. Water loss from $TaCl_3(OH)_2$ and HCl loss from $TaCl_4OH$ have been studied as model reactions for etching of Ta_2O_5 films at high $TaCl_5$ concentrations at elevated temperatures. Both reactions have large barriers for the unimolecular pathway. The activation barrier becomes much lower through the catalytic assistance of a water molecule, which opens a barriereless reaction channel for reactions in the gas phase. $TaOCl_3$ forms a strong water complex like $TaCl_5$ does with a similar complex formation energy. The role of the assisting water molecule in the etching process is emphasized.

References

---

[21] McKinley, K.A.; and Sandler, N.P. *Thin Solid Films*, **1996**, *290-291* , 440.

[22] Rausch, N.; Burte, N.P. *Microelectronics Journal,* 1993, 421.

[23] Treichel, H.; Mitwalsky, A.; Sandler, N.P.; Tribula, D.; Kern, W.; Lane, A.P. *Advanced Materials for Optics and Electronics,* **1992**, *1,* 299.

[24] Tanimoto, S.; Matsui, M.; Aoyagi, M.; Kamisako, K.; Kuroiwa, K.; Tarui, Y. *Jpn. J. Appl. Phys.* **1991**, *30,* L330.

[25] Zaima, S.; Furuta, T.; Yasuda, Y.; Lida, M. *J Electrochem Soc*, **1990**, *137 ,* 1297.

[26] Nishioka, Y.; Shinriki, H.; Mukai, K. *J. Electrochem. Soc.* **1987**, *134,* 410.

[27] Ingrey, S.J.; Westwood, Y.C.; Cheng, Y.C.; Wei, J. *Appl. Opt.* **1975**, *14,* 2194.

[28] Devine, R.A.B.; Chaneliere, C.; Autran, J.L.; Balland, B.; Paillet, P.; Leray, J.L. *Microelectron. Eng.,* **1997**, *36,* 61.

[29] Koyama, H.; Tanimoto, S.; Kuroiwa, K.; Tarui, Y. *Jpn. J. Appl. Phys.* **1994**, *33,* 6291.

[30] (a) Aarik, J.; Aidla, A.; Kukli, K.; Uustare, T. *J. Cryst. Growth,* **1994**, *75,* 180. (b) Kukli, K.; Aarik, J.; Aidla, A.; Kohan, O.; Uustare, T.; Sammelselg, V. *Thin Solid Films,* **1995**, *260,* 135. (c) Simon, H.; Aarik, J. *J. Physique iV.* **1995**, *5,* C5-277. (d) Aarik, J.; Kukli, K.; Aidla, A.; Pung, L. *Appl. Surf. Sci.* **1996**, *103,* 331.

[31] The preliminary results were presented at E-MRS 1999 Spring Meeting in Strasbourg, 1-4 June 1999.

[32] (a) Møller, C.; Plesset, M.S. *Phys. Rev.***1934**, *46*, 618. (b) Binkley, J.S.; Pople, J.A. *Int. J. Quantum Chem.* **1975**, *9S*, 229.

[33] Becke, A.D. *J. Chem. Phys.* **1993**, *98*, 5648.

[34] Gaussian 98, Revision A.3, Frisch, M.J.;Trucks, G.W.; Schlegel, H. B.; Secures, G. E.; Robb, M. A.; Cheeseman, J. R.; Zakrzewski, V.G.; Montgomery, Jr. J. A.; Stratmann, R. E.; Burant, J. C.; Dapprich, S.; Millam, J. M.; Daniels, A. D.; Kudin, K. N.; Strain, M. C.; Farkas, O.; Tomasi, J.; Barone, V.; Cossi, M.; Cammi, R.; Mennucci, B.; Pomelli, C.; Adamo, C.; Clifford, S.; Ochterski, J.; Petersson, G. A.; Ayala, P. Y.; Cui, Q.; Morokuma, K.; Malick, D. K.; Rabuck, A. D.; Raghavachari, K.;

Foresman, J. B.; Cioslowski, J.; Ortiz, J. V.; Stefanov, B. B.; Liu, G.; Liashenko, A.; Piskorz, P.; Komaromi, I.; Gomperts, R.; Martin, R. L.; Fox, D. J.; Keith, T.; Al-Laham, M. A.; Peng, C. Y.; Nanayakkara, A.; Gonzalez, C.; Challacombe, M.; Gill, P. M. W.; Johnson, B.; Chen, W.; Wong, M. W.; Andres, J. L.; Gonzalez, C.; Head-Gordon, M.; Replogle, E. S.; Pople, J. A., Gaussian, Inc., Pittsburgh PA, 1998.

[35] Hehre, W.J.; Radom, L.; Pople, J.A.; Schleyer, P.v.R. *Ab Initio Molecular Orbital Theory*, Wiley, 1986

[36] (a) Cizek, J.; *J. Chem. Phys.* **1966**, *45*, 4256; (b) Pople, J. A.; Krishnan, R.; Schlegel, H.B.; Binkley, J.S. *Int. J. Quantum Chem.* **1978**, *14*, 545; (c) Bartlett, R.J.; Purvis, G.D. *Ibid.* **1978**, *14*, 561; (d) Purvis, G.D; Bartlett, R.J. *J. Chem. Phys.* **1982**, *76*, 1910; (e) Raghavachari, K.; Trucks, G.W.; Pople, J.A.; Head-Gordon, M. *Chem. Phys. Lett.* **1989**, *157*, 479; (f) Bartlett, R.J.; Watts, J.D.; Kucharski, S.A.; Noga, J. *Ibid.* **1990**, *165*, 513.

[37] Hay, P.J.; Wadt, W.R. *J. Chem. Phys.* **1985**, *82*, 299.

[38] Bergner, A.; Dolg, M.; Kuechle; W., Stoll, H.; Preuss, H. *Mol. Phys.* **1993** ,*80*, 1413.

[39] Huzinaga, S. *Gaussian basis sets for molecular calculations*, Elsevier Amsterdam, Oxford, New York, Tokyo 1984.

[40] (a) Ditchfield, R.; Hehre, W.J.; Pople, J.A. *J. Chem. Phys.* **1971**, *54*, 724. (b) Hariharan, P.C.; Pople, J.A. *Theor. Chim. Acta* **1973**, *28*, 213. (c) Francl, M.M.; Pietro, W.J.; Hehre, W.J.; Binkley, J.S.; Gordon, M.S.; DeFrees, D.J.; Pople, J.A. *J. Chem. Phys.* **1982**, *77*, 3654.

[41] Russo, T.V.; Martin, R.L; Hay, P.J. *J. Phys. Chem.* **1995**, *99*, 17085.

[42] Ischenko, A.A.; Strand, T.G.; Demidov, A.V.; Spiridonov, V.P. *J. Mol. Struc*t. **1978**, *43*, 227.

[43] Kang, S.K.; Tang, H.; Albright, T.A. *J. Am. Chem. Soc.*, **1993**, *115*, 1971

[44] Benson, M.T.; Cundari, T.R.; Li, Yu; Strohecker, L.A. *Int. J. Quant. Chem.: Quant. Chem. Symp.* **1994**, *28,* 181.

[45] Deng, L.; Ziegler, T. *Organometallics* **1996**, *15,* 3011.

[46] (a) *Spectroscopic Properties of Inorganic and Organometallic Compounds.* (The

---

Royal Society of Chemistry, Garden City Press Limited, London, 1984), Vol. 16, p.762. (b) Dobs, K.D.; Hehre, W.J. *J. Comput. Chem.* **1987**, *8,* 861. (c) Benson, M.T.; Cundari, T.R.; Lim, S.J.; Nguyen, H.D.; Pierce-Beaver, K. *J. Am. Chem. Soc.* **1994**, *116*, 3966. (d) Sosa, C.; Andzelm, J.; Elkins, B.C.; Wimmer, E.; Dobbs, K.D.; Dixon, D.A. *J. Phys. Chem.* **1992**, *96,* 6630. (e) Russo, T.V.; Martin, R.L.; Hay, P.J. *J. Chem. Phys.* **1995**, *102,* 9315.

[47] Rosenkilde, C.; Voyiatzis, G.; Jensen, V.R.; Ystens, M.; ∅stvold, T. *Inorg. Chem.* **1995**, *34,* 4360.

[48] (a) *Structure Data of Free Polyatomic Molecules*, Springer, Berlin **1987** (b) *Modern Organic Chemistry*, Marcel Dekker, New York, **1973**, p. 421.

[49] Figueira, R.R.; Fournier, L.L.; Varetti, E.L. *Spectrochim Acta Part A* **1982***, 38,* 965.

[50] Beattie, I.R.; Livingstone, K.M.S.; Reynolds, D.J.; Ozin, G.A. *J. Chem. Soc. A.* **1970**, 1210.

[51] Landis, C.R.; Cleveland, T.; Firman, T.K *J. Am.Chem.Soc*. **1995**, *117*, 1859.

[52] Del Bene, J.E.; Person, W.B.; Szczepaniak, K. *J. Phys. Chem.* **1995**, *99,* 10705.

[53] Chase, M.W. *NIST-JANAF Thermochemical Tables, Fourth Edition,, J.Phys.Chem. Ref. Data, Monograph 9,* 1998.

[54] Lubin, L.; Liting, Li, Tobin, J.M. *J. Am. Chem. Soc.* **1997**, *119,* 8574.

[55] Acho, J.A.; Doerrer, L.H.; Lipppard, S.J. Inorg. Chem. **1995**, *34*, 2542.

[56] (a) Zielinski, J.J.; Poirier, R.A.; Peterson, M.R.; Csizmadia, I.G. *J. Comput. Chem.* **1983**, *4*, 419. (b) Nguyen, M.T.; Ha, T.-K. *J. Am. Chem. Soc.* **1984**, *106*, 599. (c) Nguyen, M.T.; Hegarty, A.F.; *J. Am. Chem. Soc.* **1984**, *106*, 1552. (d) McKee, M.L. *J. Phys. Chem.* **1993**, *97*, 13608.

4. Gas-phase reaction in CVD of TiN from $TiCl_4$ and NH_3

4.1 Introduction

Titanium nitride has a unique combination of useful properties (high hardness and melting point, good electric and thermal conductivity, chemical inertness, and excellent adherence to most metals, semi-conductors and insulators) and numerous existing and potential industrial applications. It has been even entitled as "technologically the most important nitride" [57] In microelectronics TiN has a broad area of applications as a low resistance contact and a diffusion barrier for metallization.[58]

Several precursors such as $TiCl_4$,[57,59] $Ti(NMe_2)_4$, [57, 60, 61] $Ti(NEt_2)_4$[57, 60, 62] and $Ti(NMeEt)_4$ [63] have been applied in titanium nitride deposition. The reaction of $TiCl_4$ with N_2 and H_2 (eq 1) has been used at first for TiN deposition at high (~900-1200°C) temperatures. The application of ammonia as a source of nitrogen (eq 2) lowers the temperature to ~500°C, [59] which opens this process for a broader application in microelectronic industry.

$$2TiCl_4 + N_2 + 4H_2 \rightarrow 2TiN + 8HCl \qquad (1)$$

$$6TiCl_4 + 8NH_3 \rightarrow 6TiN + 24HCl + N_2 \qquad (2)$$

Organometallic precursors such as $Ti(NR_2)_4$, contain an excess of nitrogen. However, simple thermal decomposition leads to a high carbon contamination, while addition of ammonia improves the film composition and also lowers the process temperature.

During the CVD process few types of (subsequent) processes occur. At lower temperatures $TiCl_4$ and ammonia form donor-acceptor complexes, presumably with one or two ammonia, e.g. $TiCl_4 \cdot NH_3$ and $TiCl_4 \cdot 2NH_3$. Fast complexation is followed by slow ammonolysis. At high temperatures Ti(IV) is reduced to Ti(III) in the form of TiN_x film or as a powder. These types of processes (e.g., complex formation, ammonolysis and reduction) are well known in the gas phase and solution chemistry of $TiCl_4$ while their detailed mechanistic description is far from being well understood [64]. In liquid ammonia up to three chlorine atoms are substituted by NH_2 groups, while in methylamine only two TiCl bonds are ammonolysed. Trimethylamine reduces Ti (IV) to Ti(III) and forms a complex with resulting titanium trichloride – $TiCl_3 \cdot 2NH_3$. Saeki et al. [65] observed $TiCl_4 \cdot 5NH_3$ as a product of the gas phase reaction between $TiCl_4$ and NH_3 at a temperature below 220°C, which presumably consists of a mixture of NH_4Cl with an ammonia adduct of the partially aminolyzed $TiCl_4$. In the temperature range between 220°C and 430°C $TiCl_4 \cdot 5NH_3$ decomposes to ClTiN, which at higher temperatures reacts with ammonia forming TiN_x powder[65]. The thermochemistry of gas-phase species relevant to TiN CVD has been studied theoretically by Allendorf et al,[66] who reported a 17 kcal/mol exothermic enthalpy of the 1:1 complex formation between $TiCl_4$ and NH_3 and a 20 kcal/mol endothermic decomposition energy of this complex toward Cl_3TiNH_2 and HCl. Ti-C and Ti-N bond energies have been also reported in ref.66. It was found that the Ti-Cl bond energies computed at CCSD(T) and at BLYP levels are in good agreement with each other. Structures and energetics of some intermediates in TiN CVD: $TiCl_m(NH_2)_n$, $TiCl_m(NH_2)_nNH$ and $TiCl_m(NH_2)_nN$ have been calculated by Schlegel et al [67] using a variant of G2 level theory.

The formation of the metal-ligand multiple bond is the next processes which was observed during CVD of transition metal nitrides. Winter et al[68] provided evidence of imidos in TiN CVD from $TiCl_4$ and *tert*-butylamine using mass spectrometry. Imido complexes are also supposed to play important role in the synthesis of solid-state M_3N_4 (M=Zr, Nb), Mo_2N_3 and VN by the addition of ammonia to $M(NR_2)_4$.[69]

In this chapter theoretical study of subsequent steps of $TiCl_4$ ammonolysis and 1:1 and 1:2 complexes of $TiCl_{4-x}(NH_2)_x$ (x = 1-4) molecules with ammonia are presented. Quantum chemical calculations provide structures, energies and vibrational frequencies for further thermodynamic equilibrium and kinetics analysis of the leading processes. As next, the possible intermediacy of compounds involving Ti=N double bond in CVD of TiN from $TiCl_4$ and NH_3 is considered.

4. 2 Computational Methods

Molecular geometries have been optimized using three different theoretical methods: HF, MP2 and B3LYP as implemented in the Gaussian98 program package. Analytical harmonic frequencies have been computed at the HF level of theory for all stationary structures and at the B3LYP and MP2 levels for selected molecules. HF vibrational frequencies are scaled by 0.89. Using B3LYP optimized geometries single point coupled cluster CCSD(T) calculations have been performed.[a] The relative energies presented in the work include zero-point energy (ZPE) corrections.

All calculations were performed using a quasi-relativistic effective core potential (ECP) for titanium with a valence basis set (441/2111/41), which was derived from the [55/5/5] valence basis set of Hay and Wadt. An ECP with a valence basis set (4/5)/[2s3p] [70] extended by a d-type polarization function [71] was used for chlorine. It has been demonstrated for a representative set of transition metal complexes [72] that ECP's generated for *ab initio* methods can be applied in DFT-based calculations as well. Standard 6-31G* basis sets [73] were used for nitrogen and hydrogen atoms. If not specified otherwise relative energies discussed in this work are given at the CCSD(T)//B3LYP level and the structural parameters for the B3LYP optimized geometries.

The kinetic simulations were performed within a model of well-stirred reactor at temperatures 300 – 1200 K and residence times 0.1-2 s. These calculations were done using CHEMKIN[74] program package.

---

[a] For some reactions it was impossible to located transtition state structures at correlated levels. In these cases CCSD(T) single point calculations were carried out at the HF optimized geometries.

4.3 Complex formation and ammonolysis

Titanium tetrachloride reacts with gaseous or liquid ammonia by forming adducts, which are further ammonolyzed in excess of ammonia [75]. When $TiCl_4$ and NH_3 are mixed at temperatures below 530K, also six-coordinated complexes with ammonia are observed[76],[77]. In chapter the following four-coordinated molecules: $TiCl_4$, $TiCl_3NH_2$, $TiCl_2(NH_2)_2$, $TiCl(NH_2)_3$ and $Ti(NH_2)_4$ and their 1:1 and 1:2 complexes with ammonia are considered first.

4.3.1 Four-coordinated titanium containing molecules

The optimized geometries of $TiCl_4$, $TiCl_3NH_2$, $TiCl_2(NH_2)_2$, $TiCl(NH_2)_3$ and $Ti(NH_2)_4$ at B3LYP, HF and MP2 level are presented at Figure 4.1. Experimental structures and vibrational frequencies are available only for $TiCl_4$ [78] (Table 4.1). The Ti-Cl bond length determined by gas electron diffraction is 2.170 Å. Thus all three methods, HF, MP2 and B3LYP, are within 0.01 Å of the Ti-Cl bond length (see Fig. 4.1a). B3LYP gives a bigger and HF and MP2 a smaller value compared with the experimental results. In earlier HF all electron[79], HF pseudopotential[80] and local density functional studies[81] the Ti-Cl bond length in $TiCl_4$ was computed as 2.165 Å, 2.184 Å and 2.167 Å, respectively.

The calculated HF vibrational frequencies are in a good agreement with experimental values [78] and previous theoretical studies using HF ECP[80]and LDF[81] approaches (see Table 4.1). The vibrational modes computed at the B3LYP and at the MP2 approaches are higher than the experimental values.

Consecutive substitution of Cl by NH_2 in the $TiCl_{4-x}(NH_2)_x$ (x = 0-4) series leads to elongation of both Ti-Cl and Ti-N bond lengths. Thus the first two molecules in the series, $TiCl_4$ and $TiCl_3(NH_2)$, have the shortest Ti-Cl (2.176 Å) and Ti-N (1.855 Å) bond lengths, respectively, while the last two, $TiCl(NH_2)_3$ (Ti-Cl = 2.259 Å and $Ti(NH_2)_4$, (Ti-N = 1.912 Å) have the longest ones. An earlier RHF ECP[82] study of $TiClH_2(NH_2)$ and $TiH_2(NH_2)_2$ predicts Ti-N bonds to be 1.86 Å and 1.89 Å, respectively. This is in good agreement with

1.855 Å and 1.867 Å obtained in this work for the Ti-N bonds in $TiCl_3(NH_2)$ and $TiCl_2(NH_2)_2$ respectively. Experimental geometries for these compounds are not available. However, theoretical values of the TiN bond length in $Ti(NH_2)_4$ (1.912 Å) and in $TiCl(NH_2)_3$ (1.855 Å) are in good agreement with experimental data in the substituted compounds $Ti(NMe_2)_4$ (1.917 Å)[83] and Cl_3TiCl_3 NEt_2 (1.852 Å)[84].

Amino groups attached to Ti in the calculated molecules are planar, which indicates a delocalization of the nitrogen lone pairs towards the empty d orbitals of titanium.

Table 4.1. Computed and experimental vibrational frequencies (in cm^{-1}) for TiCl4.

	HF	**B3LYP**	**MP2**	**Calc.[a)]**	**Calc.[b)]**	**Exp.[c)]**
$\nu_1(a_1)$	389	397	407	403	377	388
$\nu_2(e)$	112	121	122	117	96	118
$\nu_3(t_2)$	484	514	533	518	507	497
$\nu_4(t_2)$	138	144	141	144	129	139

[a] from ref.83 [b] from ref. 84. [c] from ref. 81

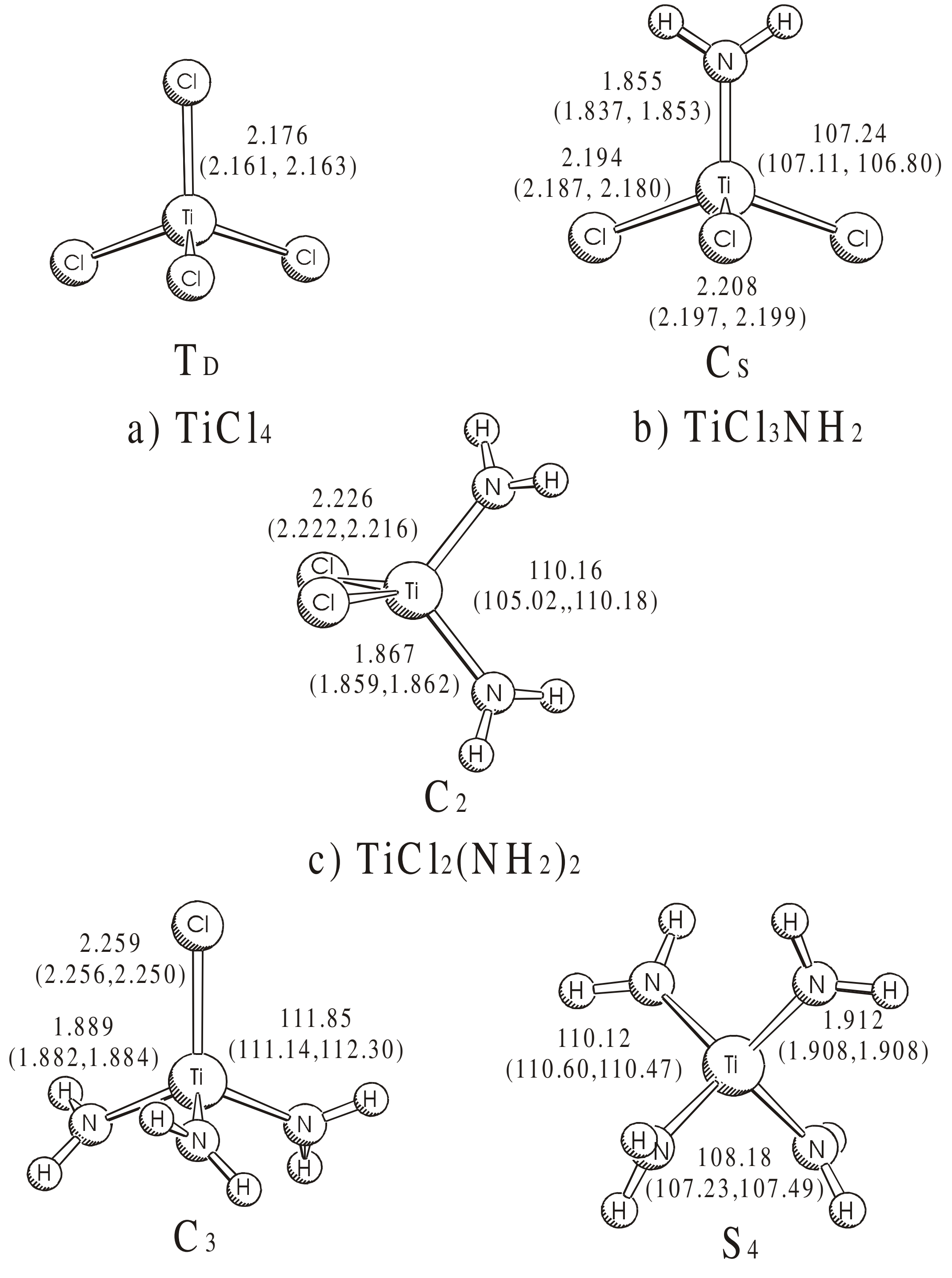

T_D

a) $TiCl_4$

C_S

b) $TiCl_3NH_2$

C_2

c) $TiCl_2(NH_2)_2$

C_3

d) $TiCl(NH_2)_3$

S_4

e) $Ti(NH_2)_4$

Fig. 4.1 B3LYP optimized geometries of four coordinated titanium compounds: a) $TiCl_4$, b) $TiCl_3NH_2$, c) $TiCl_2(NH_2)_2$, d) $TiCl(NH_2)_3$, e) $Ti(NH_2)_4$. HF and MP2 values are given in parentheses.

4.3.2 Five-coordinated complexes

Tetracoordinated titanium molecules $TiCl_{4-x}(NH_2)_x$, form relatively strong donor-acceptor complexes with ammonia. The energy of the $TiCl_4:NH_3$ complex formation (ΔH_c) (see Table 4.2) varies from 18.3 kcal/mol (HF and BL3LYP) to 23.6 kcal/mol (MP2 and CCSD(T)) which can be compared with previous theoretical values of 24.3 and 17 kcal/mol calculated using MP2 ECP[85] and BLYP [66] methods, respectively.

The complexes of $TiCl_x(NH_2)_{4-x}$ with ammonia have bipyramidal structures. For the $TiCl_4:NH_3$ complex two conformations (geometric isomers)[a] can be visualized with NH_3 occupying the axial or equatorial positions:

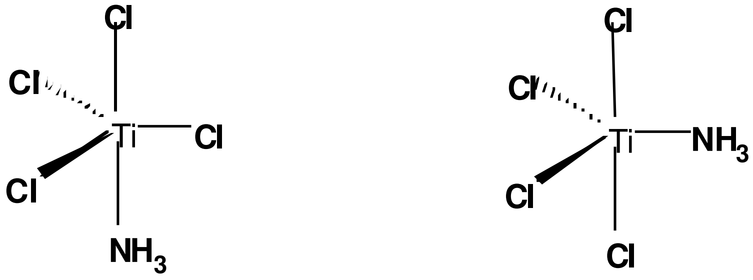

1-ax **1-eq**

Scheme 4.1

---

[a] Although *geometric isomers* may be considered as a more appropriate term for considering bipyramodal structures with different axial-equatorial configurations, we call them *conformations* in this paper, since energy variations for this type of *isomerism* is in a few kcal/mol range.

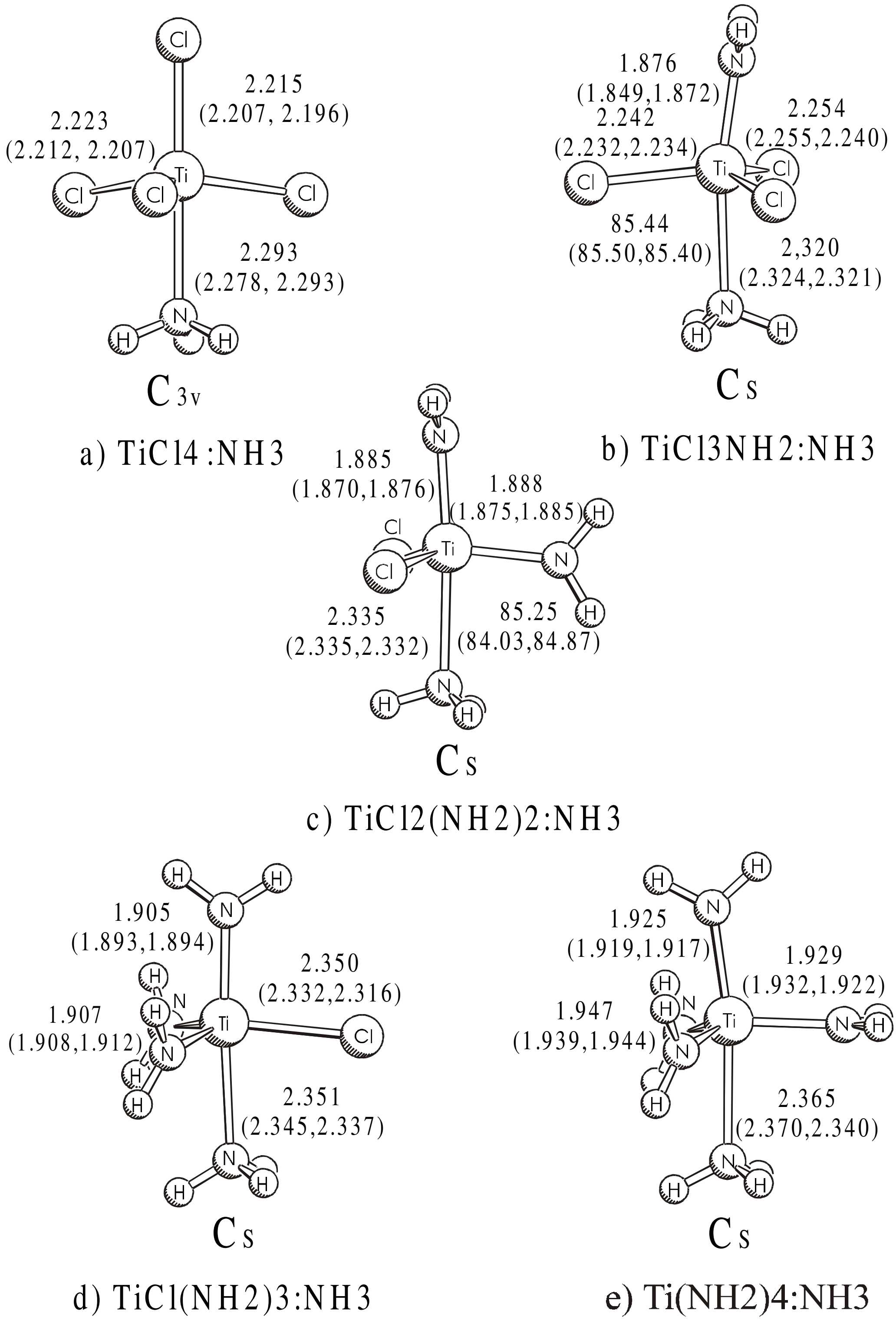

a) TiCl4:NH3

b) TiCl3NH2:NH3

c) TiCl2(NH2)2:NH3

d) TiCl(NH2)3:NH3

e) Ti(NH2)4:NH3

Fig. 4.2 B3LYP optimized geometries of five coordinated titanium complexes with ammonia: a) $TiCl_4$:NH_3, b) $TiCl_3NH_2$:NH_3, c) $TiCl_2(NH_2)_2$:NH_3, d) $TiCl(NH_2)_3$:NH_3 , e) $Ti(NH_2)_4$:NH_3 . HF and MP2 values are given in parentheses.

Structure **1-eq** collapses into **1-ax** during optimization at the B3LYP level and thus, has not been investigated further. The Ti-Cl bond length for of the axial chlorine atom in **1-ax** (see also Figure 4.2a) is shorter compared to the equatorial ones, which is unusual for bipyramidal structures [86]. An elongation of the equatorial bonds in **1-ax** can be explained by hydrogen bonding between equatorial chlorine atoms and the hydrogen atoms of ammonia. Similar effect was observed in pentacoordinated oxichlorides $TaCl_4(OH)$ and $TaCl_3(OH)_2$.

Table 4.2. Complex formation energies (ΔH_c) (in kcal/mol) for $TiCl_{4-x}(NH_2)_x$:yNH_3 (x =0-4; y = 1-2) adducts.[a)]

$TiCl_{4-x}(NH_2)_x$:yNH_3		**HF**	**B3LYP**	**MP2**	**CCSD(T)**
$TiCl_4$	1:1	18.3	18.3	23.6	23.6
	1:2	35.9 (35.8)[b)]	34.7 (32.9)[b)]	47.4 (43.8)[b)]	47.4 (44.9)[b)]
$TiCl_3NH_2$	1:1	17.1	17.5	23.3	23.2
	1:2	34.7	33.6	46.9	46.8
$TiCl_2(NH_2)_2$	1:1	13.9	13.7	19.5	19.5
	1:2	27.9	28.0	40.4	40.5
$TiCl(NH_2)_3$	1:1	12.0	10.9	16.2	16.1
	1:2	19.9	17.7	33.1	29.5
$Ti(NH_2)_4$	1:1	7.2	7.9	12.8	13.3
	1:2	6.6	7.5	16.6	17.2

[a] Most stable conformations of complexes are considered. See text for details.

[b] The ΔH_c values for the *trans* conformations are given in parenthesis.

Four possible conformations with regard to axial and equatorial orientation can be visualized for the $TiCl_3NH_2$:NH_3 complex:

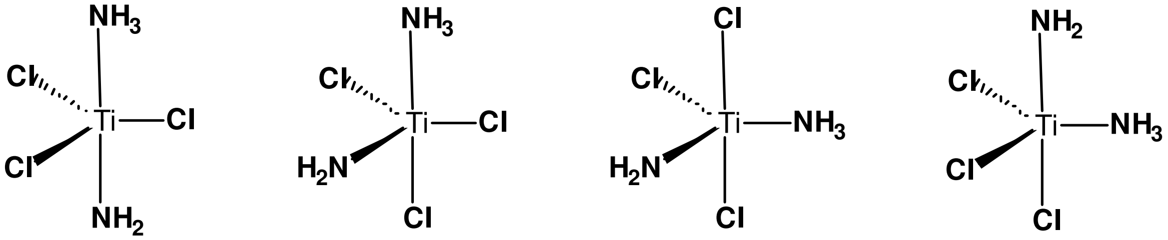

2-ax,ax **2-ax,eq** **2-eq,eq** **2-eq,ax**

Scheme 4.2

All methods except HF predict the **2-ax,ax** conformation (NH_2 and NH_3 in axial positions) to be the most stable one. The energy difference is small (~1kcal/mol) at all four theory levels considered (see Table 4.3). The **2-eq,ax** conformer collapses into **2-ax,eq** during optimization at the B3LYP level and thus, was not considered further. The Ti-Cl and Ti-NH_3 bond lengths in **2-ax,ax** are elongated compared to **1-ax** (see Figures 2a and 2b). Thus similar to the tetracoordinated molecules, substitution of Cl by NH_2 leads to elongation of *all* bonds in their complexes with ammonia. This effect is apparent in other NH_3 complexes discussed below. The ΔH_c value of the most stable $TiCl_3NH_2$:NH_3 conformer, **2-ax,ax**, is very similar to that one of $TiCl_4$:NH_3 (see Table 2). As well as for $TiCl_4$:NH_3, the complex formation energies for $TiCl_3NH_2$:NH_3 appear to be higher at MP2 and CCSD(T) compared to the values computed with the HF and the B3LYP approaches.

Table 4.3. Relative energies of $TiCl_3NH_2$:NH_3 conformers in kcal/mol (see Scheme 4.2).

	HF	**B3LYP**	**MP2**	**CCSD(T)**
2-ax,ax	0.0	0.0	0.0	0.0
2-ax,eq	-0.2	1.2	1.0	0.8
2-eq,eq	2.8	2.6	3.1	3.3
2-eq,ax	Collapses	into	2-ax,eq	

$TiCl_2(NH_2)_2$:NH_3 has five possible arrangements of the ligands with regard to their positions in a bipyramidal structure:

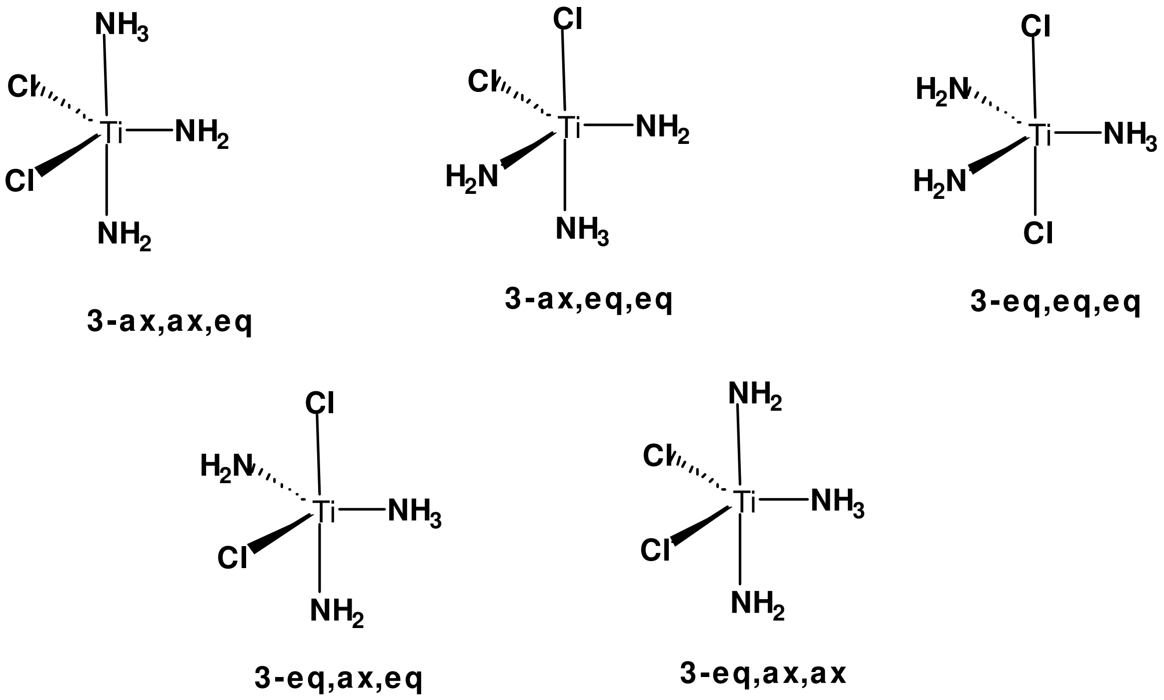

3-ax,ax,eq **3-ax,eq,eq** **3-eq,eq,eq**

3-eq,ax,eq **3-eq,ax,ax**

Scheme 4.3

Similar to the $TiCl_3NH_2:NH_3$ complex, the **3-ax,ax,eq** conformer of $TiCl_2(NH_2)_2:NH_3$ with NH_2 and NH_3 ligands in the axial positions has been found to be the most stable one at the B3LYP level. Somewhat unexpectedly, another conformation with an axial position of ammonia, **3-ax,eq,eq**, was found to be slightly higher in energy compared to **3-eq,eq,eq** where all nitrogens are located in the equatorial positions. Two other conformations **3-eq,ax,eq** and **3-eq,ax,ax** collapsed to **3-ax,eq,eq** and to **3-eq,eq,eq**, respectively. The most stable conformation, **3-ax,ax,eq** were also computed at the HF, MP2 and CCSD(T)//B3LYP levels of theory (see Figure 4.2c).

While the complex formation energies are close for $TiCl_4$ and $TiCl_3NH_2$, the following steps of the ammonolysis reduce ΔH_c by 3-4 kcal/mol (see Table 4.2). The drop in ΔH_c at the second and subsequent steps of the ammonolysis can be explained as follows. The first substitution of Cl by NH_2 takes place in an axial position, while in further steps the Cl atoms are replaced in the equatorial positions. Completely ammonolyzed $Ti(NH_2)_4$ forms a 1:1 adduct with NH_3 with an energy of only 13.3 kcal/mol, which is about ½ of the ΔH_c value of $TiCl_4:NH_3$. Although $TiCl(NH_2)_3:NH_3$ may have four conformations with different orientation of the ligands in the bipyramidal structure, only the isomer with axial positions of NH_2 and NH_3 (see Figure 4.2d) was computed. This isomer is expected to be the lowest one according to conformational studies of $TiCl_3NH_2:NH_3$ and $TiCl_2(NH_2)_2:NH_3$. For the $Ti(NH_2)_4:NH_3$ complex the conformation with an axial orientation of ammonia (see Figure 4.2e) was calculated.

4.3.3 Six-coordinated complexes

Titanium tetrachloride forms a six-coordinated adduct with the second NH_3 molecule with almost the same $Ti-NH_3$ bond strength as the first one (see Table 4.2). There are two possible $TiCl_4:2NH_3$ conformers, e.g. with *cis* and *trans* orientation of NH_3 in the tetragonal bipyramide structure of the complex:

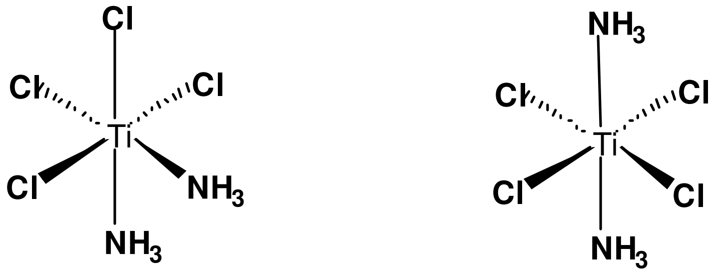

4-*cis* **4-*trans***

Scheme 4.4

Both conformers have almost the same energy at the HF level, while the correlated methods show the **4-*cis*** form to be 2-3 kcal/mol more stable compared to **4-*trans*** (Table 4.2). The relatively small energy difference between the *cis* and *trans* forms of $TiCl_4$:$2NH_3$ can be explained by a balance of van-der-Waals repulsion of ligands (larger in the **4-*cis*** conformer) and the $TiCl_4$ deformation energy (larger in the **4-*trans*** conformer) (see Figures 4.3a and 4.3b). Four other 1:2 complexes have been computed only for the *cis* conformation of two NH_3 coordinated to Ti (see Figure 4.3c-f).

Substitution of chlorine atoms by NH_2 in $TiCl_x(NH_2)_{4-x}$:$2NH_3$ leads (like in the case of the four-coordinated molecules and the corresponding 1:1 complexes) to elongation of the Ti-Cl and Ti-N bonds. A comparison of the TiCl and TiN bonds in the four- , five-, and six-coordinated complexes reveals an additional effect of elongation of both bonds when the coordination number of Ti increases through formation of dative Ti-NH_3 bonds.

Similar to 1:1 complexes ΔH_c values of the 1:2 complexes of $TiCl_4$ and $TiCl_3NH_2$ with ammonia are close to each other. The value of ΔH_c drops again with further increase of the number of NH_2 groups in the complexes (see Table 4.2). Note, that the ΔH_c values of the 1:2 complexes are approximately twice as large as the energies of the 1:1 adducts, except for $Ti(NH_2)_4$. In the latter case the formation of the second Ti$\leftarrow$$NH_3$ donor-acceptor bond is accompanied by a smaller energy release than the first one.

The results of the NBO analysis performed at the B3LYP level are shown in Table 4.4. The positive charge at Ti increases along with increasing number of NH_2 groups in

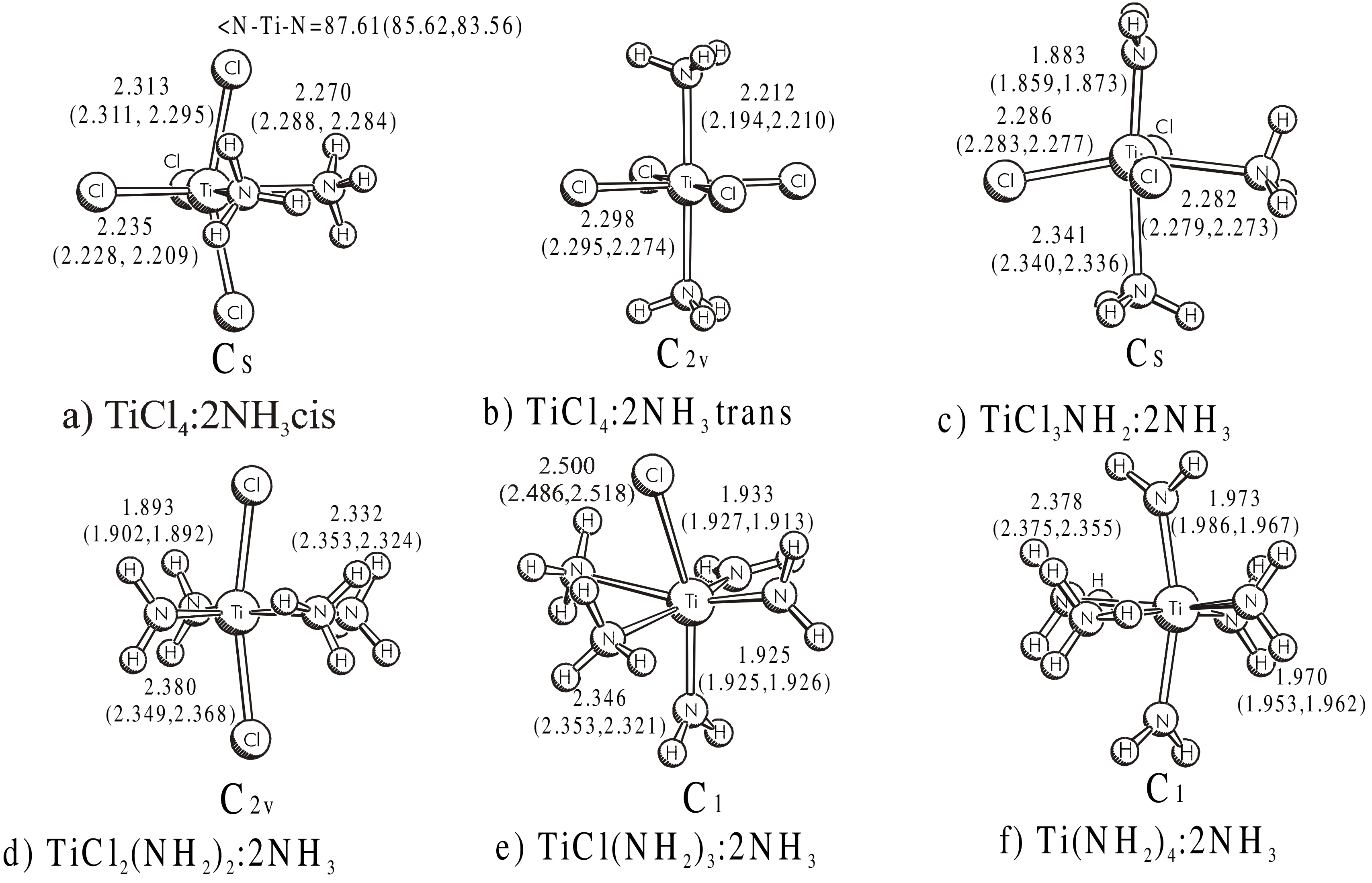

a) $TiCl_4$:$2NH_3$cis

b) $TiCl_4$:$2NH_3$ trans

c) $TiCl_3NH_2$:$2NH_3$

d) $TiCl_2(NH_2)_2$:$2NH_3$

e) $TiCl(NH_2)_3$:$2NH_3$

f) $Ti(NH_2)_4$:$2NH_3$

Fig. 4.3 B3LYP optimized geometries of six-coordinated titanium complexes with two NH_3: a) $TiCl_4$:$2NH_3$ cis, b) TiCl4:$2NH_3$ trans c) $TiCl_3NH_2$:$2NH_3$, d) $TiCl_2(NH_2)_2$:$2NH_3$, e) $TiCl(NH_2)_3$:$2NH_3$, f) $Ti(NH_2)_4$:$2NH_3$

four-coordinated molecules and in 1:1 and 1:2 complexes. Thus the electrostatic component the dative Ti←NH$_3$ bond should *increase* when the number of the NH2 groups increases. However, electrostatic repulsion between the ligands leads to the *decrease* of ΔH_c with increasing number of NH$_2$ groups in the molecule. Complexation by ammonia reduces the positive charge at the central atom, in agreement with dative character of the Ti←NH$_3$ bond.

Table 4.4 B3LYP NBO charges (q) at Ti atom in calculated complexes.

	$TiCl_x(NH_2)_{4-x}$	**$TiCl_x(NH_2)_{4-x}$:NH_3**	**$TiCl_x(NH_2)_{4-x}$:2NH_3**
$TiCl_4$	0.67	0.61	0.50
$TiCl_3NH_2$	0.92	0.84	0.74
$TiCl_2(NH_2)_2$	1.12	1.06	0.97
$TiCl(NH_2)_3$	1.30	1.25	1.19
$Ti(NH_2)_4$	1.46	1.33	1.25

4.3.4 Thermochemistry and mechanism of ammonolysis.

Substitution of the Cl atoms by NH$_2$ groups is endothermic, and the heat of reaction increases with the number of amino groups in the molecule (see Table 4.5). Since substitution of Cl by NH$_2$ increases steric repulsion between ligands, ammonolysis of the complexes is more endothermic than similar reactions of four-coordinated molecules. It is well known that an excess of ammonia replaces up to three Cl atoms while full ammonolysis does not occur[75]. This holds for gas phase reactions of TiCl$_4$ and NH$_3$ and for the reactions of TiCl$_4$ with liquid NH$_3$. Since the reaction of TiCl$_4$ with NH$_3$ consists of two steps, *exothermic* complex formation (presumably with two ammonia) and *endothermic* substitution of Cl by NH_2 groups, the *overall* reaction energies for the different stages of ammonolysis were calculated (see Table 4.6). An *exothermic* effect of formation of an H-bonded adduct of NH_3 and HCl (10-11 kcal/mol)[87] was considered additionally. With such approximations a substitution of *up to three* Cl atoms by NH_2 groups appears to be *exothermic*, while the complete ammonolysis of $TiCl_4$ into $Ti(NH_2)_4$ is *endothermic*. This provides a qualitative explanation for the experimental observation of *incomplete* ammonolysis of titanium tetrachloride. For an accurate estimation of the free energy of ammonolysis the entropy changes and the solvolysis of reactants and products have to be taken into account.

Table 4.5. Zero Kelvin heats of the subsequent steps of ammonolysis of $TiCl_{4-x}(NH_2)_x$ molecules and their 1:1 and 1:2 complexes with ammonia (in kcal/mol).

Reaction	x=	HF	B3LYP	MP2	CCSD(T)
$TiCl_4{:}xNH_3 + NH_3 \rightarrow TiCl_3NH_2{:}xNH_3 + HCl$	0	9.2	10.5	12.1	10.8
	1	12.3	13.2	14.2	13.0
	2	10.5	11.7	12.5	11.4
$TiCl_3NH_2{:}xNH_3 + NH_3 \rightarrow TiCl_2(NH_2)_2{:}xNH_3 + HCl$	0	13.4	13.2	14.9	13.5
	1	16.6	17.0	18.7	17.2
	2	20.2	18.8	21.4	19.7
$TiCl_2(NH_2)_2{:}xNH_3 + NH_3 \rightarrow TiCl(NH_2)_3{:}xNH_3 + HCl$	0	20.0	19.2	21.2	19.7
	1	21.9	22.0	24.6	23.1
	2	28.0	29.5	28.5	30.7
$TiCl(NH_2)_3{:}xNH_3 + NH_3 \rightarrow Ti(NH_2)_4{:}xNH_3 + HCl$	0	25.6	25.2	27.8	26.0
	1	30.4	28.3	31.1	28.8
	2	38.9	35.3	44.3	38.3

Table 4.6. Zero Kelvin heats of the subsequent stages of aminolysis of $TiCl_4$ accompanied by 1:2 complex formation with ammonia (in kcal/mol).[a]

Reaction	HF	B3LYP	MP2	CCSD(T)
$TiCl_4 + 4NH_3 \rightarrow TiCl_3NH_2:2NH_3 + NH_3:HCl$	-36.5	-34.1	-45.8	-47.0
$TiCl_4 + 6NH_3 \rightarrow TiCl_2(NH_2)_2:2NH_3 + 2NH_3:HCl$	-27.3	-26.3	-35.5	-38.3
$TiCl_4 + 8NH_3 \rightarrow TiCl(NH_2)_3:2NH_3 + 3NH_3:HCl$	-10.3	-7.8	-17.9	-18.6
$TiCl_4 + 10NH_3 \rightarrow Ti(NH_2)_4:2NH_3 + 4NH_3:HCl$	17.6	16.6	15.4	8.8

[a] 11 kcal/mol exothermic energy of NH_3:HCl adduct formation computed in ref. 92a has been uniformly added to all reaction energies.

Transition state energies for the ammonolysis reactions of $TiCl4_{-x}(NH_2)_x$ molecules are presented in Table 4.7. The corresponding structures are given on Figure 4.4. The transition states were located at all three levels for the first two reactions, at HF and MP2 for the third reaction, and only at HF for the last step of the ammonolysis. The transition state structures for all steps of the ammonolysis have very long Ti-Cl distances for the leaving Cl atoms (product like). A comparison of the structures shown in Figure 4.4 at the HF level shows a clear trend of "shifting" the TS geometries toward the dissociation products with proceeding ammonolysis. This observation explains the increasing difficulty in locating the TS structures at correlated levels, which usually have lower barriers and thus more flat potential energy surfaces in the barrier region. Since the B3LYP optimized geometries have not been located, the HF optimized geometries were used for computation of the single point CCSD(T) energies of the transition states for the last two reactions in Table 4.7. To validate their comparison with other CCSD(T) energies computed at the B3LYP optimized geometries, both CCSD(T)//B3LYP and CCSD(T)//HF energies for the transition states in the first two reactions in Table 4.6 were calculated. Although the N···H and H···Cl distances vary substantially in different approaches for the first two TS structures shown in Figure 4.4, CCSD(T) energies computed at HF and B3LYP differ only by ~1 kcal/mol. This comparison confirms the flat character of the potential energy surface in the barrier region. It also validates comparison of the CCSD(T)//HF energies for transition states with the CCSD(T)//B3LYP energies calculated for molecules and complexes.

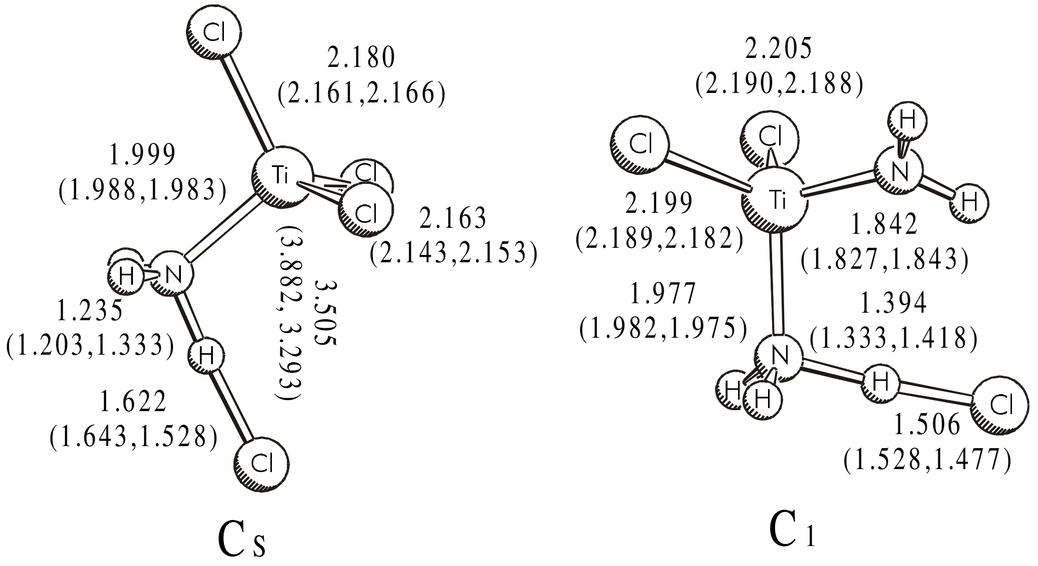

a) $TiCl_4:NH_3$ TS b) $TiCl_3NH_2:NH_3$ TS

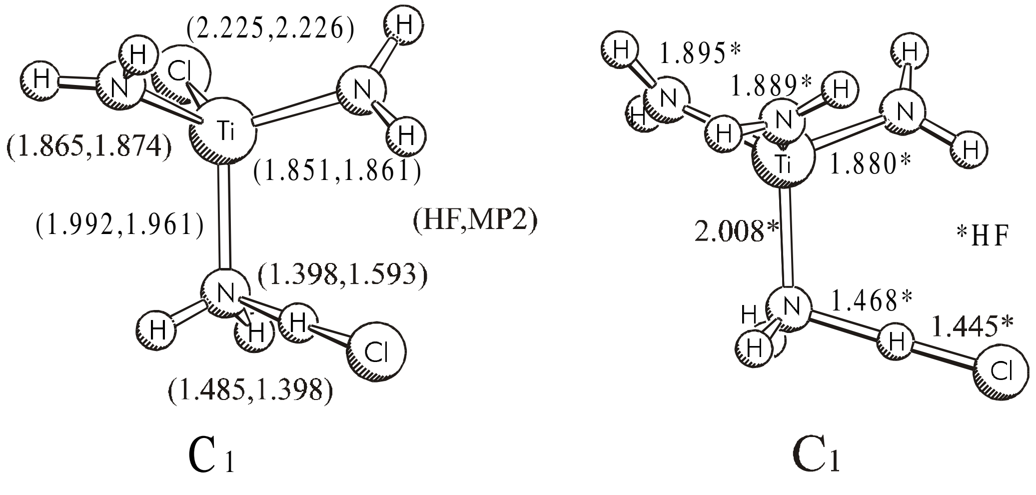

c) $TiCl_2(NH_2)_2:NH_3$ TS d) $TiCl(NH_2)_3:NH_3$ TS

Fig. 4.4 B3LYP optimized geometries of transition states during dichlorinations of a) $TiCl_4:NH_3$, b) $TiCl_3NH_2:NH_3$, c) $TiCl_2(NH_2)_2:NH_3$, d) $TiCl(NH_2)_3:NH_3$. HF and MP2 values are given in parentheses.

Table 4.7 Transition state energies in reactions of substitution of Cl atom by NH_2 group in $TiCl_{4-x}(NH_2)_x$ (x = 0-3) molecules (in kcal/mol).

Reaction	**HF**	**B3LYP**	**MP2**	**CCSD(T)**
$TiCl_4 + NH_3 \rightarrow TiCl_3NH_2 + HCl$	25.1	16.4	18.4	19.0 $^{a)}$ 20.4 $^{b)}$
$TiCl_3NH_2 + NH_3 \rightarrow TiCl_2(NH_2)_2 + HCl$	19.3	9.6	11.3	12.7 $^{a)}$ 13.8 $^{b)}$
$TiCl_2(NH_2)_2 + NH_3 \rightarrow TiCl(NH_2)_3 + HCl$	19.0	---	11.0	13.3 $^{b)}$
$TiCl(NH_2)_3 + NH_3 \rightarrow Ti(NH_2)_4 + HCl$	19.9	---	---	15.5 $^{b)}$

[a]at CCSD(T)//B3LYP; [b] at CCSD(T)//HF

The TS for the first step of ammonolysis of $TiCl_4$ has appreciably higher energy, than subsequent substitution of Cl by NH_2. Only for the first reaction step between $TiCl_4$ and NH_3 and for the second one at the HF level the energies of the transition states are above the product energies (see energy diagram in Figure 4.5 and compare the energies in Tables 4.5 and 4.6). For the following Cl substitution by the NH_2 groups, the transition state energies are below the product energies, which shows that (weak) hydrogen bonded complexes exist as intermediates between the transition states and the products. A similar situation has been revealed in our previous study of $TaCl_5$ hydrolysis in the context of Ta_2O_5 CVD.

For 1:2 complexes TS structures were located at all thee levels only for the first reactions and at the HF level for the second and third reactions. For the last step of ammonolysis it was impossible to locate the TS even at the HF level. Similar to the reactions of four-coordinated molecules with ammonia 1:2 complexes have very loose product-like TS structures for substitution of Cl by NH_2 (Fig 4.6). The computed TS energies for reactions of the 1:2 complexes with ammonia show (Table 4.8) similar trends as the corresponding analogs in Table 4.7. Thus, only the first reaction in Table 4.8 (see

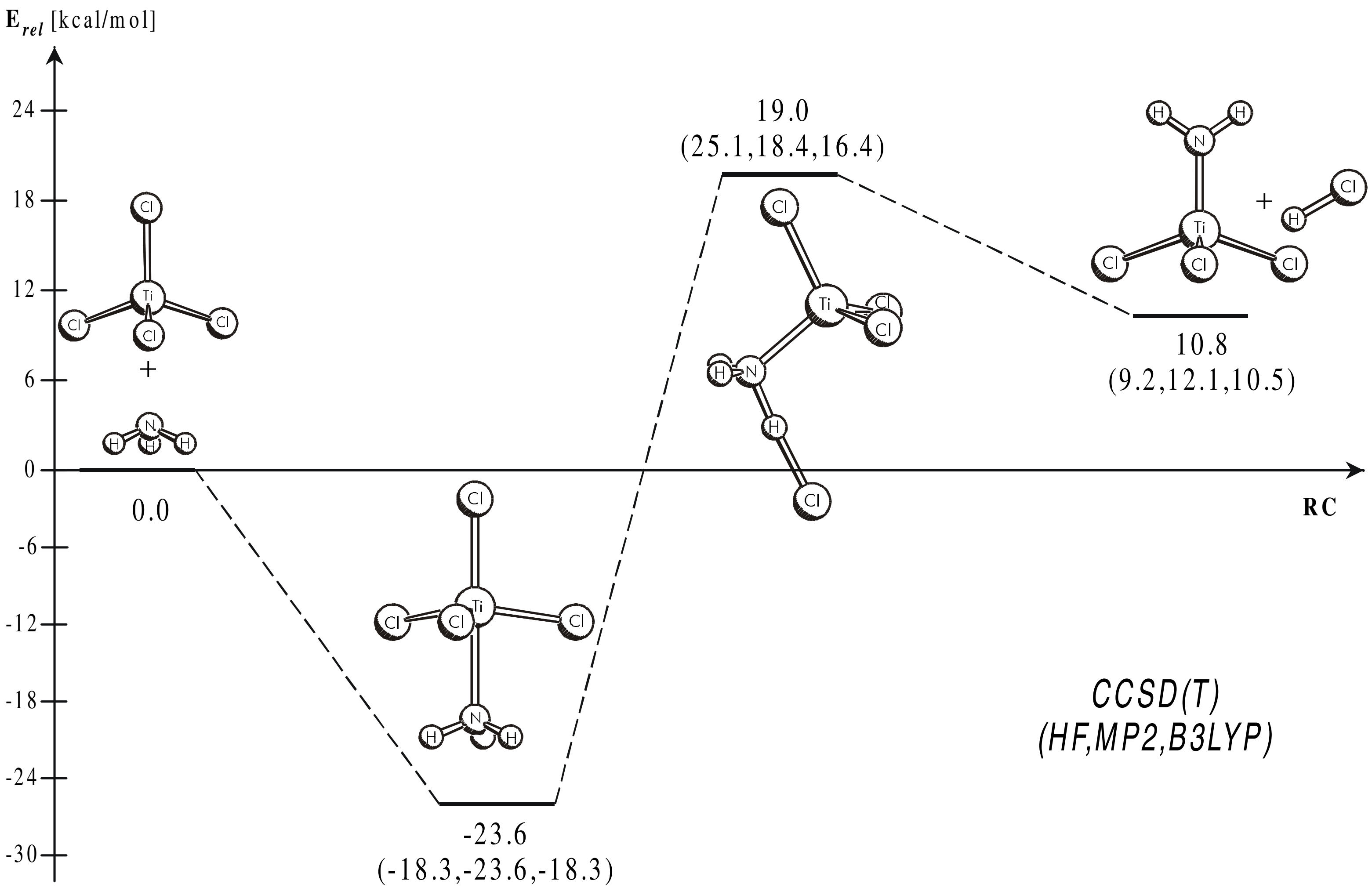

Fig. 4.5 Calculated reaction path for the formation of $TiCl_4$:NH_3 complex and further ammonolysis reactionat CCSD(T). Relative energies at HF, MP2 and B3LYP are given in parentheses.

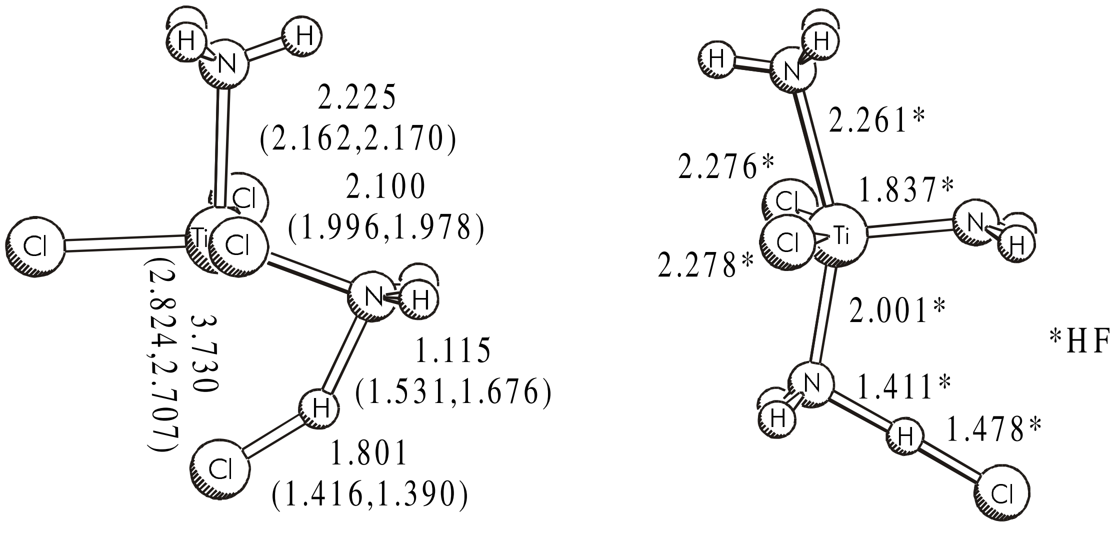

C_s C_s

a) $TiCl_4:2NH_3$ TS b) $TiCl_3NH_2:2NH_3$ TS

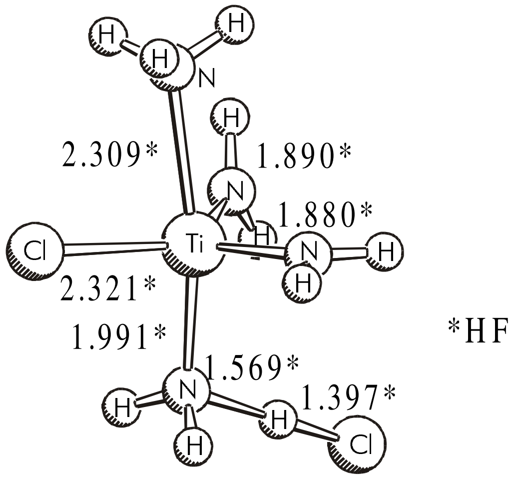

C_1

c) $TiCl_2(NH_2)_2:2NH_3$ TS

Fig. 4.6 B3LYP optimized geometries of transition states during dichlorinations of a) $TiCl_4:2NH_3$, b) $TiCl_3NH_2:2NH_3$, c) $TiCl_2(NH_2)_2:2NH_3$, d) $TiCl(NH_2)_3:2NH_3$. HF and MP2 values are given in parentheses.

also energy diagram on Figure 4.7) has a barrier height larger than the energy of the reaction products and larger than the barriers for two subsequent reactions. Complete reaction profiles calculated at CCSD(T) level for the next steps of ammonolysis are presented at Figs. 4.8-4.10.

Table 4.8. Transition state energies in reactions of substitution of Cl atom by NH_2 group in $TiCl_{4-x}(NH_2)_x$:NH_3 (x = 0-3) complexes (in kcal/mol).

Reaction	HF	B3LYP	MP2	CCSD(T)
$TiCl_4:NH_3 + NH_3 \rightarrow TiCl_3NH_2:NH_3 + HCl$	31.4	15.7	21.2	18.6$^{a)}$ 22.0$^{b)}$
$TiCl_3NH_2:NH_3 + NH_3 \rightarrow TiCl_2(NH_2)_2:NH_3 + HCl$	17.8	---	---	14.3$^{b)}$
$TiCl_2(NH_2)_2:NH_3 + NH_3 \rightarrow TiCl(NH_2)_3:NH_3 + HCl$	18.3	---	---	14.6$^{b)}$
$TiCl(NH_2)_3:NH_3 + NH_3 \rightarrow Ti(NH_2)_4:NH_3 + HCl$	---	---	---	---

[a] at CCSD(T)//B3LYP; [b] at CCSD(T)//HF.

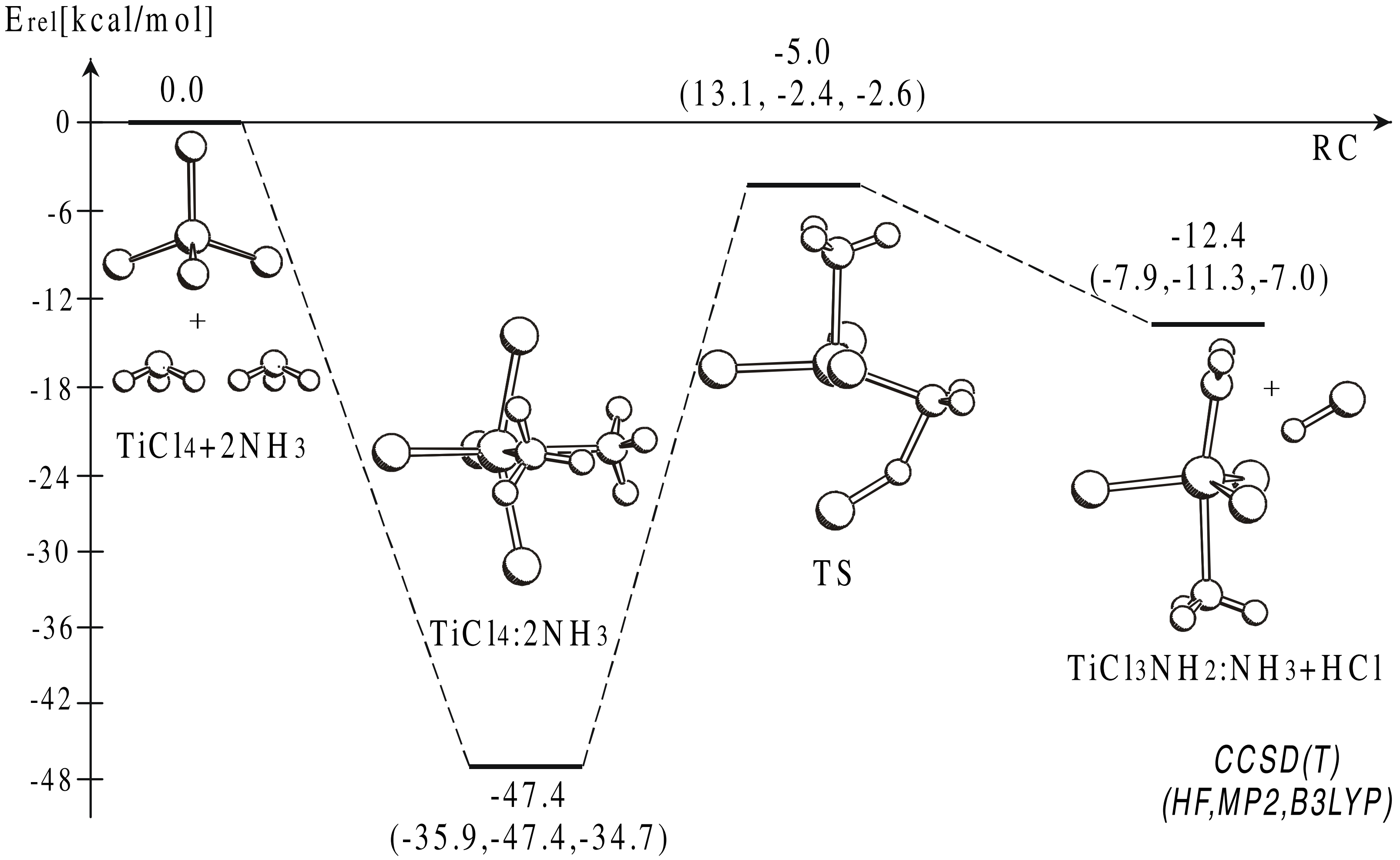

Fig. 4.7 Calculated reaction path for the formation of $TiCl_4$:2NH_3 complex and further ammonolysis reaction at CCSD(T). Relative energies at HF, MP2 and B3LYP are given in parentheses.

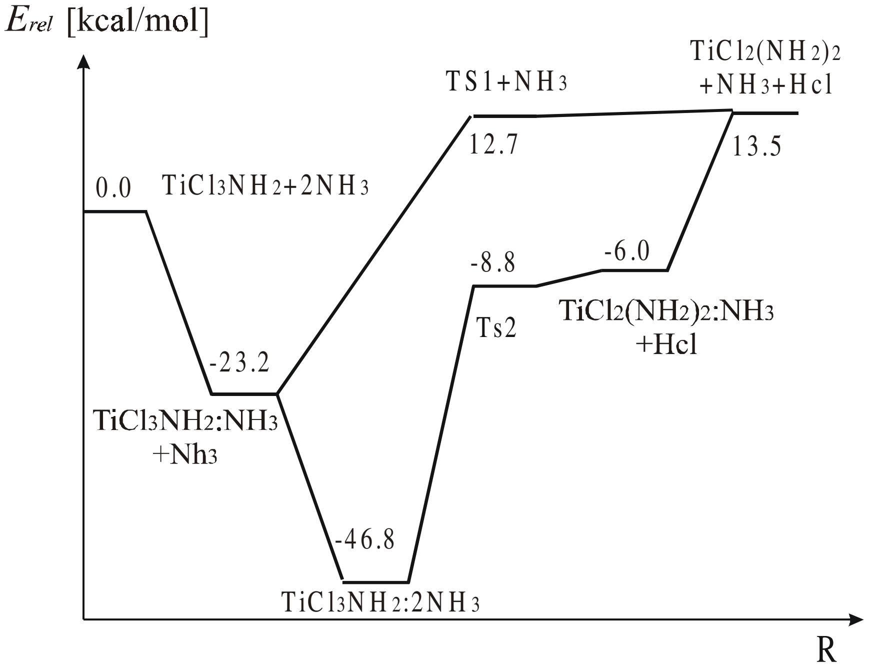

Fig. 4.8 Calculated reaction paths for the formation of 1:1 and 1:2 complexes of $TiCl_3NH_2$ with NH_3 and further ammonolysis at CCSD(T).

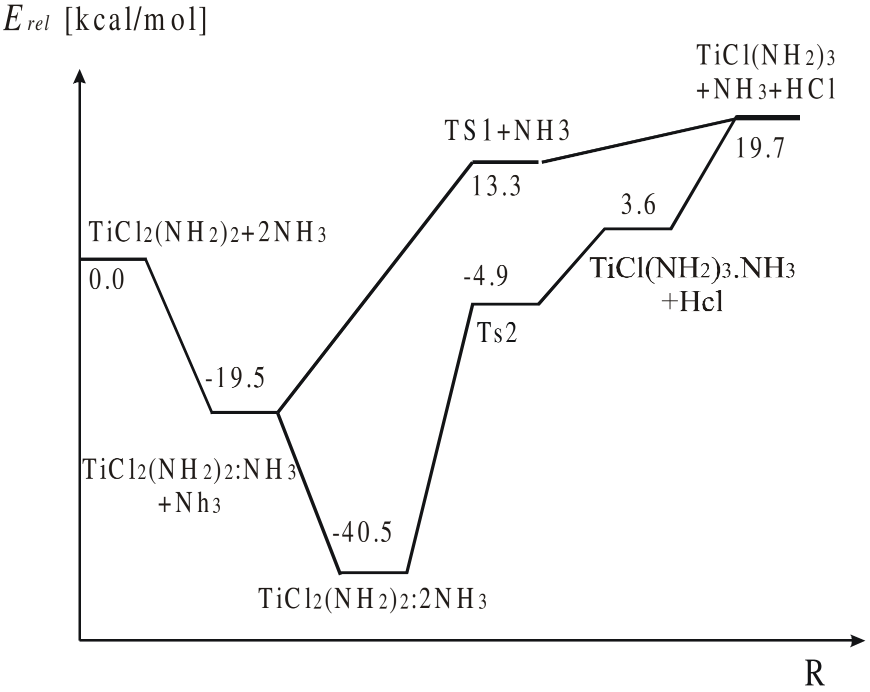

Fig. 4.9 Calculated reaction paths for the formation of 1:1 and 1:2 complexes of $TiCl_2(NH_2)_2$ with NH_3 and further ammonolysis at CCSD(T).

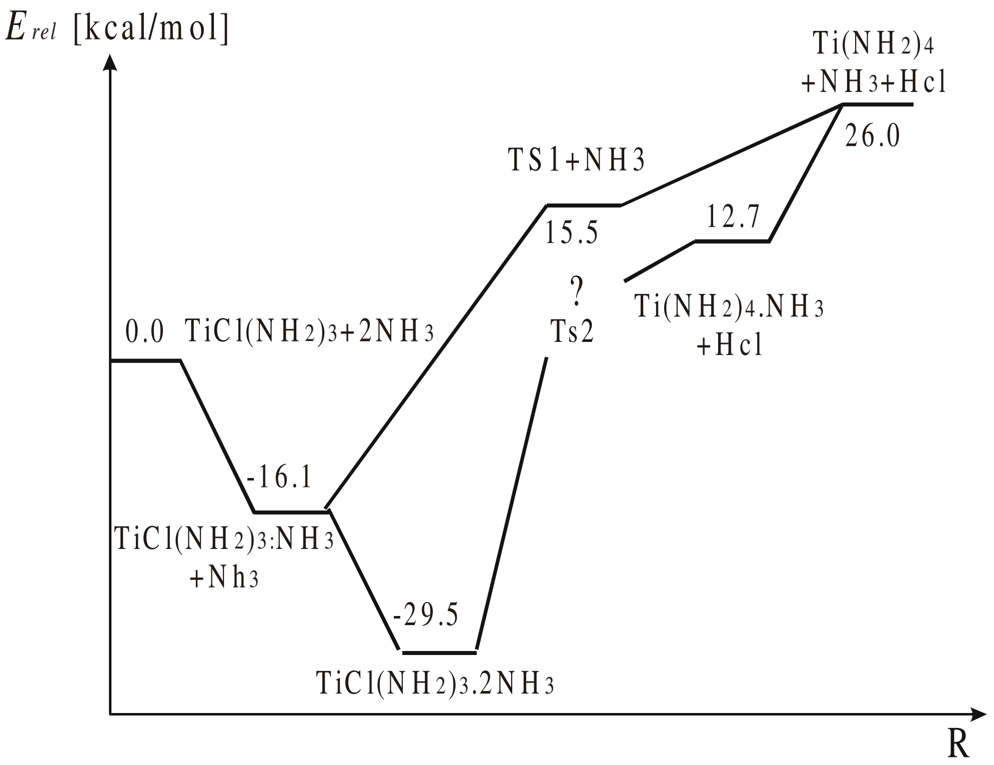

Fig. 4.10 Calculated reaction paths for the formation of 1:1 and 1:2 complexes of $TiCl(NH_2)_3$ with NH_3 and further ammonolysis at CCSD(T).

4.3.5 Equilibrium gas mixture composition

The sequence of considered reactions including 1:1 and 1:2 complex formation and ammonolysis can be summarized as follows:

$$\mathrm{TiCl_{4-x}(NH_2)_x + NH_3 + M} \leftrightarrows \begin{cases} \mathrm{TiCl_{3-x}(NH_2)_{x+1} + HCl + M} & \text{(1 a)} \\ \mathrm{TiCl_{4-x}(NH_2)_x{:}NH_3 + M} & \text{(1 b)} \end{cases} ;$$

$$x=0\text{-}3,$$

$$\mathrm{Ti(NH_2)_4 + NH_3 + M} \leftrightarrows \mathrm{Ti(NH_2)_4{:}NH_3 + M} \qquad \text{(1c)}$$

$$\mathrm{TiCl_{4-x}(NH_2)_x{:}NH_3 + NH_3 + M} \leftrightarrows \begin{cases} \mathrm{TiCl_{3-x}(NH_2)_{x+1}{:}NH_3 + HCl + M} & \text{(2 a)} \\ \mathrm{TiCl_{4-x}(NH_2)_x{:}2NH_3 + M} & \text{(2 b)} \end{cases} ;$$

$$x=0\text{-}3,$$

where M is the carrier gas molecule, which is always present in the CVD reactor. The completely ammonolysed $Ti(NH_2)_4$ molecule can only form 1:1 (reaction (1c)) and 1:2 (reaction (2c)) complexes and does not undergo further ammonolysis.

Energy diagrams corresponding to the above reaction scheme are given in Fig. 4.5,4.7-4.10. Quantum-chemical calculations at CCSD(T) level were used further for the kinetic and thermodynamic calculations. The last scheme is modified by adding one NH_3 molecule to include the 1:2 complex formation of $Ti(NH_2)_4$ (reaction (2c)).

Not all the reactions included in the above scheme are significant in real CVD process. Simple estimate of their role can be obtained considering equilibrium gas composition in typical CVD conditions. Temperature dependencies of the equilibrium concentrations are presented in Fig. 4.11a and Fig. 4.11b for 1:1 and 1:10 $TiCl_4/NH_3$ ratio, respectively. The total pressure in the gas-phase mixture was set to be equal 10 Torr. One of the commonly used inert carrier gases is N_2, which was chosen also in these study. Because of hardware limitations the simplified element-potential method was used to simulate chemical equilibrium in typical conditions during low pressure CVD.

In general, complex formation dominates at the temperatures below 500K . When $TiCl_4$ and NH_3 are mixed in the equal proportion (Fig. 4.11a), both 1:1 and 1:2 complexes of initial molecules are observed. In the excess of additional ammonia (Fig. 4.11b), $TiCl_4$:$2NH_3$ complex dominates. For typical CVD conditions (T=700-1000K) only the product of the first step of ammonolysis, $TiCl_3NH_2$, is observed in substantial concentration, independently on the ratio of reactants. The product of the second step of ammonolysis, $TiCl_2(NH_2)_2$, appears in a noticeable amount only at the temperatures higher than 1000K. As a consequence of high endothermicity of ammonolysis the subsequent products, $TiCl(NH_2)_3$ and $Ti(NH_2)_4$, are practically not observed.

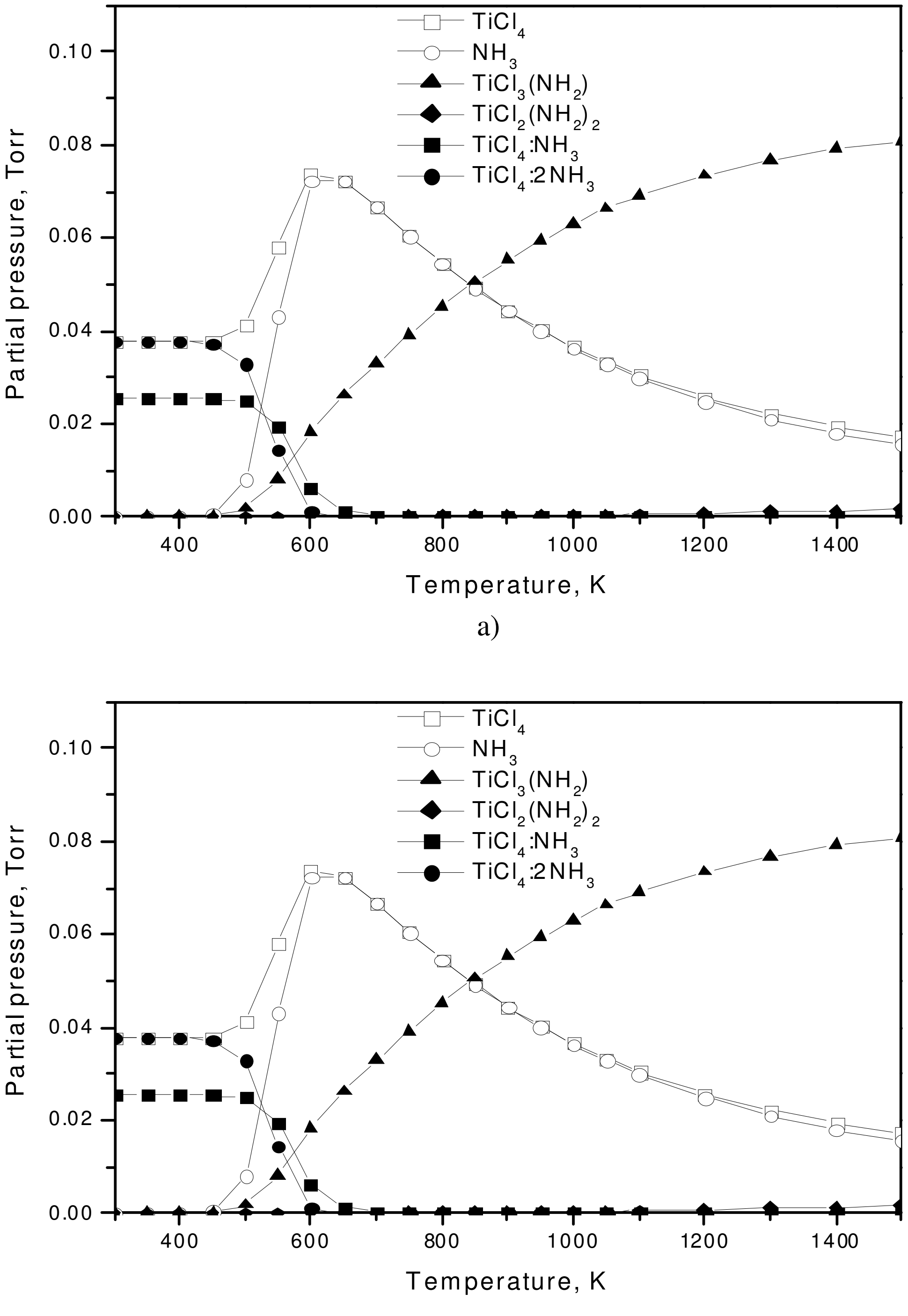

a)

b)

Fig. 4.11. Calculated equilibrium gas-phase mixture composition (Torr) a) Initial gas mixture composition $p(N_2)/p(NH_3)/p(TiCl_4)=0.98/0.01/0.01$. Total pressure $p_{tot}=10$ Torr. b) Initial gas mixture composition $p(N_2)/p(NH_3)/p(TiCl_4)=0.89/0.1/0.01$. Total pressure $p_{tot}=10$ Torr.

4.3.6. Elementary reaction rate constants

The general form of the reaction enthalpy profile ($U_{rp}(q_r)$; q_r is the reaction coordinate) is shown on Fig. 4.12. According to the quantum chemical results presented in this chapter the energy of products can be lower (Fig.4.12a) or higher (Fig. 4.12b) than the energy of the transition state ($C_{+}^{\neq}$). In the latter case the weak H-bonded complexes between reaction products exist, however they have not been considered here since they are too weak to influence significantly the rate of bimolecular reaction.[88] Thus simplified reaction profile shown at Fig. 4.12b by dashed line was used in calculations of the reaction rates.

Reactions with the path profiles shown in Fig. 4.12 proceed via a long-living intermediate complex (C*), which can be stabilized (C) or decomposed to reactants (X + Y) or products (Z +W):

$$\begin{gathered} X + Y \;\underset{k_f(E)}{\overset{k_{dr}(E)}{\leftrightarrows}}\; C^* \;\overset{k_{dp}(E)}{\rightarrow}\; Z + W, \\ C^* + M \;\overset{k_{st}(E)}{\rightarrow}\; C + M. \end{gathered} \qquad (3)$$

Energy dependent rate constants correspond to the following elementary reactions: $k_f(E)$ – C* formation; $k_{dr}(E)$ and $k_{dp}(E)$ – decomposition of C* into reactants and products, respectively; and $k_{st}(E)$ – C* stabilization in collisions with the bath gas molecules M.

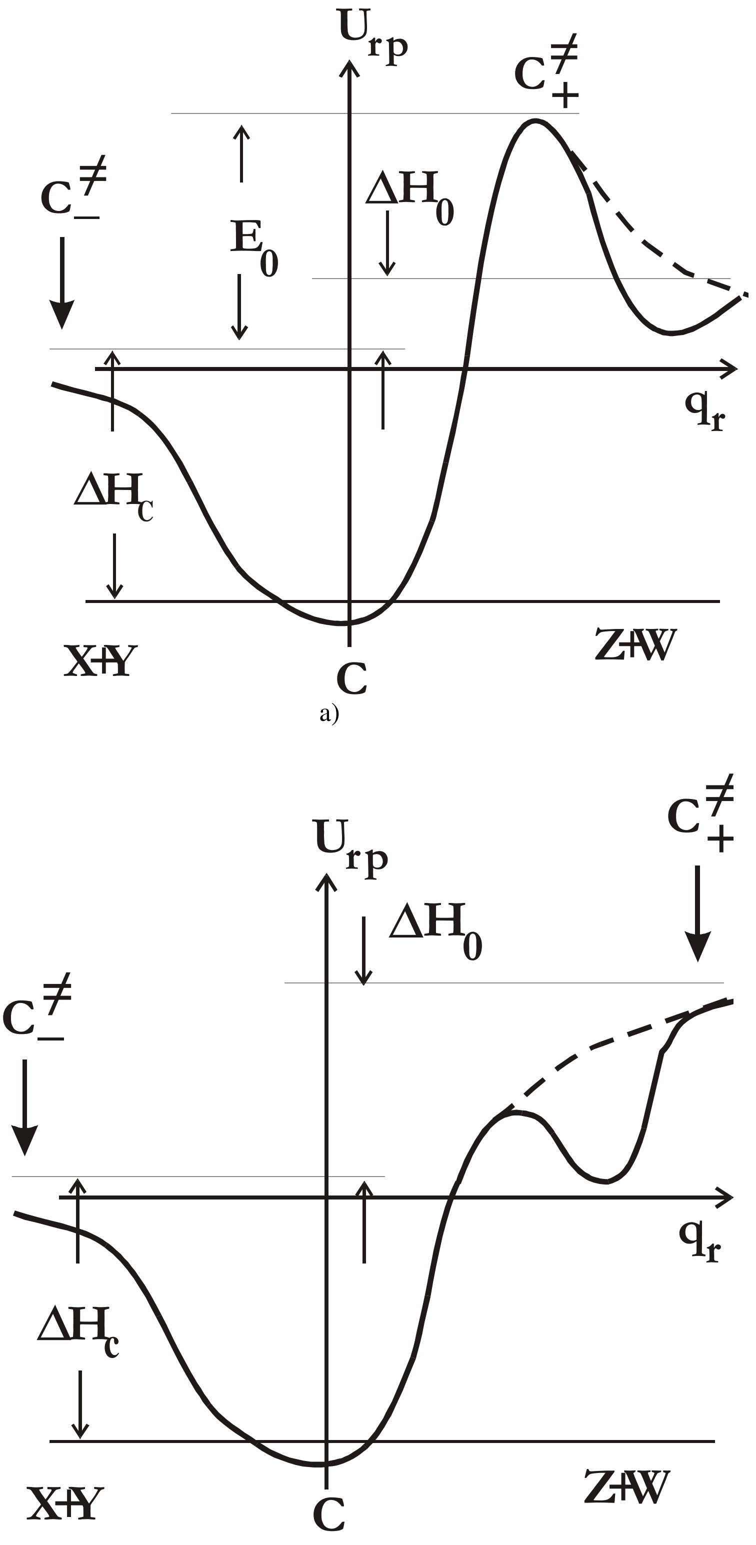

a)

b)

Fig. 4.12. Form of the reaction path profiles of the ammonolysis reactions (**1 a**) - (**2 a**).
a) x=0; b) x=1-3.

The macroscopic temperature dependant rate constants shown on the scheme below are determined by the above mentioned microscopic processes:

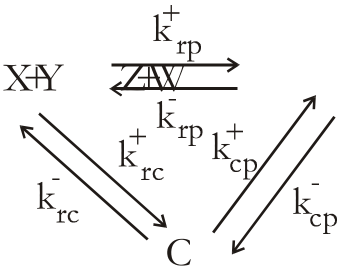

(3)

The model to calculate reaction rates of the formation of considered complexes and their ammonolysis was developed by S. Ya. Umanskii, K. P. Novoselov and A. Kh. Minushev from SOFT-TECH. The consideration starts with the observation that the intermediate complex, C* posses a substantial internal energy above the ground state of the reagents (E(C*) > E_o (ΔH_o ~ 10-18 kcal/mol; see Figs 4.5, 4.7 - 4.10) what results in:

$$k_{dr}(E) >> k_{dp}(E) \qquad (5)$$

Due to the high energy E(C*) also the stabilization of C* in the pressure range used during CVD becomes much less probable than decomposition to reactants:

$$k_{dr}(E) >> [M]\, k_{st}(E). \qquad (4)$$

In such situation the bimolecular rearrangement reaction and the complex formation can be considered independently. For the same reason the direct and reverse reactions between C and reaction products can be excluded from the macroscopic kinetic scheme ($k_{\bullet p}^{+}$ and $k_{cp}^{-} \cong 0$)

The reaction rate constants of direct bimolecular reactions with a well defined potential barrier are evaluated using the standard Transition State Theory. This is valid however only for the first step of ammonolysis. The situation gets complicated when the reaction path profile has no barrier. Direct application of the variational principle is excluded since the information about potential energy surface at large distances is missing. In this case a semi-empirical approach, which was developed for the barrierless association-decomposition reactions at high pressures was considered.[89] The main assumption of this model is that the decomposing complex is represented in the form of two fragments. Interaction between both fragments can be described by Morse potential:

$$U(q_r) = D\{1 - \exp[-\beta(q_r - q_{re})]\}^2, \qquad (7)$$

where D is the classical decomposition energy, q_{re} the equilibrium distance and β is an adjustable parameter (inverse potential energy range), which in these calculations is set to be equal 2. Classical decomposition energy is given as:

$$D = \Delta H_c + \Delta H_0 - \varepsilon_{z,C} + \varepsilon_{z,Z} + \varepsilon_{z,W}, \qquad (8)$$

where ΔH_c and ΔH_0 are the complex formation and bimolecular reaction enthalpies at zero Kelvin temperature (see Fig. 4.5, 4.7-4.10), and $\varepsilon_{z,C}$, $\varepsilon_{z,Z}$ and $\varepsilon_{z,W}$ are zero-point energies of C, Z and W, respectively. The detailed studies of thermodynamic functions based on this assumption result in an approximation to reaction rate constants.[90]

Rate constants of the elementary reactions were calculated in the temperature range 300-1500 K. It appeared that the rate constants of the bimolecular reactions (reactions (1a), (2a)) in this temperature range can be accurately represented in the standard Arrhenius form:

$$k(T) = A\exp\left(-\frac{E_A}{RT}\right). \qquad (9)$$

The values of the pre-exponential factors A^+ for the direct and A^- for the reverse reactions and the corresponding Arrhenius activation energies E_A^+ and E_A^- are given in Table 4.9.

Rate constants of the complex formation and decomposition (reactions 1b,c and 2b,c) depend on the total gas pressure $p_{tot.}$ Calculations performed in the wide pressure range from 6×10^{-2} Torr to 1500 Torr showed that in this range all considered reactions proceed in the low pressure regime or in the beginning of the fall-off regime. Typical fall-off curves are presented in Fig.4.12. It has to be noted that these results justify inequality (6), which allowed to neglect the coupling between the complex formation reactions and bimolecular rearrangement reactions.

Table 4.9 Arrhenius parameters for forward and reverse reactions (A in $cm^3mol^{-1}s^{-1}$, E_A in kcal/mol)

Reaction	A^+	E_A^+	A^-	E_A^-
$TiCl_4 + NH_3 = TiCl_3(NH_2) + HCl$	$1.5849x10^{14}$	22.8	$2.5119x10^{11}$	11.2
$TiCl_4:NH_3 + NH_3 = TiCl_3(NH_2):NH_3 + HCl$	$1.2589x10^{13}$	21.8	$1.9953x10^{11}$	10.7
$TiCl_3(NH_2) + NH_3 = TiCl_2(NH_2)_2 + HCl$	$2.0261x10^{15}$	14.6	$6.1521x10^{14}$	1.1
$TiCl_3(NH_2):NH_3 + NH_3 = TiCl_2(NH_2)_2:NH_3 + HCl$	$1.6692x10^{16}$	18.1	$6.4357x10^{15}$	0.6
$TiCl_2(NH_2)_2 + NH_3 = TiCl(NH_2)_3 + HCl$	$9.0034x10^{14}$	20.2	$2.6668x10^{16}$	0.6
$TiCl_2(NH_2)_2:NH_3 + NH_3 = TiCl(NH_2)_3:NH_3 + HCl$	$7.3862x10^{15}$	25.5	$9.5310x10^{14}$	0.6
$TiCl(NH_2)_3 + NH_3 = Ti(NH_2)_4 + HCl$	$5.3989x10^{15}$	27.0	$6.1521x10^{16}$	1.1
$TiCl(NH_2)_3:NH_3 + NH_3 = Ti(NH_2)_4:NH_3 + HCl$	$5.3711x10^{12}$	27.2	$2.2869x10^{14}$	0.6

The calculated rate constants were used further in kinetic calculations based on the well-mixed reactor model. Calculations were performed at different residence times τ and at the same total pressure p_{tot} and the initial gas compositions at which equilibrium calculations were carried out (see Fig. 4.11).

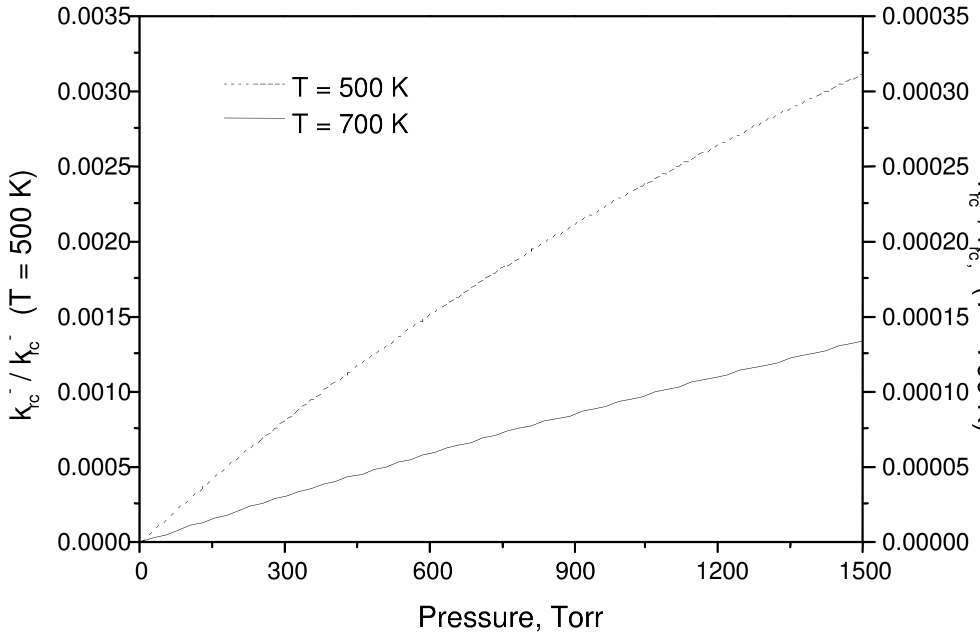

a)

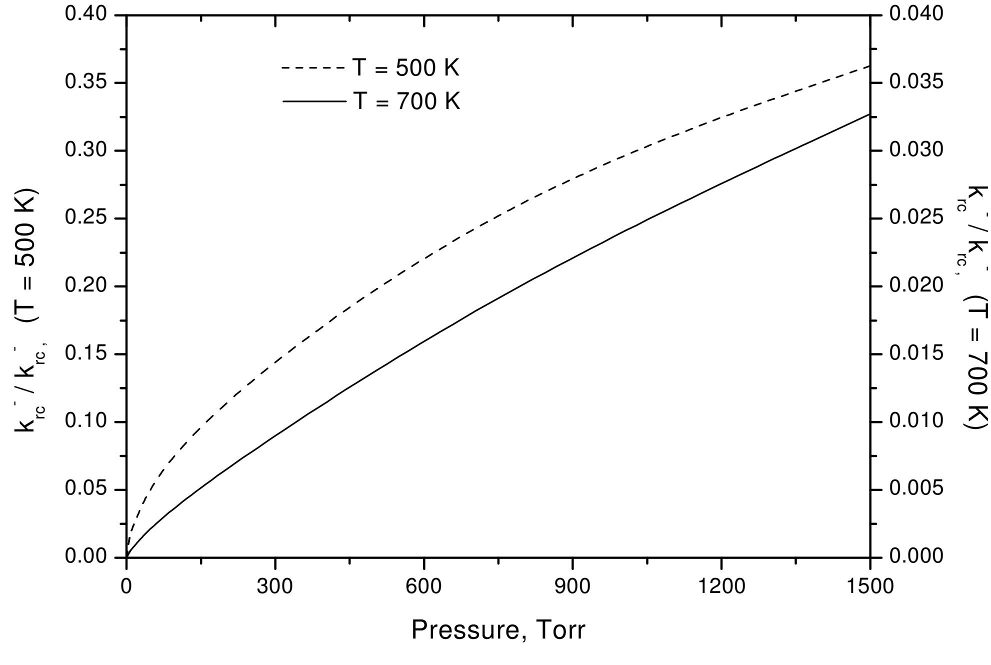

b)

Fig. 4.12. Pressure dependencies of the rates constants for barrierless decomposition reactions at two fixed temperatures: a) $TiCl_4$:NH_3 decomposition; b) $TiCl_4$:$2NH_3$ decomposition.

The most important result of these calculations is, that at temperatures where complex formation or ammonolysis prevail in equilibrium, temperature behavior of the steady-state concentrations of the major products does not differ significantly from the equilibrium one, even at rather small τ. This fact is illustrated at Fig. 4.13 , where steady-state concentrations at different T for τ=1s are presented. The residence time at which steady-state composition becomes close to the equilibrium one becomes large at temperatures close to 600 K (see Fig.4.14) i.e. in this temperature complex formation and ammonolysis proceed with comparable rates

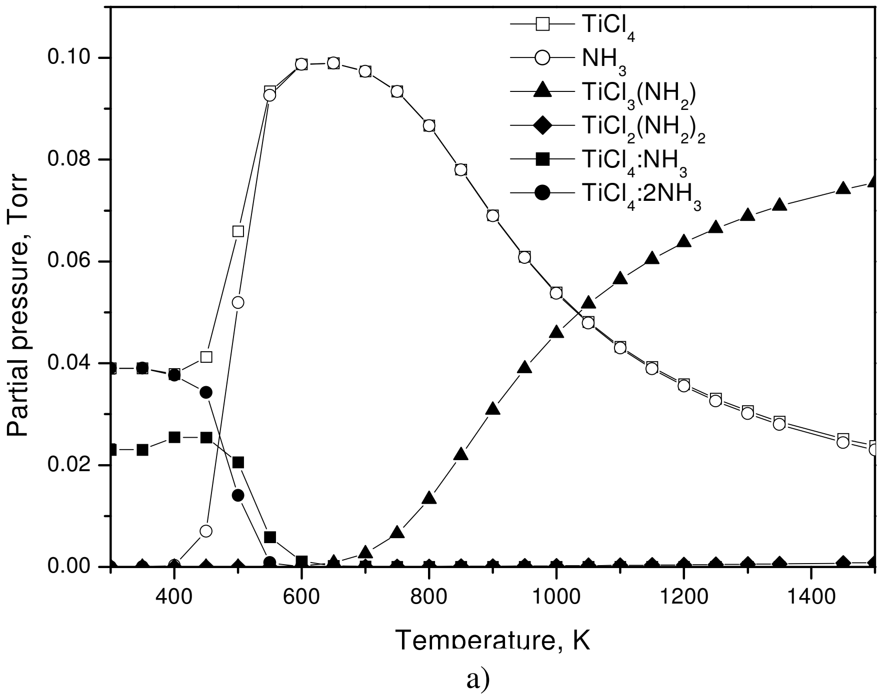

a)

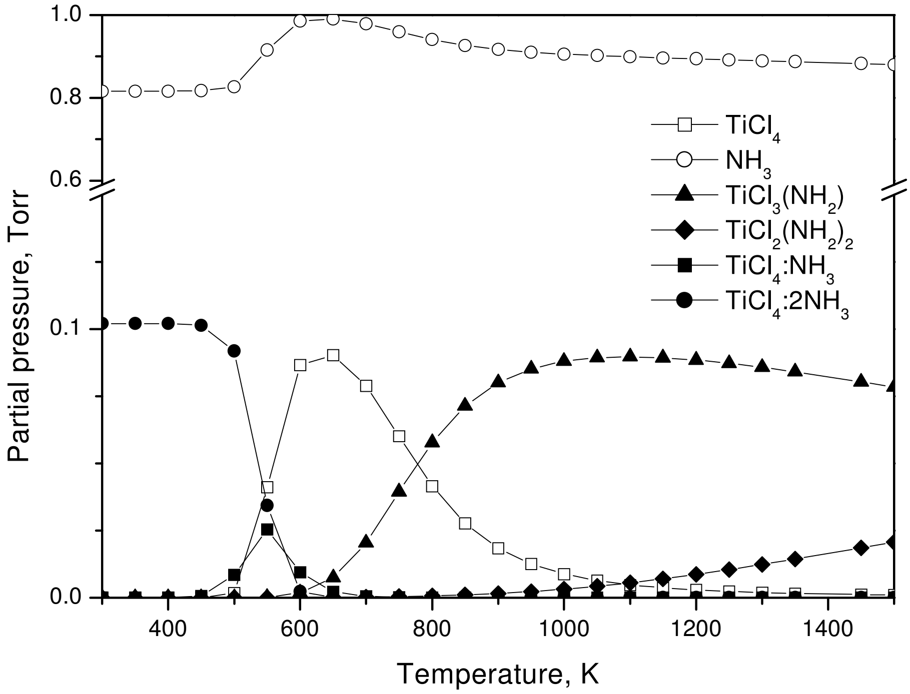

b)

Fig. 4.13. Steady-state concentrations of reactants in a single-wafer reactor with perfect stirring operating at the residence time τ=1s and total pressure p_{tot} =10 Torr. The inflow mixture compositions $N_2/NH_3/TiCl_4$ were taken in proportions: a) 0.98/0.01/0.01, b) 0.98/0.01/0.01.

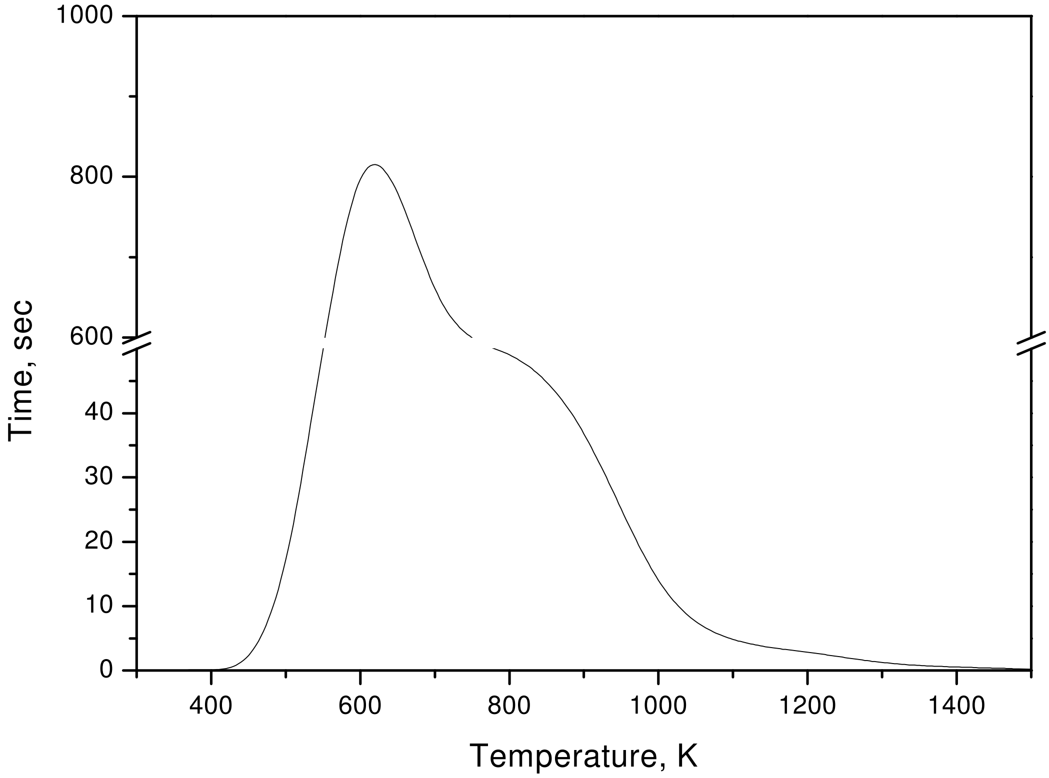

Fig. 4. 14. Temperature dependence of the residence time τ at which steady-state concentrations of the major components in a single-wafer reactor with perfect stirring are close to the equilibrium ones.

4.4 Formation of imido complexes

The formation of a double Ti=N bond during CVD of TiN from $TiCl_4$ and NH_3 undergoes via elimination of HCl from $TiCl_{3-x}(NH2)_x$ (x=0-2) molecules and their five- and six-coordinated complexes with ammonia. The structures of possible $TiCl_{3-x}(NH2)_x$:yNH_3 (x=0-2, y=0-2) complexes were discussed in the first part of this chapter.

4.4.1 Four-coordinated imido compounds

The optimized geometries of $TiCl_2NH$, $TiCl(NH_2)NH$ and $Ti(NH_2)_2NH$ are presented at Fig.4.15. The Ti=N double bond gets elongated together with consecutive substitution of Cl atoms by NH_2 groups, ranging from 1.668Å in Cl_2TiNH to 1.695Å in $(NH_2)_2TiNH$. This is more than 0.2 Å shorter than a single Ti-N bond in the corresponding $TiCl_{3-x}(NH_2)_x$ compounds. Baboul and Schlegel[91] found that the shorter Ti=N bond is additionally about 40 kcal/mol stronger than the single one. The Ti=N-H angle deviates from 180 degree only in case of $Cl(NH_2)TiNH$ where it is equal 169.18°. This is in good agreement with results presented by Schlegel et al.[91] Their calculations at G2 level of theory predict the Ti=N-H angle in $Cl(NH_2)TiNH$ to be 169.9 degree. The Ti=N bond length reported in their work is 1.647Å and 1.676Å for Cl_2TiNH and $(NH_2)_2TiNH$, respectively. Both theoretical results match experimental data for $TiCl_2N'Bu(OPPh_3)_2$ (Ti=N is equal 1.672Å) and $Ti(TMEDA)(Cl)_2$ with Ti=N equal 1.699Å. The almost linear Ti-N-H angle in Cl_2TiNH and $(NH_2)_2TiNH$ does not find an analogue among main groups imido compounds. For example the Si=N-H angle is significantly bent (122 degree) in $H_2Si=NH$. The linear Ti=N-H linkage has been interpreted as a triple bond formulation for linear imido coordination.[92]

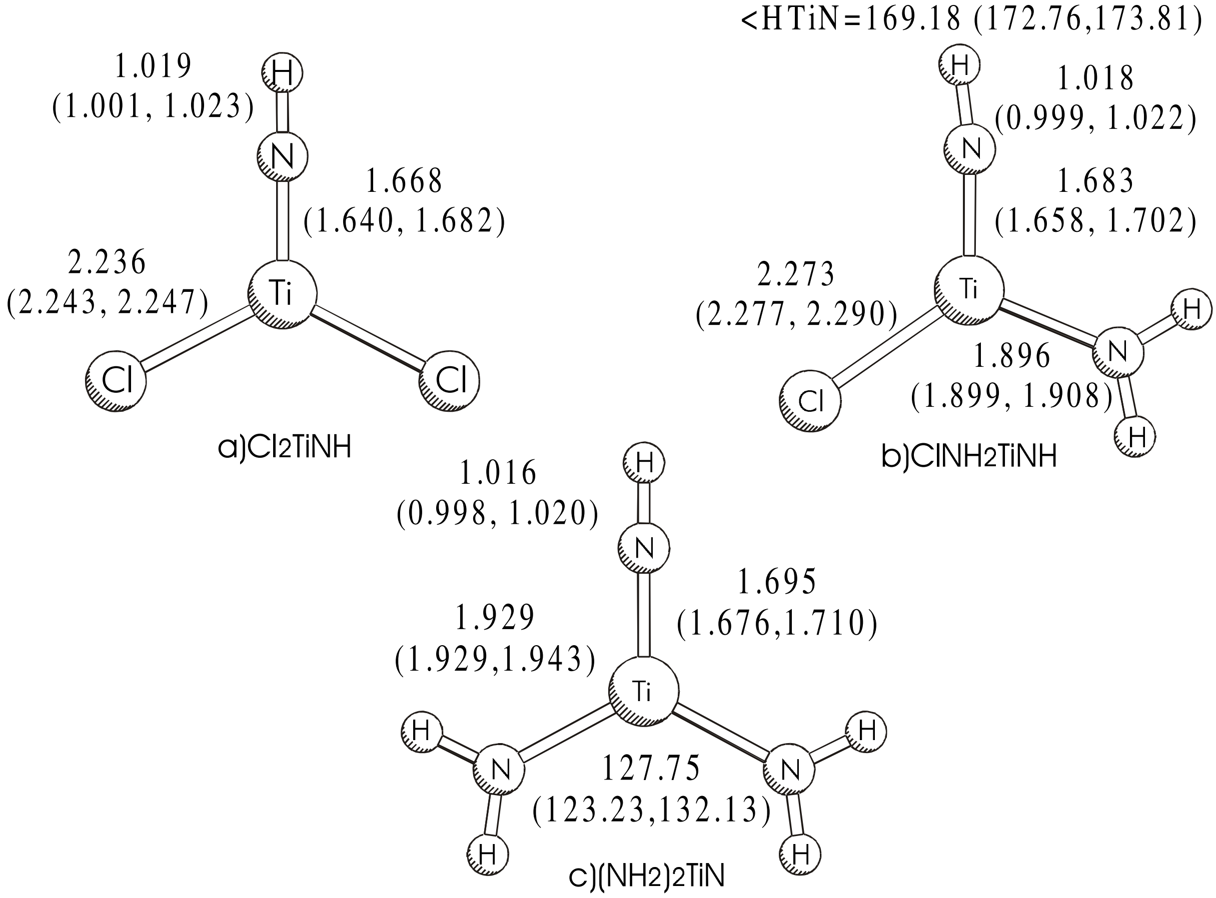

Fig. 4.15 B3LYP optimized geometries of primary imido compounds a) Cl_2TiNH, b) $ClNH_2TINH$, c) $(NH_2)_2TiN$. HF and MP2 values are given in parenthesis.

4.4.2 Five-coordinated imido compounds

Similar to the $TiCl_{4-x}(NH_2)_x$ molecules also primary imido compounds form strongly bonded donor-acceptor complexes with ammonia (Table 4.10). The stabilization energy decreases with increasing number of NH_2 groups ranging at the CCSD(T) level from 47.6 kcal/mol for Cl_2TNH to 35.0 kcal/mol for $(NH_2)_2TiNH$. The last value is in very good agreement with G2 (33.8 kcal/mol) and B3LYP/6-311G(d) (34.3 kcal/mol) results presented by Cross and Schlegel[93] In all cases the MP2 values match CCSD(T) results, while B3LYP data are comparable with HF ones. This binding energy is about twice as strong as it was observed for $TiCl_{4-x}(NH_2)_x$ species (Table 4.2).

Table 4.10 Complex formation energies (ΔH_c) (in kcal/mol) for $Cl_{2-x}(NH_2)_xTiNH:yNH_3$ (x =0-2; y = 1-2) adducts.

$Cl_{2-x}(NH_2)_xTiNH:yNH_3$		HF	**B3LYP**	**MP2**	**CCSD(T)**
Cl_2TiNH	y=1	42.5	44.3	48.1	47.6
	2	69.5	71.7	81.3	80.6
Cl_2NH_2TiNH	1	36.8	38.2	41.2	41.4
	2	55.2	57.8	65.3	65.6
$(NH_2)_2TiNH$	1	30.3	31.7	34.2	35.0
	2	40.0	43.1	49.1	48.5

The analysis of calculated structures (Fig.4.16) shows that the Ti=N distance gets elongated going from $Cl_2TiNH:NH_3$ (1.676 Å) to $(NH_2)_2TiNH:NH_3$ (1.708 Å). All Ti=N values are longer than in the corresponding four coordinated compounds. Also the Ti-Cl and $TiNH_2$ bonds are longer than in $Cl_{2-x}(NH_2)_xTiNH$. According to electrostatic repulsion between ligands the distance between the central Ti atom and coordinated ammonia is the shortest for $Cl_2TiNH:NH_3$ (2.183 Å) and the longest for $(NH_2)_2TiNH:NH_3$ (2.216 Å).

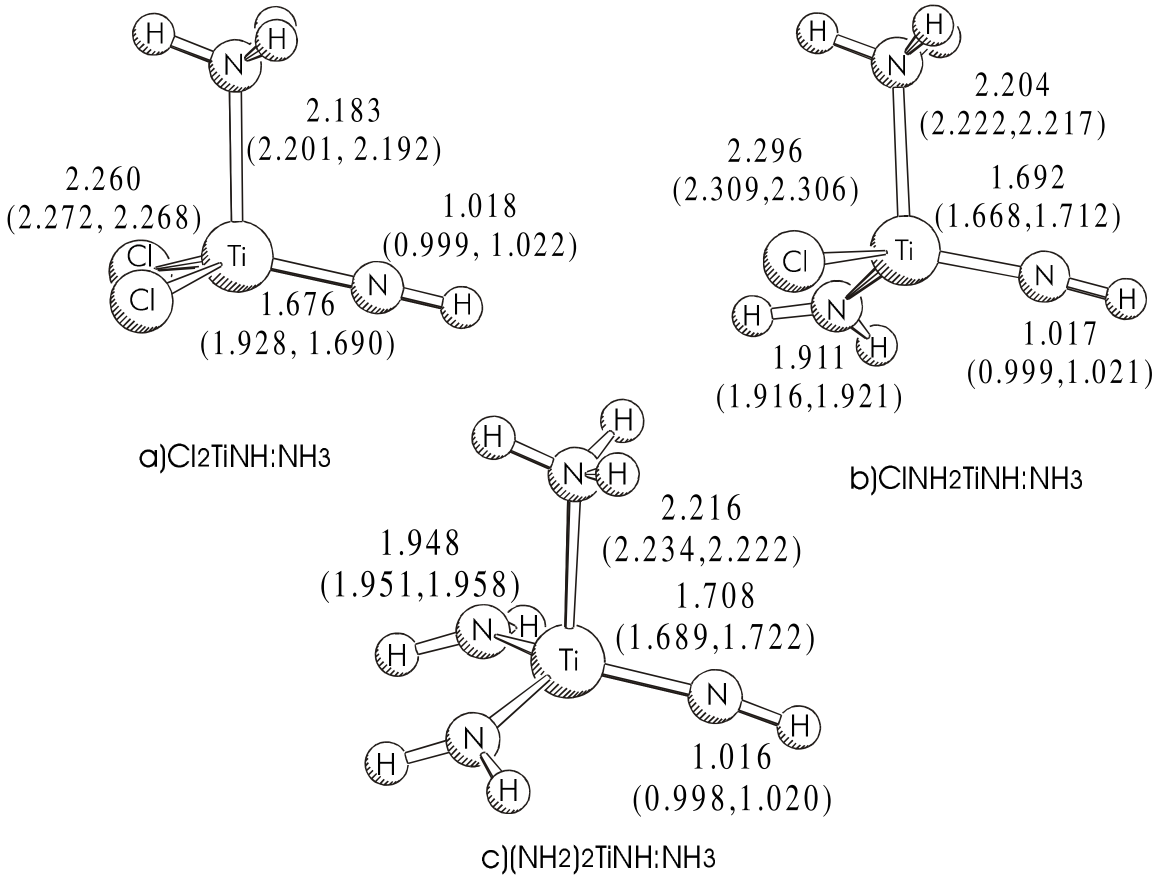

Fig. 4.16 B3LYP optimized geometries of 1:1 imido complexes with ammonia a) $Cl_2TiNH:NH_3$, b) $ClNH_2TINH:NH_3$, c) $(NH_2)_2TiN:NH_3$. HF and MP2 values are given in parenthesis.

4.4.3 Six-coordinated complexes

All imido compounds form moderately strong six-coordinated complexes with the second NH_3 molecule. Similar to six-coordinated amidoes complexes the binding energy of additional NH_3 drops significantly together with increasing number of coordinated amino groups going from 33 kcal/mol for $Cl_2TiNH:2NH_3$ to less than 15 kcal/mol for $(NH_2)TiNH:2NH_3$. This means that in all cases the ΔH_c values of 1:2 complexes are much smaller than the energy of 1:1 aducts (Table 4.10).

The increase of the Ti coordination number by formation of the second dative Ti-NH_3 bond leads to a further elongation of all other bond lenghts in the complexes (Fig.4.17). As it was observed in all amido complexes and four- and five-coordinated imido adducts the Ti=N bond length increases together with increasing number of NH_2 groups in the molecule. Thus the Ti=N distance in $(NH_2)_2TiNH{:}2NH_3$ is about 0.03 Å longer than in $Cl_2TiNH{:}2NH_3$ according to the B3LYP calculations. The MP2 method consequently predicts this bond to be longer, independent on the coordination number of Ti and the number of amino groups in the complex. The large MP2 value of the Ti=N bond length is accompanied with smaller angles between Ti=NH and coplanar ligands compared to HF and B3LYP results.

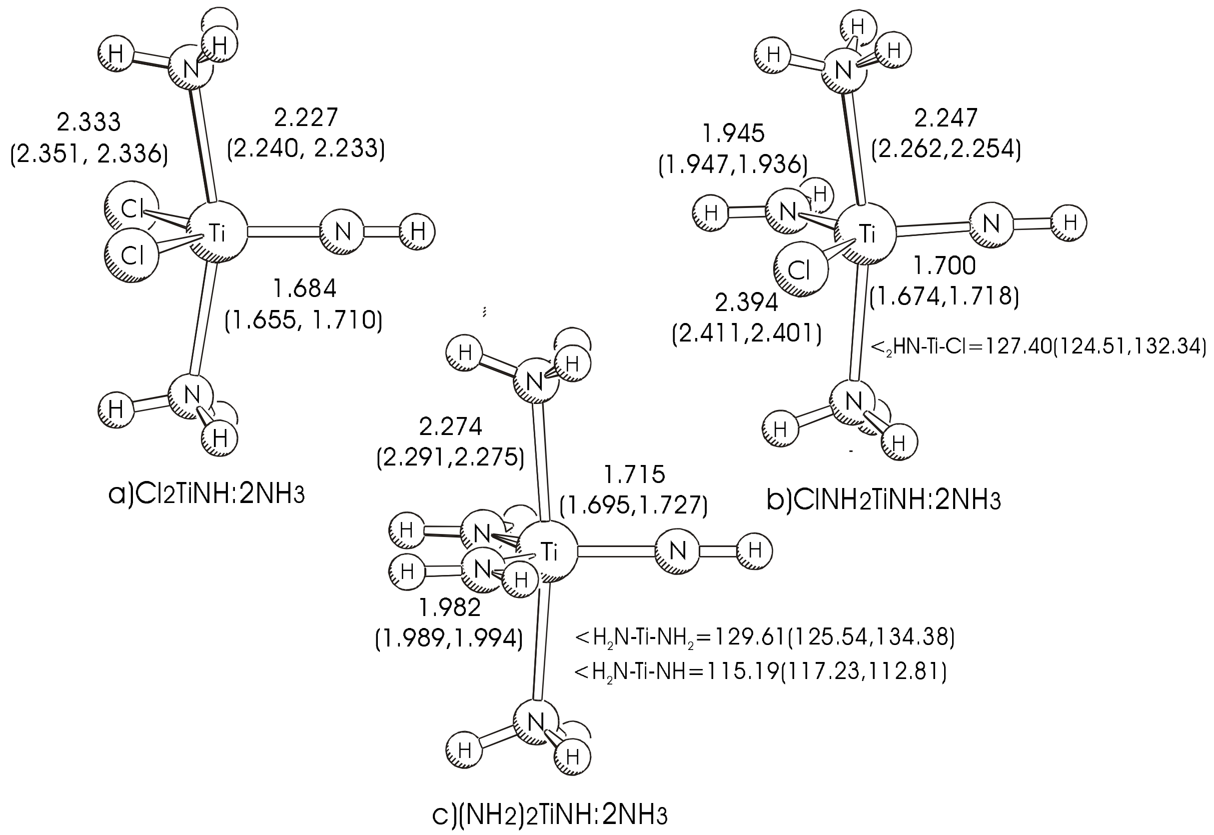

a)Cl2TiNH:2NH3

b)ClNH2TiNH:2NH3

c)(NH2)2TiNH:2NH3

Fig. 4.17 B3LYP optimized geometries of 1:2 imido complexes with ammonia a) $Cl_2TiNH{:}2NH_3$, b) $ClNH_2TINH{:}2NH_3$, c) $(NH_2)_2TiN{:}2NH_3$. HF and MP2 values are given in parenthesis.

4.4.4 Thermochemistry and mechanism of imido species formation

Direct formation of all imido compounds via elimination of HCl from corresponding amidos is rather endothermic and as it was also shown for amino species the heat of reaction increases with the number of NH_2 groups in the molecule (Table 4.11). Coordination of the additional ammonia molecule to amido compounds weakens the Ti-Cl and Ti-NH_2 bonds. Thus the endothermicity of imidoes formation subsequently decreases for five- and six-coordinated complexes. Formation of five- and six-coordinated compounds can be considered also in two steps: exothermic formation of 1:1 or 1:2 amido aducts and endothermic formation of Ti=N bond. The endothermicity of overall formation of five-coordinated imido compounds is in this case significantly reduced. The formation of six-coordinated $Cl_2TiNH:2NH_3$ becomes exothermic (Table 4.12, Fig. 4.18) at all levels of theory. There is no agreement about the sign of the heat of $ClNH_2TiNH:2NH_3$ formation. Understimating of the energy of most of 1:1 and 1:2 imido adducts by HF and B3LYP methods results in higher energy of the overall processes if compared to CCSD(T) (Table 4.12, Fig. 4.19) and MP2. The coordination of a second ammonia to $TiCl(NH_2)_3:NH_3$ lowers the energy of HCl elimination only slightly and the overall reaction stays endothermic (Table 4.12, Fig.4.20).

Table 4.11. Zero Kelvin heats of the subsequent reactions of direct imido $TiCl_{2-x}(NH_2)_xTiNH$ molecules formation and their 1:1 and 1:2 complexes with ammonia (in kcal/mol).

Reaction	**x**	HF	B3LYP	MP2	**CCSD(T)**
$TiCl_3NH_2:xNH_3 \rightarrow Cl_2TiNH:xNH_3 + HCl$	0	65.3	66.9	52.7	61.3
	1	39.8	40.1	28.0	36.9
	2	30.4	28.7	18.4	27.5
$TiCl_2(NH_2)_2:xNH_3 \rightarrow ClNH_2TiNH:xNH_3 + HCl$	0	69.8	67.4	55.5	63.1
	1	46.9	42.8	33.8	41.2
	2	42.6	37.6	30.6	38.1
$TiCl(NH_2)_3:xNH_3 \rightarrow (NH_2)_2TiNH:xNH_3 + HCl$	0	75.3	71.2	62.9	68.9
	1	57.1	50.3	44.8	50.0
	2	55.2	45.7	46.8	49.9

Table 4.12. Zero Kelvin heats of the overall $TiCl_{2-x}(NH_2)_xTiNH$ imidoes formation and their 1:1 and 1:2 complexes with ammonia (in kcal/mol).

Reaction	y	**HF**	**B3LYP**	**MP2**	**CCSD(T)**
$TiCl_3NH_2 + yNH_3 \rightarrow Cl_2TiNH:xNH_3 + HCl$	1	22.7	22.6	4.6	13.7
	2	-4.3	-4.8	-28.5	-19.3
$TiCl_2(NH_2)_2 + yNH_3 \rightarrow ClNH_2TiNH + HCl$	1	33.0	29.2	14.3	21.7
	2	14.7	9.6	-9.7	-2.4
$TiCl(NH_2)_3 + yNH_3 \rightarrow (NH_2)_2TiNH + HCl$	1	45.0	39.4	28.6	33.9
	2	35.3	28.1	13.7	20.3

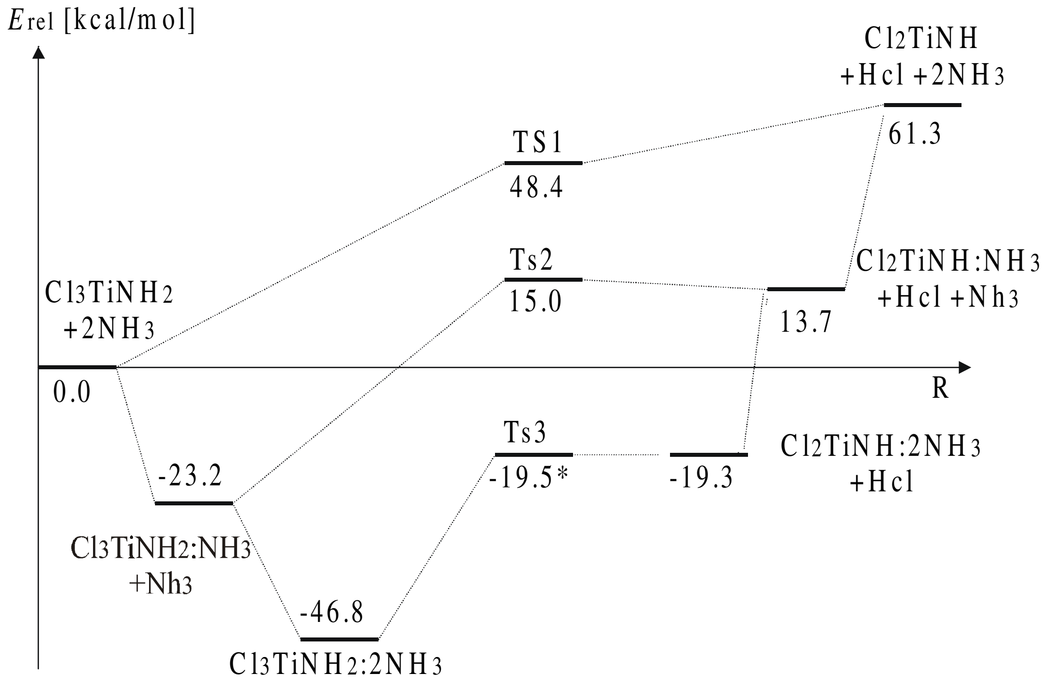

Fig.4.18 CCSD(T) reaction path for formation of 1:1 and 1:2 complexes of Cl_2TiNH with ammonia.

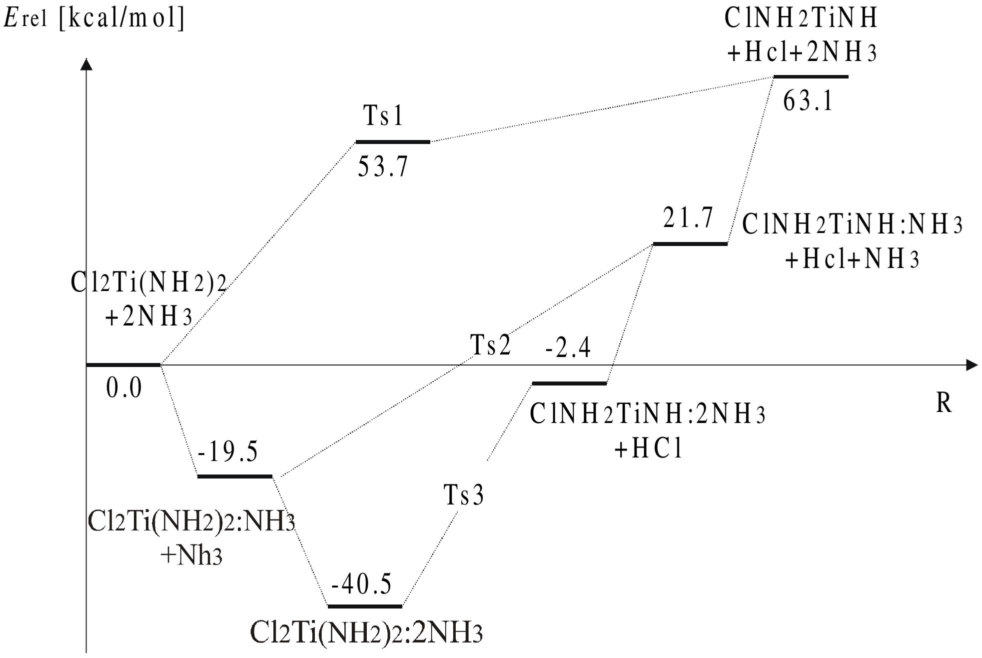

Fig.4.19 CCSD(T) reaction path for formation of 1:1 and 1:2 complexes of $ClNH_2TiNH$ with ammonia.

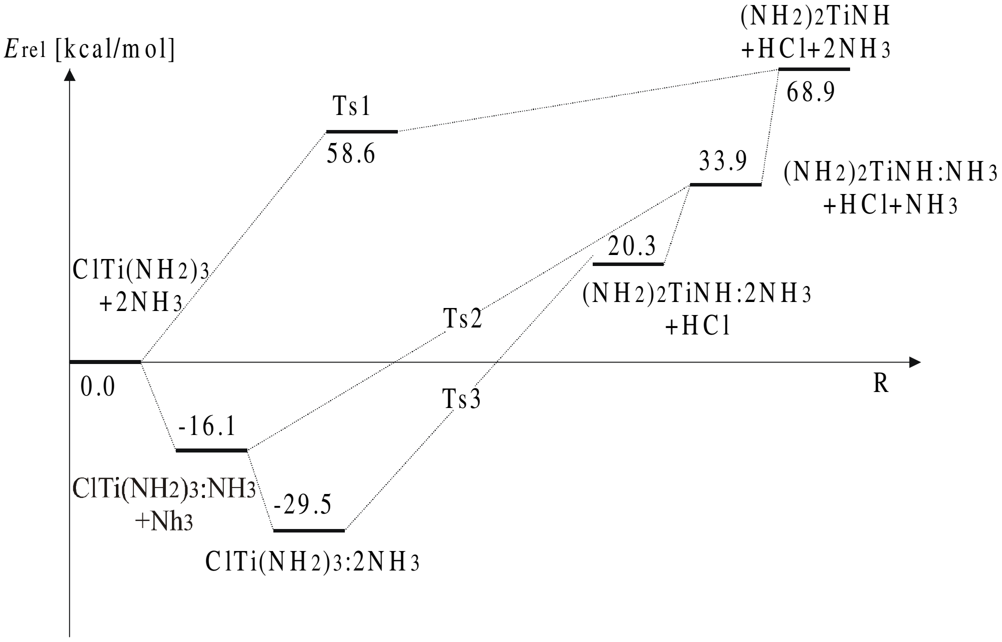

Fig.4.20 CCSD(T) reaction path for formation of 1:1 and 1:2 complexes of $(NH_2)_2TiNH$ with ammonia.

The calculated geometries for elimination of HCl from $TiCl_{3-x}(NH_2)_x$ are presented on Fig.4.21. Table 4.13 shows the corresponding energies of subsequent transition states. The structures located at B3LYP are in all cases closer to the products of the reactions than it is predicted at HF and especially MP2. The additional shift toward reaction products is observed together with substitution of Cl atoms by amido groups.

The reaction barriers increase together with increasing number of amino groups, similar as it was reported for elimination of HCl from $TiCl_{4-x}(NH_2)_x$. The calculated barrier of 48.4 kcal/mol at CCSD(T) level for formation of Cl_2TiNH is in very good agreement with 44.7 kcal/mol reported by Cross and Schlegel.[93] The structure presented in their work is however later along the reaction path (closer to the product), with long distances between Ti and leaving Cl (2.583 Å) and between N and leaving H (2.300 Å). Comparing thermodynamical results for imido compounds (Table 4.11) and TS's (Table 4.13) we see that products of elimination reactions are located above the transition states. Since HCl is a good Lewis acid this indicates the presence of a weak H-bonded complexes of $Cl_{2-x}NH_xTiNH$ with HCl. The strength of this bond appears to be independent on the imido compound and was calculated for $TiClH_2NH_2$ at MP2 level[82] as ~14 kcal/mol. Cross and Schlegel[93] located the $Cl_2TiNH{:}HCl$ adduct 15.6 kcal/mol lower relative to the dissociated products.

Table 4.13. Transition state energies in reactions of substitution of Cl atom by NH_2 group in $Cl_{3-x}(NH_2)_xTiNH{:}yNH_3$ ($x = 0\text{-}2$) molecules (in kcal/mol).

Reaction	y	**HF**	**B3LYP**	**MP2**	**CCSD(T)**
$TiCl_3NH_2{:}yNH_3 \rightarrow Cl_2TiNH{:}yNH_3 + HCl$	0	66.7	53.6	42.7	48.4
	1	52.0	39.9	32.4	38.2
	2	31.8	-	-	27.3
$TiCl_2(NH_2)_2 \rightarrow ClNH_2TiNH + HCl$		68.8		44.0	53.7
$TiCl(NH_2)_3 \rightarrow (NH_2)_2TiNH + HCl$		2.2		9.7	58.6

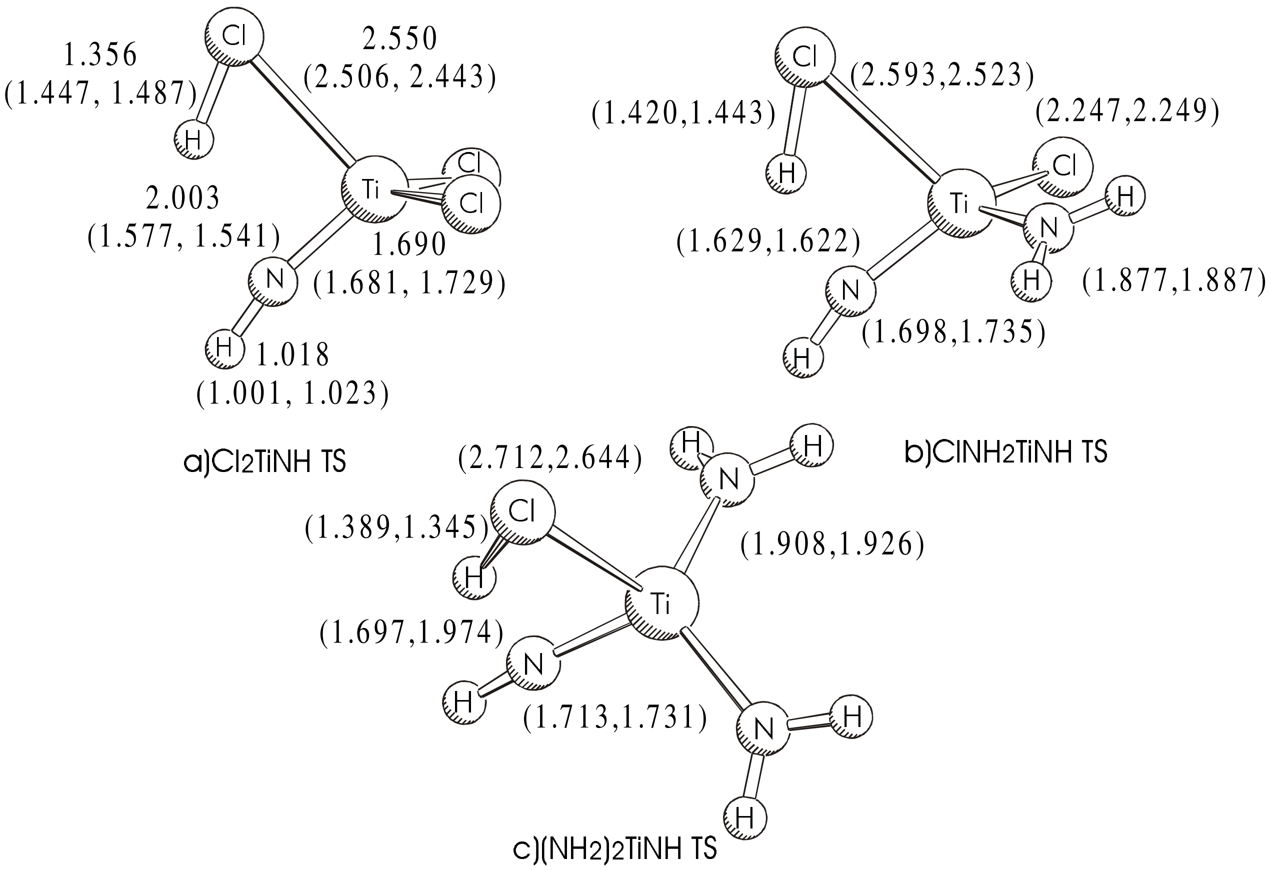

a)Cl2TiNH TS

b)ClNH2TiNH TS

c)(NH2)2TiNH TS

Fig. 4.21 B3LYP optimized geometries of transition states for the formation of imido compounds a) Cl_2TiNH, b) $ClNH_2TINH$, c) $(NH_2)_2TiN$. HF and MP2 values are given in parenthesis.

Transition states for the formation of five- and six-coordinated imido compounds were considered only for $Cl_2TiNH{:}xNH_3$ (Fig.4.22). The calculated structures show that a coordination of ammonia molecules shifts the TS's further toward reaction products. Presence of one ammonia molecule lowers the reaction barrier by more than 10 kcal/mol, compared to elimination of HCl from four-coordinated $TiCl_3NH_2$ (Table 4.13). However as presented in Table 4.11 the $\Delta H_R(0)$ value of the whole reaction drops by more than 25 kcal/mol. This implies that the TS for this reaction is located energetically slighty higher than the dissociated products.

The transition state for elimination of HCl from six-coordinated $TiCl_3NH_2$:2NH3 was located only at the HF level (Fig. 4.22). A CCSD(T) single point calculation performed at the HF optimized geometry gives an energy which is only 0.2 kcal/mol lower than the energy of the dissociated products. This comparision of the results is however not exact since the CCSD(T) energies of both products ($Cl_2TiNH:2NH_3$ and HCl) were calculated at the B3LYP geometries and thus a location of the TS above the reaction products is not excluded.

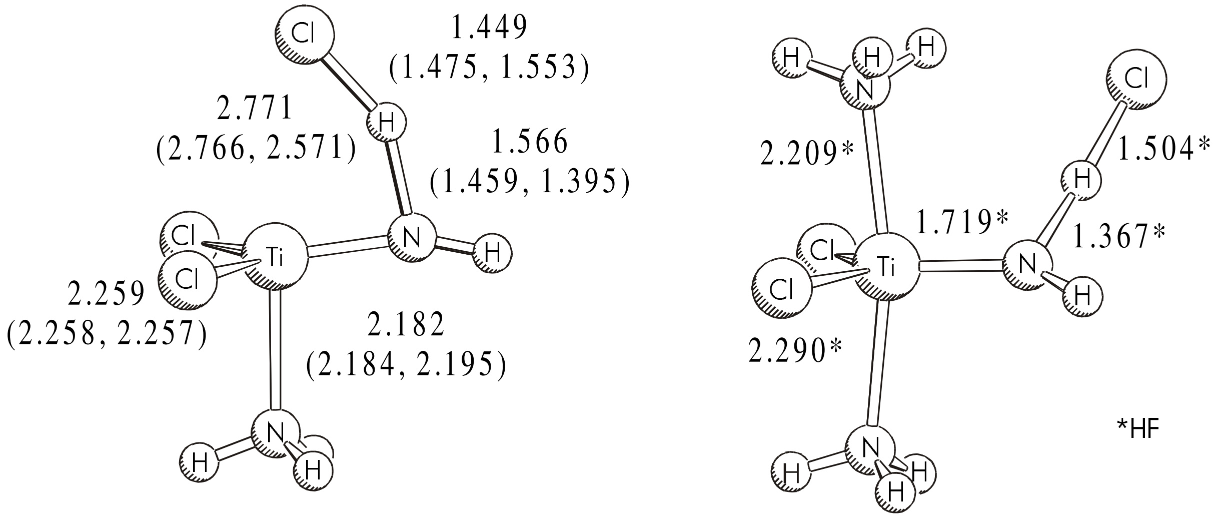

a)Cl2TiNH:NH3TS

b)Cl2TiNH:2NH3TS

Fig. 4.22 B3LYP optimized geometries of transition states in formation of imido complexes a)$Cl_2TiNH:NH_3$, b) $Cl_2TiNH:2NH_3$. HF and MP2 values are given in parenthesis.

4.5 Summary and Conclusions

According to our theoretical studies all four steps of $TiCl_4$ ammonolysis, which occurs in the $TiCl_4/NH_3$ system, are *endothermic* with the heat of reaction increasing along the pathway of the ammonolysis. In excess of ammonia the *exothermic* formation of $TiCl_{4-x}(NH_2)_x$ provides the thermodynamic driving force for ammonolysis. The presented estimation shows that the first three steps of the ammonolysis are exothermic in excess of ammonia, while the last one is endothermic in agreement with the experimental observation of incomplete substitution of Cl atoms by NH_2 groups in gaseous and liquid ammonia.

The transition state structures for substitution of Cl atoms by NH_2 are close to the reaction products. For all but the first step of the ammonolysis the transition states have energies below those of the separated reaction products because of H-bond formation between nitrogen and HCl. The transition state structures "shift" further toward the products with an increasing number of NH_2 groups in the reactant. This complicates their locations on the flat potential energy surface particularly for the correlated methods MP2 and B3LYP. The optimized geometries at B3LYP, HF and MP2 are generally in good agreement with each other. All three correlated methods MP2, B3LYP and CCSD(T) give similar values for the reaction energies, while B3LYP underestimates the complex formation energies compared to the other two methods.

The kinetic and equilibrium analysis of the elementary gas-phase processes illustrates the general behavior of the system in hand at typical CVD conditions. At temperatures below 450 K formation of $TiCl_4{:}yNH_3$ complexes is dominating. If $TiCl_4$ and NH_3 are mixed in equal proportion, both 1:1 and 1:2 complexes of initial molecules are formed. In excess of ammonia, $TiCl_4{:}2NH_3$ complex is the main product at low temperatures. For typical CVD conditions (T=700-1000K) only the first step of ammonolysis product, $TiCl_3NH_2$, is formed in substantial amount. The product of the second step of ammonolysis, $TiCl_2(NH_2)_2$, appears in a noticeable amount only at temperatures higher than 1000K and in case of excess of ammonia.

At medium temperatures (around 600 K) the amount of the first ammonolysis product ($TiCl_3NH_2$) depends essentially on the residence time and increase for long τ.

Direct formation of a Ti=N double bond in all $Cl_{2-x}(NH_2)_xTiNH$ imido compounds is endothermic. The heat of reaction increases with the number of NH_2 groups in the molecule and decreases upon coordination of one and particularly two ammonia molecules. The endothermicity of the direct formation of the five- and six-coordinated imido complexes is significantly reduced when considered with respect to the initial compounds $TiCl_{4-x}(NH_2)_x$ (x=1-3) and yNH_3 (y=1,2). The overall formation of $Cl_2TiNH{:}2NH_3$ and $ClNH_2TiNH{:}2NH_3$ becomes exothermic at MP2 and CCSD(T) levels. B3LYP and HF predict formation of the later species to be slightly endothermic. These reactions offer a low energy pathway for the degradation of titanium complexes in the formation of TiN. The coordination of a second ammonia to $TiCl(NH_2)_3{:}NH_3$ does not significantly reduce the high endothermicity of HCl elimination and this reaction cannot be considered as significant in the CVD of TiN.

The transition states in the formation of $Cl_{2-x}(NH_2)_xTiNH$ are located below the energy of the products. The calculations of the reaction barriers for the formation of five- and six coordinated $Cl_{2-x}(NH_2)_xTiNH{:}yNH_3$ show rather an opposite trend. This indicates that the formation of weak H-bonded complexes between the 1:1 and 1:2 imido aducts and HCl is energetically unfavorable.

References

---

[57] Hoffman, D.M. *Polyhedron,* **1994**, *13,* 1169.

[58] (a) Nicolet, M.-A. *Thin Solid Films,* **1978**, *52,* 415. (b) Wittmer, M.; Studer, B.; Melchior, H. *J. Appl. Phys.,* **1981**, *52,* 5722. (c) Anamori, S. *Thin Solid Films,* **1986**, *136,* 195. (d) Park, K.C.; Kim, K.B., *J. Electrochem.* **1995**, *142,* 3109.

[59] Kurtz, S.R.; Gordon, R.G. *Thin Solid Films,* **1986**, *140,* 277.

[60] Raaijmakers, I.J. *Thin Solid Films,* **1994**, *247,* 85.

[61](a) Dubois, L.H.; Zegarski, B.R. *J. Electrochem.Soc.* **1992**, *139,* 3603. (b) Prybyla, J.A.; Chiang, C.-M.; Dubois, L.H. *J. Electrochem. Soc.* **1993**, *140,* 2695. (c) Weiller, B.H. *J. Am. Chem. Soc.,* **1996**, *118,* 4975.

[62] Musher, J.N.; Gordon, R.G. *J. Electrochem. Soc.* **1996**, *143,* 736.

[63] Lee, J.G.; Choi, J.H.; Lee, C.; Hong, J.H., Lee, E.G. *Jpn. J.Appl. Phys.,* **1998**, *37,* 6942.

[64] (a) Fowles, G.W.A. In *Progress in Inorganic Chemistry. Ed. Cotton, F.A. Vol. 6,* Interscience Publishers, NY 1964, p. 1. (b) Clark, R.J.H. In *Comprehensive Inorganic Chemistry, Vol. 3., Eds, Bailer, J.C.,Jr.; Emeleus, H.J.; Nyholm, R.; Trotman-Dickenson, A.F., 1973, p.355.*

[65] Saeki, Y.; Matsuzaki, R.; Yajima, A.; Akiyama, M. *Bull Chem.. Soc. Jpn,* **1982**, *55*, 3193.

[66] Allendorf, M.D.; Janssen, C.L.; Colvin, M.E.; Melius, C.F.; Niesen, I.M.B.; Osterheld, T.H.; Ho, P. *Electrochem. Soc. Proc. PV95-4,* Pennington, NJ, p. 393.

[67] Baboul, A.G., Schelegel, H.B. *J. Phys. Chem. B*, **1998**, *102*, 5152.

[68] Winter, C.H.; Sheridan, P.H.; Lewkebandra, T.S.; Heeg, M. J.; Proscia, J.W. *J. Am. Chem. Soc*. **1992**, *114*, 1095.

[69] Fix, R.M.; Gordon, R.G.; Hoffman, D.M. *J. Am. Chem. Soc* **1990**, *112*, 7833.

[70] Bergner, A.; Dolg, M.; Kuechle; W., Stoll, H.; Preuss, H. *Mol. Phys.* **1993** ,*80*, 1413.

[71] Huzinaga, S. *Gaussian basis sets for molecular calculations*, Elsevier Amsterdam, Oxford, New York, Tokyo 1984.

[72] Russo, T.V.; Martin, R.L; Hay, P.J. *J. Phys. Chem.* **1995**, *99*, 17085.

---

[73] (a) Ditchfield, R.; Hehre, W.J.; Pople, J.A. *J. Chem. Phys.* **1971**, *54*, 724. (b) Hariharan, P.C.; Pople, J.A. *Theor. Chim. Acta* **1973**, *28*, 213. (c) Francl, M.M.; Pietro, W.J.; Hehre, W.J.; Binkley, J.S.; Gordon, M.S.; DeFrees, D.J.; Pople, J.A. *J. Chem. Phys.* **1982**, *77*, 3654.

[74] R. J. Kee, F. M. Rupley, J. A. Miller, M. E. Coltrin, J. F. Grcar, E. Meeks, H. K. Moffat, A. E. Lutz, G. Dixon-Lewis, M. D. Smooke, J. Warnatz, G. H. Evans, R. S. Larson, R. E. Mitchell, L. R. Petzold, W. C. Reynolds, M. Caracotsios, W. E. Stewart, and P. Glarborg, Chemkin Collection, Release 3.5, Reaction Design, Inc., San Diego, CA (1999).

[75] Cotton, F.A.; Wilkinson, G. *Advanced Inorganic Chemistry. Fourth Edition.* Wiley: NY, 1980, p. 700.

[76] Fowles, G.W.A.; Pollard, F.H. *J. Chem. Soc.* **1953**, *527*, 2588.

[77] Kurtz, S.R; Gordon, R.G.; Thin Solid Films, **1986**, *140*, 277.

[78] Morino, Y.; Uehara, H. *J. Chem.Phys*, **1966**, *45*, 4543.

[79] Jonas, V.; Frenking, G., Reetz, M.T., *J. Comp. Chem.* **1992**, *13*, 919.

[80] Krömer, R.; Thiel, W. *Chem. Phys. Lett.* **1992**, *189*, 105.

[81] Sosa, C.; Andzelm, J.; Elkin, B.C.; Wimmer, E.; Dobbs, K.D.; Dixon, .D.A., *J. Phys. Chem.* **1992**, *96*, 6630.

[82] Cundari, T.R.; Gordon, M.S. *J. Am. Chem.Soc.***1993**, *115*, 4210.

[83] Haaland, A.; Rypdal, K.; Volden, H.V.; Andersen, R.A. *J.Am. Chem. Soc.,Dalton Trans.* **1992**, 891.

[84] Lappert, M.F.; Power, P.P.; Sangerand, A.R.; Srivasta, R.C., Metal and Metalloid Amides; Ellis Horwood: Chichester, 1980, p 475.

[85] Beste, A.; Krämer, O.; Fischer, A.; Frenking, G. *Eur. J. Inorg. Chem.* **1999,** 2037-2045.

[86] Wells, A.F.,Structural Inorganic Chemistry, Clarendon Press, Oxford, 1975.

[87] (a) Szczesniak, M.M.; Kurnig, I.J.; Scheiner, S. *J. Chem. Phys.***,** **1988**, *89*, 3131. (b) Del Bene, J.E. *J. Comput. Chem.* **1989**, *10,* 603. (c) Chiport, C.; Rinaldi, D.; Rivail, J.-L. *Chem. Phys. Lett.* **1992**, *191,* 287.

---

[88] Holbrook, K.A., Pilling, M.J. and Robinson, P.J. *Unimolecular Reactions*, London: Wiley-Interscience, 1972.

[89] Quack, M. and Troe, J. *Ber. Buns. Phys. Chem.* **1977**, *81*, 329

[90] Umanskii, S.Ya.; Novoselov, K.P.; Minushev, A.Kh.; Siodmiak, M.; Frenking, G.; Korkin, A.A.

[91] Baboul, A.G, Schlegel, B. *J. Phys. Chem. B* **1998**, *102*, 5152.

[92] Nugent, W.A., Mayer, J.M. Metal-Ligand Mulitple Bonds, Wiley, New York, 1988.

[93] Cross, J.B. and Schlegel, H.B. , private communication, submitted to press

5. Hydrogen adsorption at TiN (100) surface

5.1. Introduction

Knowledge and understanding of chemical mechanism of reactions at solid surfaces are of great importance to chemisorption.[94] *Ab initio* calculations of chemical reactivity at solids, which could provide a microscopic description of surface processes, are however still far from achieving the accuracy obtained in the molecular study. Metal surfaces are particularly difficult for computational studies due to the large number of low-lying excited states. Thus only the interaction of small molecules with metals can be studied in more detail. Particular attention was directed so far toward hydrogen atom and H_2 molecule with dissociative adsorption on metal surfaces.

This chapter presents a density functional study of hydrogen atom adsorption on the TiN surface. Atomic hydrogen appears during CVD of TiN as a byproduct of NH_3 adsorption at the surface. Additionally, if H_2 is used as a carrier gas, hydrogen atoms enter the system in process of dissociative adsorption of H_2 at the surface. The presented calculations start with finding the parameters of the TiN bulk and defining an adequate model of the TiN surface, taking into account the properties of solid TiN. Similar to other refractory-metals TiN crystallizes in the NaCl structure, which is typical for ionic crystals. On the other hand high melting point and extreme hardness of TiN resemble properties which are found for covalent compounds. Additionally, TiN shows metallic conductivity and luster and low temperature superconductivity. Thus chemical bonding in the solid state combines ionic, covalent and metallic contribution. Ionic character of the bond is confirmed by clear charge transfer from the metal to the nonmetal. Covalent binding becomes evident due to interaction between the nonmetal and the metal orbitals

(pd_σ and pd_π). Metallic contribution (dd_σ) occurs since metal-metal distance in TiN crystal is about the same as in the pure Ti metal.

In addition to the solid state calculations the $(TiNHCl)_2$ cluster was investigated as a simplified molecular model of TiN surface. The calculations were performed using the same density functional and basis sets in both approaches, which allows qualitative and quantitative comparison of the obtained results.

5.2 Computational methods

Local Density Approximation PWC[95] and non-local PW91[96] density functionals were used for calculations of the lattice constant and the bulk modulus of TiN. The PW91 functional provided results in better agreement with experiment and thus was chosen for further studies of hydrogen interaction with the TiN surface. The same functional was applied also in the molecular study. In both periodic solid state and molecular calculations the inner core electrons of Ti were described by a 10MDF ECP[97]. Valence electrons were described by a double numerical DNP basis set, which consists of two functions for each occupied orbital in the free atom, supplemented with a d-type polarization function[98]. Solid state test calculations were performed using basis functions restricted within a radius of 4.5 Å and 4.0 Å. No qualitative and quantitative difference in the computed lattice constant and energy per atom was observed. Thus the computationally less expensive option of basis set restricted within 4.0 Å cut-off radius was chosen for the whole series of calculations. In the solid state calculation Bloch functions have been expanded as a linear combinations of atomic basis functions and the corresponding matrices have been evaluated by numerical integration. The Monkhorst-Pack algorithm has been applied for accurate Brillouin-zone integration with automatic generation of the 7×7×1 irreducible k-point grid.

5.3 TiN properties

5.3.1 TiN bulk properties

Even at the early stages of crystal growth TiN crystallizes in the fcc NaCl lattice structure[99] with the lattice constant of 4.238 Å[100]. In this work crystal parameters for TiN bulk (lattice constant *a* and bulk modulus *B*) were calculated using both the local density functional PWC[95] and the non-local PW91[96] functional. The minimum energy lattice constant *a* was found by approximation of the potential energy surface determined by single point energy calculations for bulks of different lattice constants (Fig. 5.1). The bulk modulus *B* has been obtained by computation of the second derivative of the potential energy with respect to the unit cell volume using the following expression:

$$B = V\frac{\partial^2 U_0}{\partial V^2}$$

where V is a volume of the unit cell and U_0 is the internal energy at 0K.

The lattice constant *a* of 4.47 Å computed using the LDA PWC functional is overestimated compared to the experimental value 4.238 Å[100] (Table 5.1). However the bulk modulus B=282.8 GPa calculated using this approach is in reasonable agreement with 288 GPa[102] taken from the experiment. The non-local density functional PW91 gives a lattice constant 4.25 Å, which is very close to the experimental value. It is also in good agreement with *a*=4.236 Å obtained using the plane wave approach together with the same PW91 non-local density functional.[103] The calculated bulk modulus of 278 GPa at PW91 level deviates from the experimental value slightly more than that provided by PWC functional. The method of estimating the bulk modulus, which was applied in this work serves however only as an approximation. Since the lattice constant is more essential in the further consideration of the interaction between the surface and the gas phase species, the non-local PW91 functional is found to be better suited and together with the lattice constant of 4.25 Å was chosen for further calculations.

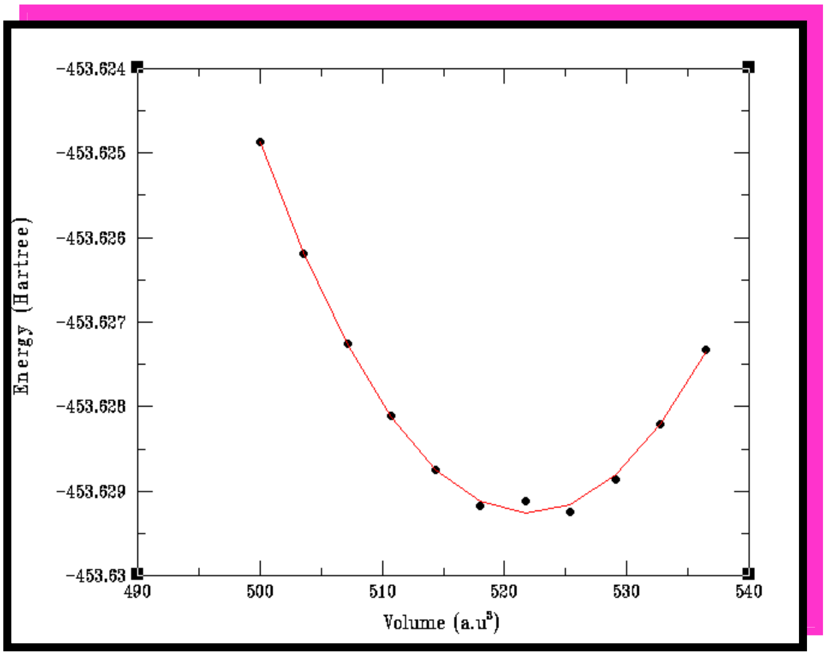

Fig. 5.1 Bulk energy as a function of unit cell volume.

Table 5.1 TiN bulk parameters: lattice constant *a* and bulk modulus *B*

	PWC	**PW91**	**Exp.**
a [Å]	4.47	4.25	4.24
B (GPa)	283	278	288

5.3.2 TiN surface

Having optimized the lattice constant the studies of three classes (Fig. 5.2) of TiN surfaces: (100), (110) and (111) were performed.. The standard method for calculating the surface energy is to subtract the bulk energy from the total energy of a slab containing the same number of atoms. The multiplication by factor 1/2 gives a single surface energy. According to the calculations of the surface energy for static (unrelaxed) slab, the (100) surface has the lowest energy (Table 5.2). The (110) surface energy is about twice as large and the (111) surface is energetically located more than three times higher than the (100) surface. These results are in good agreement with energies reported by Marlo and Milman[103] (Table 5.2). Using the plane wave approach they calculated both static and relaxed surfaces. Static surface energies are very close to those calculated in this work. Surface relaxation systematically lowers the energy by 0.28-0.5 J/m^2, however it does not change the energetical sequence of the TiN surfaces. The experimental estimates of the TiN surface energies based on sublimation energies yielded much higher values of 4.94, 6.99 and 8.53 J/m^2 for (100), (110) and (111) surfaces, respectively.[104] There is however qualitative agreement that the (100) surface in energetically the most favorable.

Table 5.2 Calculated and experimental surface energies (J/m^2) for TiN surfaces.

Surface	**PW91**	**PWA-PW91, static**$^{1)}$	**PWA-PW91, relaxed**$^{1)}$	Experiment$^{2)}$
(100)	1.74	1.76	1.30	4.94
(110)	3.29	3.14	2.86	6.99
(111)	5.30	5.45	4.95	8.53

$^{1)}$see ref. 103
$^{2)}$ see ref. 104

Since the energy differences going from (100) to (111) surfaces are quite significant, it is justified to consider only the (100) surface in further calculations of the surface phenomena. In order to study the details of these processes the TiN surface must be approximated by a suitable slab, which resembles both surface and bulk properties. Searching for an optimal model of the (100) TiN surface four unit cells containing 16, 20, 24 and 28 atoms were calculated. The unit cells correspond to slabs with 4, 5, 6, and 7 layers, respectively. Since calculations are performed within the periodic approach a 21 Å width of vacuum had to be added to each slab to keep the surface far from interaction with the other slabs. In the optimization of all unit cells the last layer was kept frozen to simulate the TiN bulk. It is reasonable to assume that an optimal model of the unit cell should contain at least two more layers, which possess properties of the TiN bulk and are not influenced by surface relaxation. For this purpose two parameters were calculated:

T- plane width - defined for a plane that contains both Ti and N as a distance between the subplanes occupied by Ti and N atoms.

D - distance between the average positions of TiN planes parallel to the surface.

The model with 7 layers provides the most reliable information since at least two central layers are free from any constrains imposed by the last frozen one. As it is presented in Table 5.3 the **T** parameter for the 3rd and 4th layer approaches zero, which indicates that both Ti and N are almost in the same plane. The plane width **T** of the outermost layer is about 0.17 Å with N atoms going further outside the surface than the Ti sublayer. The parameter **D** converges for the central layers to the bulk value and is calculated to be exactly 2.125 Å for the last two layers (Table 5.4). These results suggest that a slab containing five layers is already a reasonable model to describe the TiN (100) surface. In order to simulate the bulk effect in such slab the last two layers will be kept frozen at the positions like in the TiN crystal.

Table 5.3 T parameter for slab of 7 layers:

No. of layer	T
1 (outermost)	0.174
2	0.027
3	0.039
4	0.009
5	0.017
6	0.084
7	0.0

Table 5.4 D parameter for slab of 7 layers:

No. of layers	D
1 - 2	2.089
2 - 3	2.107
3 - 4	2.123
4 - 5	2.109
5 - 6	2.126
6 - 7	2.125

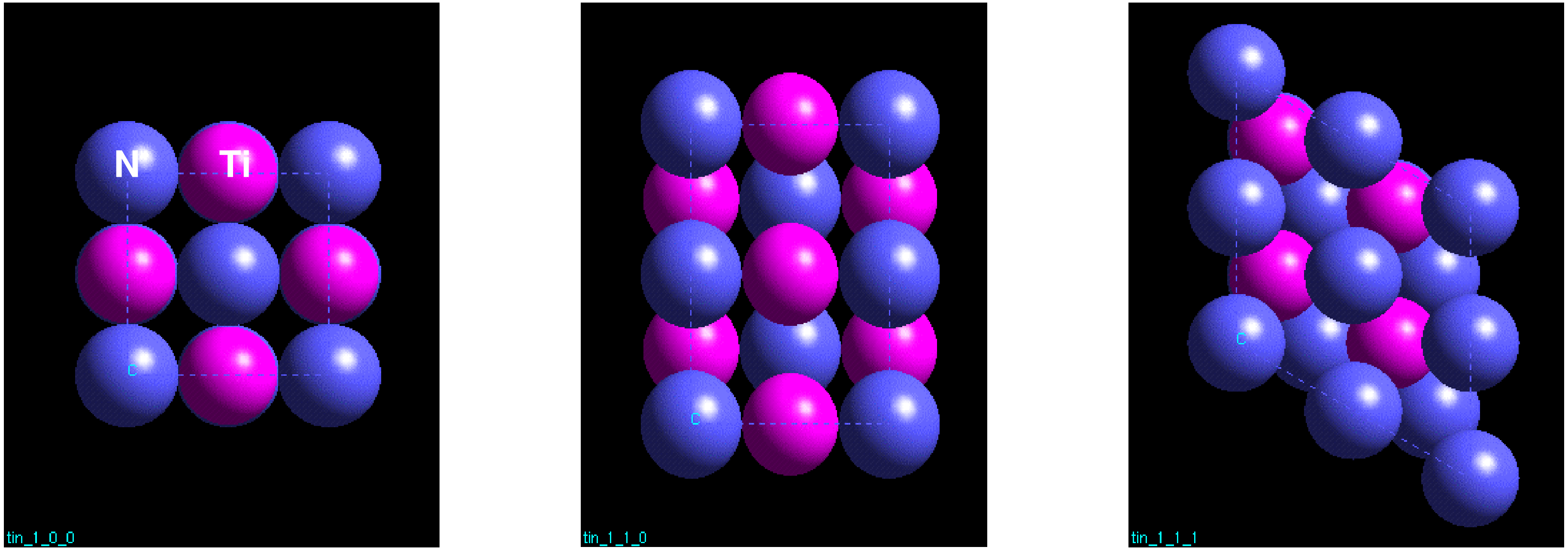

a) (100) surface

b) (110) surface

c) (111) surface

Fig. 5.2 Three classes of the TiN surface: a)(100) surface, b) (110) surface, c) (111) surface.

5.4 Hydrogen atom adsorption on TiN (100) surface

5.4.1 Molecular (cluster) model

The four-membered cyclic molecule, $(ClTiNH)_2$, has been selected in this work as a simplified molecular (cluster) model to study hydrogen interaction with the TiN(100) surface. This model is structurally and electronically close to the $(TiN)_2$ element on the surface. Since hydrogen is more electropositive than nitrogen, and chlorine is more electronegative than titanium, both atoms were chosen to saturate the dangling bonds at nitrogen and at titanium respectively. This assures charge partitioning on both Ti and N which reassembles those in the TiN crystal with nitrogen being negatively and titanium being positively charged (Table 5.5). $(ClTiNH)_2$ cluster relates also to $TiCl_4$ and NH_3, the precursors in titanium nitride deposition.

Table 5.5 Charge distribution on Ti and N atoms in $(TiClNH)_2$ and TiN bulk.

atom	**$(TiClNH)_2$**	**TiN bulk**
Ti	0.743	0.775
N	-0.628	-0.775

The PW91 functional locates a triplet state of $(TiNHCl)_2$ 3 kcal/mol lower than the lowest singlet state (Fig. 5.3, Fig. 5.5). The singlet state favors the conformer with *cis* orientation of both Cl atoms and N atoms. The molecule in the triplet state is planar with a distance between both Ti's being 0.4 Å longer than in the singlet state (Fig. 5.3a). This suggests that electrostatic repulsion of the positively charged Ti atoms dominates over the exothermic[105] formation of the metal-metal bond. Since the coordination number of both

Ti and N is lower than in solid TiN, the Ti-N bond calculated in the molecular cluster is shorter than in the bulk by about 0.2 Å.

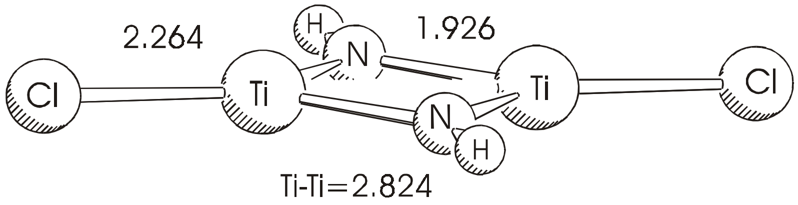

a) triplet

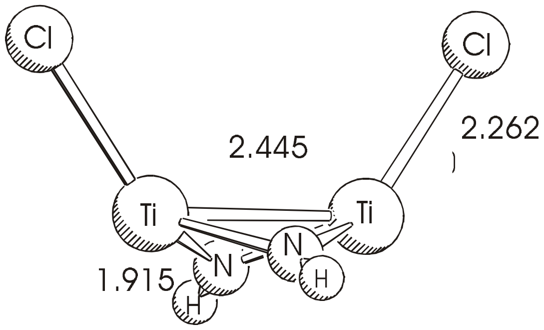

b) singlet

Fig.5.3 PW91 calculated geometries of $(TiClNH)_2$ a)triplet state, b) singlet state

The hydrogen atom can be directly adsorbed either at the Ti or at N atom. PW91 predicts stronger binding for hydrogen adsorbed at the Ti site (Fig. 5.4a, Table 5.6) with the value of 56.1 kcal/mol and corresponding bond length of 1.7 Å. Adsorption at nitrogen leads to the bond formation of a length comparable with the N-H bond in $(TiClNH)_2$ (Fig. 5.4b) and a strength of 45.5 kcal/mol (Fig. 5.5). At the crystal surface there are still two other possibilities of single atom adosrption – at the hollow and along the Ti-N bond. The molecular counterpart of the hollow location is presented at Fig. 5.4c, with the hydrogen atom in the middle of the Ti-Ti and N-N distances. Fig. 5.4d shows the hydrogen atom located along the Ti-N bond in $(TiClNH)_2$.

The structure with H between both Ti's sites is located 14 kcal/mol higher than the $(TiClNH)_2$ with the hydrogen bonded to Ti (Table 5.6). The Ti-H bond is elongated to 1.967 Å and is accompanied by a shorter distance between the Ti atoms which is 2.456 Å. This suggests that the increase of electrostatic repulsion between the metal atoms is responsible for the decrease of the adsorption energy.

The molecular model for the hydrogen location above the Ti-N bond was assigned as a transition state and is energetically least favorable, with an energy of only 8.6 kcal/mol lower than separated $(TiClNH)_2$ and H atom (Table 5.6, Fig. 5.5). The calculated distances Ti-H=1.786 Å and N-H=1.360 Å show that this structure is closer to the global minimum than to $(TiClNH)_2$ with the hydrogen bonded to N. This suggests that the system with H above the Ti-N bond is a late transition state in the migration of hydrogen from the less favorable nitrogen site to the titanium site. The PW91 barrier for this migration is 36.9 kcal/mol.

Adsorption of two hydrogen atoms was considered as a model of so-called high coverage adsorption, when due to the high concentration of the gaseous species more than one binding site per unit surface is active during the process. Two hydrogen atoms can be adsorbed at $(TiClNH)_2$ cluster at both Ti sites, Ti and N, and both N atoms.

Table 5.6 Calculated bond lengths and adsorption energies for hydrogen at $(TiClNH)_2$.

H location	**r [Å]**	**E [kcal/mol]**
above Ti	1.700	56.1
above N	1.025	45.5
above hollow	1.536	42.1
above Ti-N bond	0.620	8.6

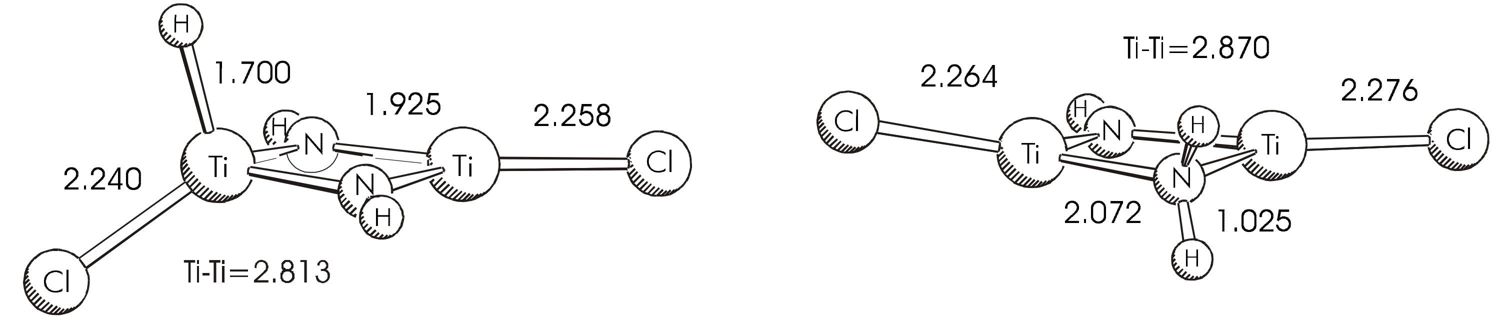

a) H on Ti

b) H on N

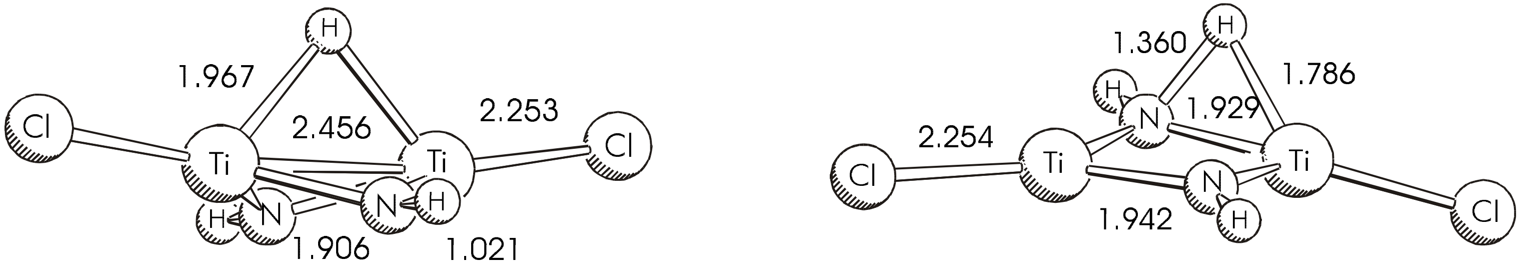

c) H above hollow

d) H above Ti-N bond

Fig. 5.4 H atom adsorption at (TiClNH)2 a) H adsorbed at Ti, b) H atom at N, c) H above hollow, d) H above Ti-N bond, TS in H migration between Ti and N.

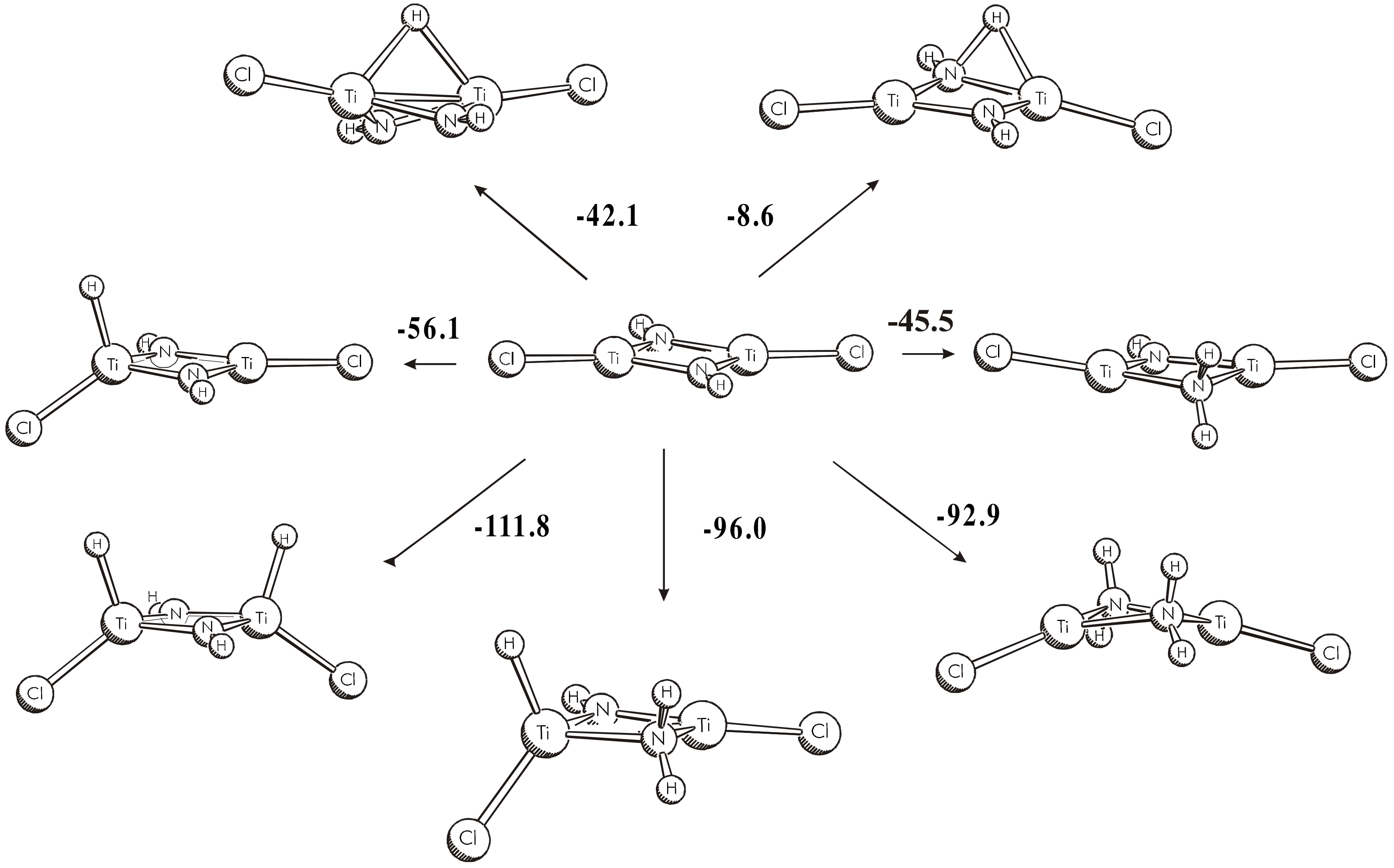

Fig.5.5 Calculated PW91 energies [kcal/mol] in adsorption of H atom at $(TiClNH)_2$.

According to the PW91 calculations the formation of two Ti-H bonds (Fig. 5.6a) is most favorable (Table 5.7, Fig. 5.5). The Ti-H bonds are slightly shorter and weaker than in case of one hydrogen adsorbed at Ti (Fig. 5.4a, Fig. 5.5). The distance between both Ti sites remains almost without change. Binding of one of the hydrogens to N atom is 16 kcal/mol less favorable (Fig. 5.5, Table 5.7) for the most stable structure and leads to an elongation of the Ti-H bond and significant shortening of the Ti-Ti distance (Fig. 5.6b). In the least favorable case of adsorption of both hydrogen atoms at N's, the second hydrogen atom is almost as strongly bonded as the first one (Fig. 5.5), with a slight elongation of the N-H bond to 1.028 Å. This structure is characterized additionally by the shortest Ti-Ti distance (Fig. 5.6c).

Table 5.7 Calculated bond lengths and adsorption energies for 2 hydrogen atoms at $(TiClNH)_2$.

H location	**r [Å]**	**E [kcal/mol]**
above Ti, Ti	1.691	111.8
above Ti, N	1.710, 1.024	96.0
above N, N	1.028	92.9

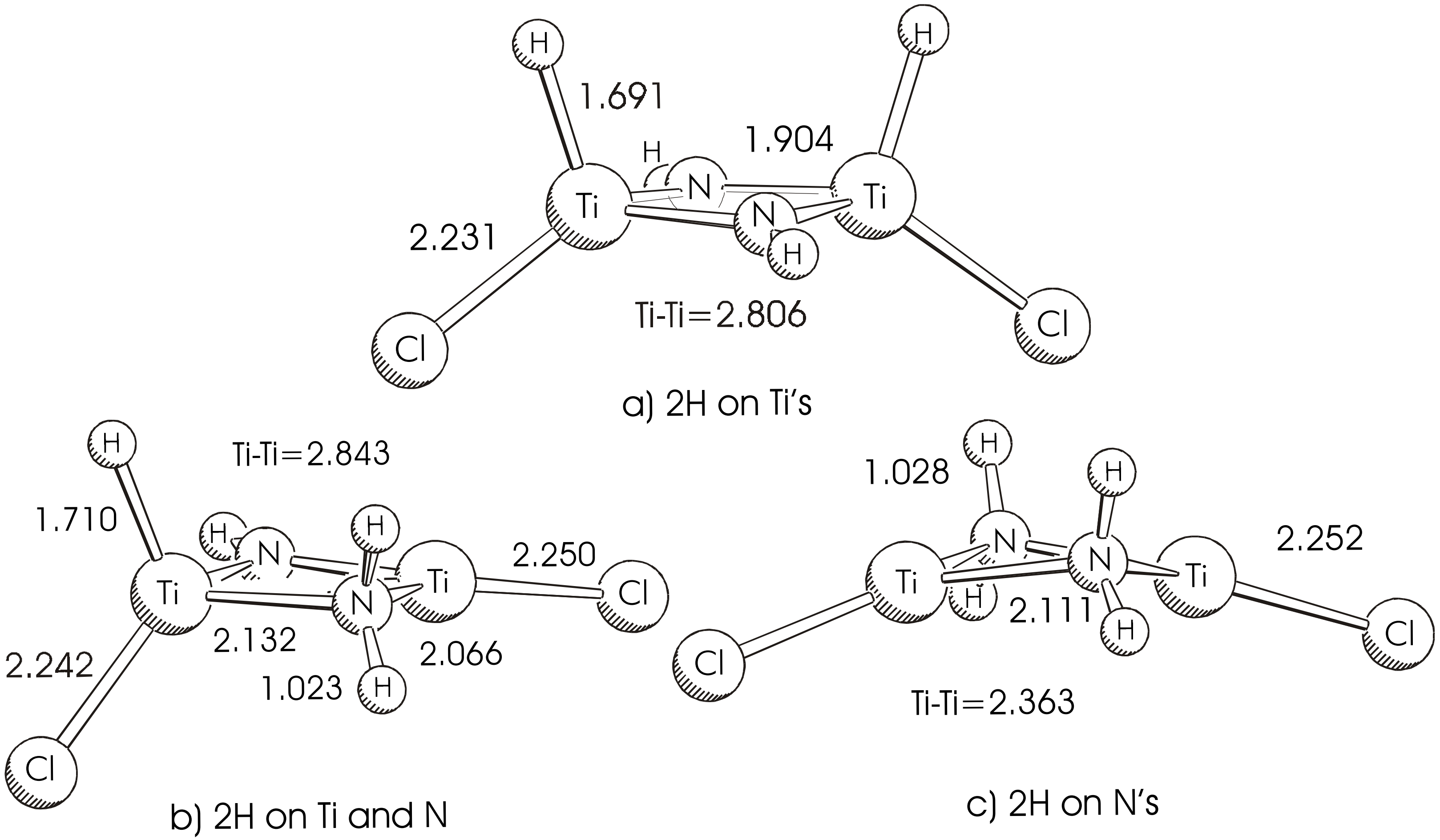

a) 2H on Ti's

b) 2H on Ti and N

c) 2H on N's

Fig. 5.6 Adsorption of two H atoms at $(TiClNH)_2$ a) both H atoms at Ti's, b) one H atom adsorbed at Ti, the other at N, c) bith H atoms at N's

5.4.2 Crystal (periodic slab) surface model

A slab with 5 layers, where 3 upper layers are relaxed was considered as a surface model in studies of hydrogen adsorption on the TiN surface. The size of the slab surface was chosen in the way that the hydrogens in neighboring cells are separated by 4.25 Å. This corresponds to a lower H coverage case. Higher coverage was approximated by two H atoms in one unit cell.

The surface study must include additional effect of the surface relaxation, which can have influence on bond lengths and adsorption energies. This effect was estimated by comparision of the results obtained for hydrogen adsorption at the frozen surface (all atoms are fixed at the positions taken from previously optimized (100) surface), and at the TiN surface, which relaxes according to the location of the adsorbed H atom. In the first case only the position of hydrogen was optimized, and in the case of the relaxing surface an optimization was performed for both hydrogen position and the surface structure.

According to the molecular study there are three possibilities to bind hydrogen atoms at the TiN surface. The calculated adsorption energies and corresponding bond lengths for adsorption at the frozen surface are presented in Table 5.8. The calculated energy of 51.3 kcal/mol for hydrogen adsorption at the Ti site is in a reasonable agreement with results obtained in the $(TiClNH)_2$ calculations. Adsorption at the Ti site is 2.4 kcal/mol more favorable than at the N site, which is much less than it was predicted by the molecular model. The calculated bond lengths of 1.74 Å and 1.05 Å for adsorption at Ti and N (Fig. 5.7) , respectively, are significantly longer when compared to the cluster study (Table 5.6). Location of H above the hollow at TiN surface is accompanied by about 15.5 kcal/mol smaller binding energy than adsorption at the top of the Ti binding site. The absolute values of adsorption energy of 35.8 kcal/mol is smaller than that provided by the molecular calculations (Table 5.6). The calculated distance to the surface of 1.5 Å is however comparable to cluster results.

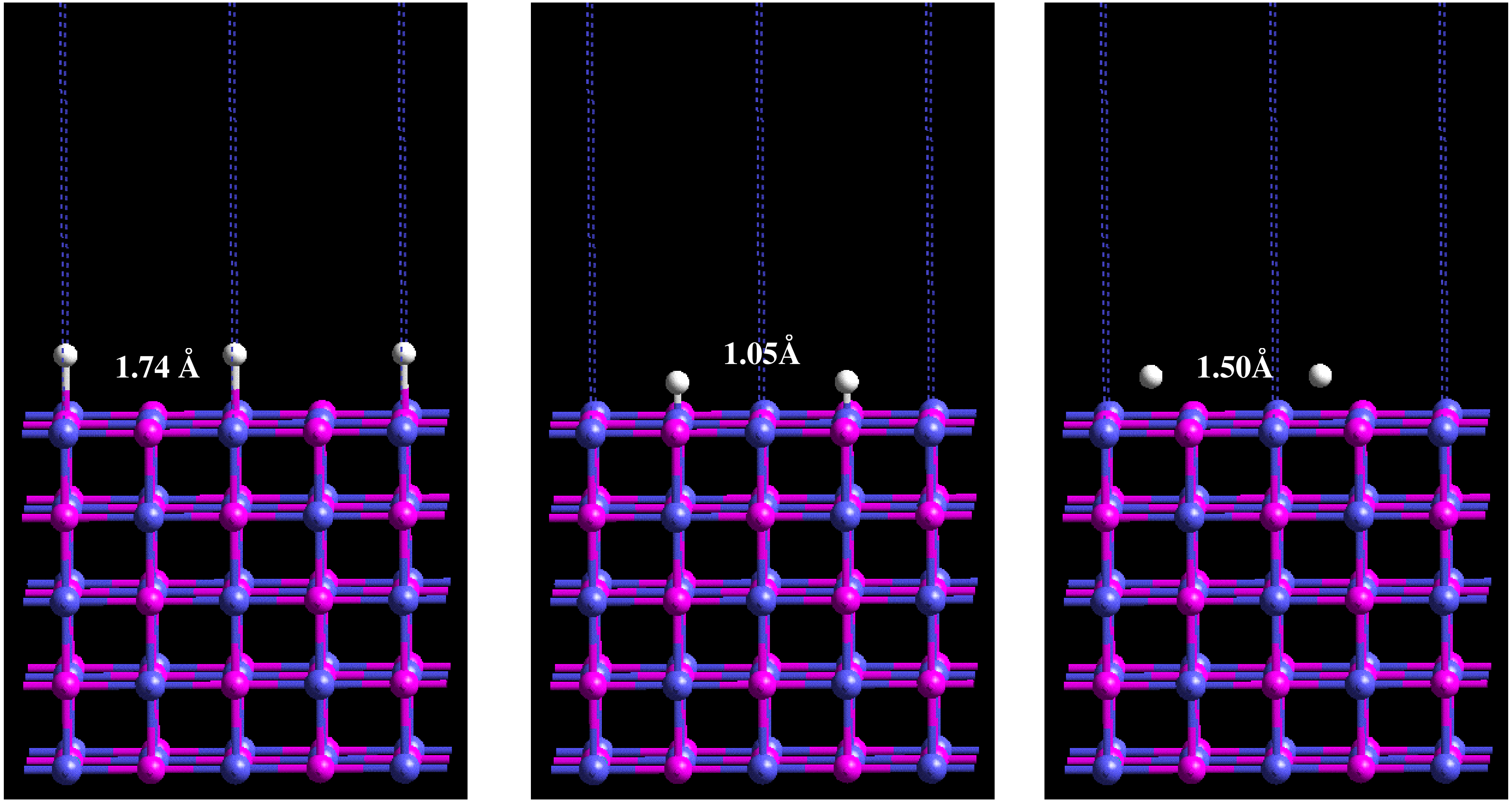

a) H at Ti site b) H at N site c) H above hollow

Fig. 5.7 Calculated bond lengths between H atom and an adsorption site at the static (100) TiN surface.

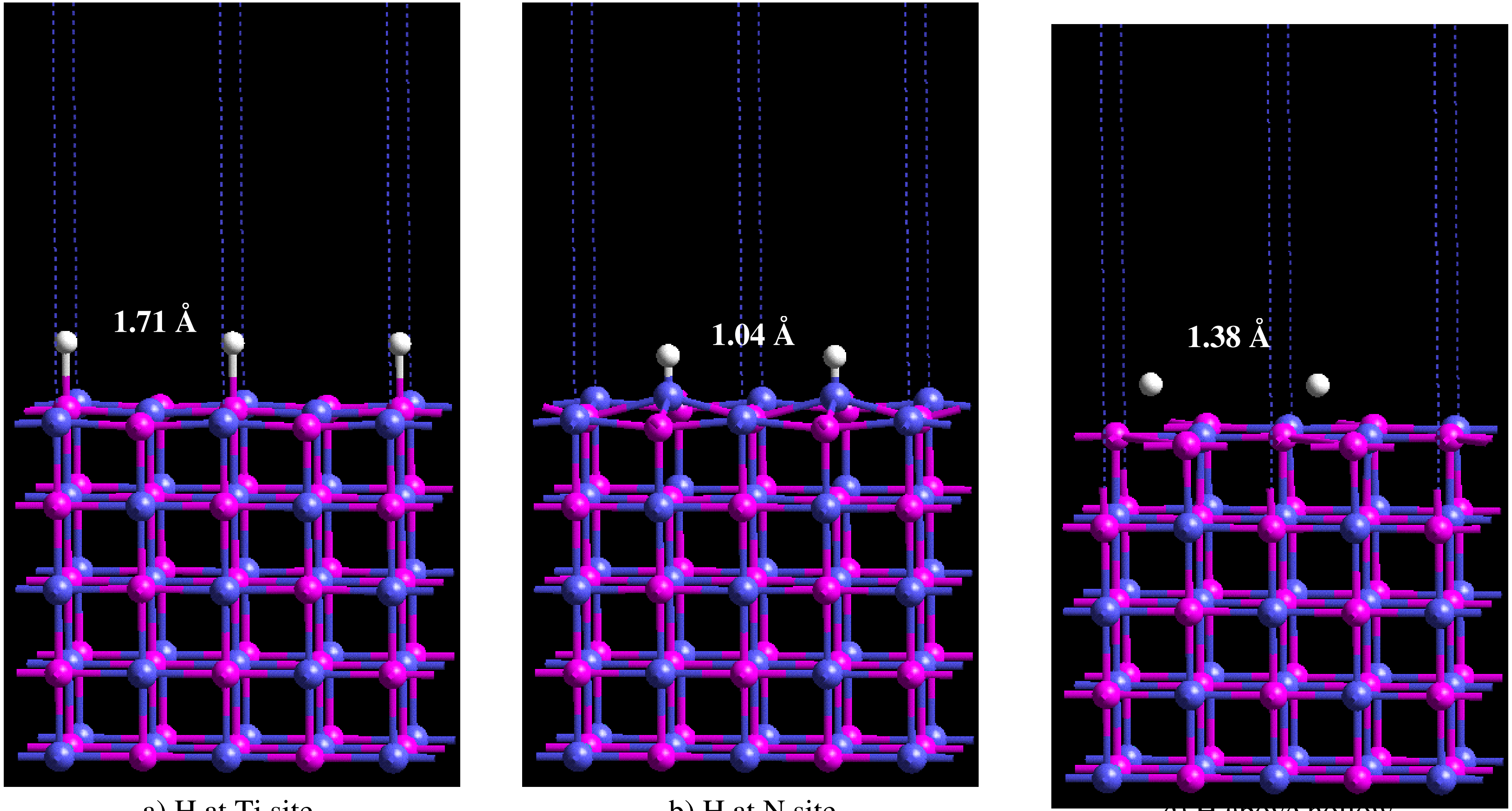

a) H at Ti site

b) H at N site

c) H above hollow

Fig. 5.8 Calculated bond lengths between H atom and an adsorption site at the relaxed (100) TiN surface.

As expected the relaxation of the surface increases the binding energy on all sites (Table 5.8) and reduces the differences between them. The global minimum at Ti has now an energy of 59.6 kcal/mol and the minimum at the N site is located only 1.7 kcal/mol higher (Fig. 5.8). A study of hydrogen chemisorption on TiN using a thermal conductivity detector at 900K and 950K gave an adsorption energy of 60.3 kcal/mol[106]. It is impossible with this experiment to select one binding site – Ti or N. Thus the exact deviation of the calculated energies from experimental data cannot be determined. The maximum deviation from experiment is however less than 3 kcal/mol. The Ti-H bond length is more influenced by the relaxation of the surface and is reduced to 1.71 Å, while the N-H length is almost not affected and equal to 1.04 Å. The calculated N-H bond matches the value calculated by Marlo et.al[103] and is in reasonable agreement with bond lengths characteristic for higher coordinated nitrogen in organometallic compounds - 1.047 Å.[107] The calculated Ti-H bond length of 1.71 Å is generally shorter than reported in the literature, being the closest to 1.768 Å measured for $C_{30}H_{35}Ti$.[108] Further comparison of the surface geometries (Fig.5.7, 5.8) and adsorption energies (Table 5.7, 5.8) shows that the nitrogen bonded to hydrogen relaxes more with a little change in the energy than titanium bonded to hydrogen. Since the distance of 3.01 Å between the Ti atoms in TiN is only slightly longer than the 2.95 Å of a Ti-Ti bond in the pure Ti crystal, nitrogen can be regarded as an interstitial type of defect (in scale of the whole TiN crystal as an "array of defects") in the slightly expanded titanium lattice. This implies that nitrogen can move in the perpendicular direction without much change in the energy.

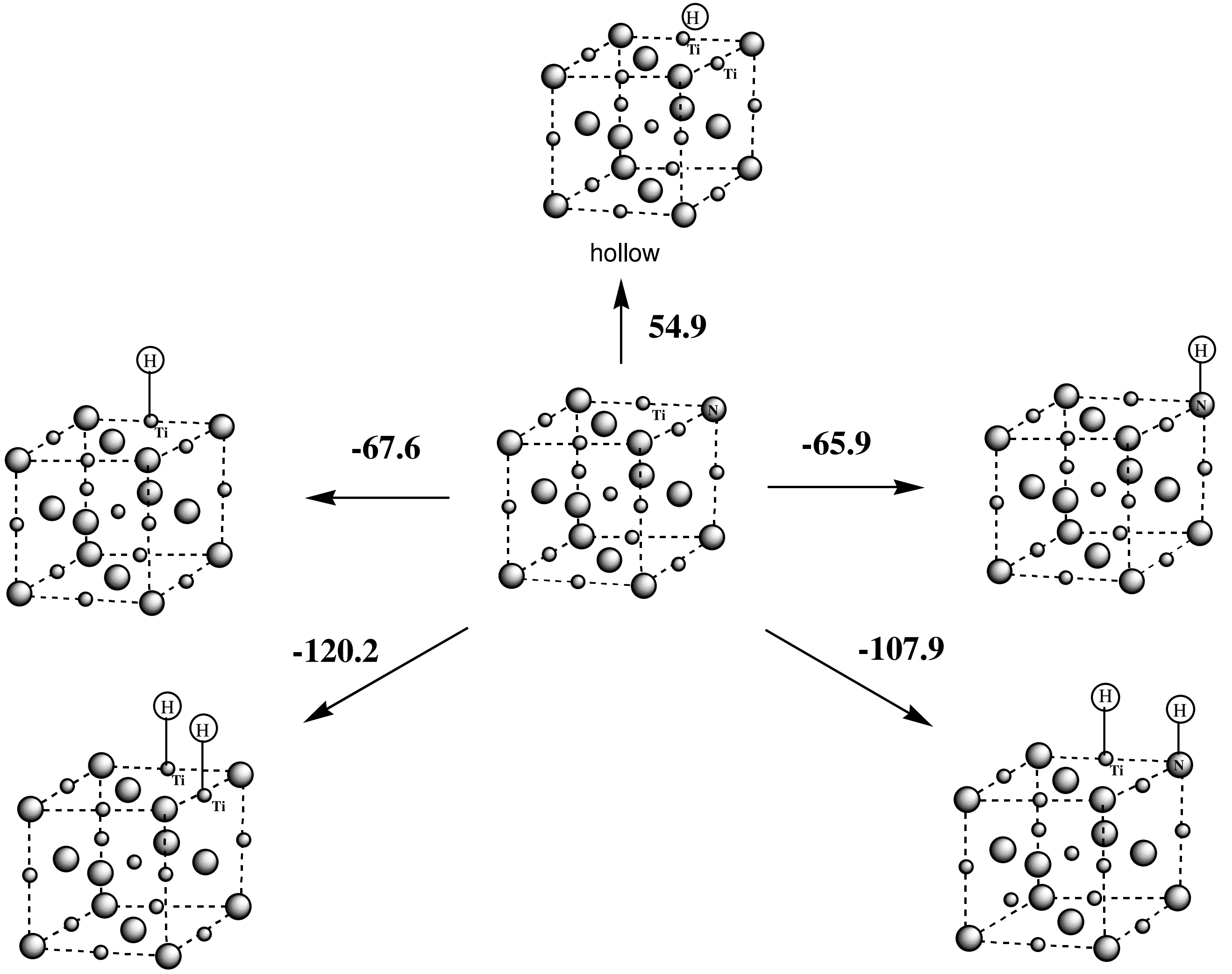

Fig. 5.9 Calculated PW91 energies in adsorption of H atom at relaxed (100) TiN surface.

Table 5.8 Calculated bond lengths and adsorption energies for hydrogen at the static and relaxed TiN surface. Bond lengths are given in Å and energies in kcal/mol.

	static	**relaxed**	**RPBE**[a)]
a (Ti-H)	1.74	1.71	1.76
E (Ti-H)	51.3	59.6	66.2
a (N-H)	1.05	1.04	1.04
E (N-H)	48.9	57.9	63.7
a (Ti-H) hollow	1.50	1.38	–
E hollow	35.8	46.9	–

[a)] see ref. 103

Adsorption of H atom above the hollow of the relaxed TiN surface is the strongest influenced by the relaxation of the surface atoms. The difference in adsorption energy to the global minimum with H at the top of the Ti site is reduced to 12.7 kcal/mol (Table 5.8) while the distance to the surface decreases to 1.38 Å.

Higher hydrogen coverage was approximated by two H atoms adsorbed within one unit cell. Since for a single hydrogen atom at the TiN surface the formation of the Ti-H bond provides the highest adsorption energy it is reasonable to assume that for two H atoms at least one Ti-H bond should be formed. Thus only two cases were considered: a) both H atoms are adsorbed at the Ti sites, b) one hydrogen is bounded to Ti and the other one to N. Corresponding structures are presented at Fig. 5.10. The calculated adsorption energies confirm that formation of the second Ti-H bond is > 12 kcal/mol more favorable than hydrogen adsorption at the N site (Fig. 5.9). The binding energy of the second hydrogen is 60.6 kcal/mol at the Ti site and 48.3 kcal/mol at the N site relative to the surface with one hydrogen atom adsorbed at Ti. Lowering the energy is connected with significant elongation of the Ti-H bond to 1.762 Å. The N-H bond length remains equal to 1.04 Å.

Table 5.9 Calculated bond lengths and adsorption energies for two hydrogen at relaxed TiN surface. Bond lengths are given in Å and energies in kcal/mol.

	a (Ti-H)	**a (N-H)**	**E**
H’s at two Ti’s	1.695	–	120.2
H at one Ti and one N	1.762	1.040	107.9

a)

b)

Fig.5.10 Calculated bond lengths in adsorption of two H atoms at relaxed (100) TiN surface: a) both H atoms at the Ti sites, b) one H atom at Ti, the other one at the N site.

5.5 Summary and Conclusions

The study shows that the non-local PW91 density functional can be applied in solid state calculations to reproduce the lattice constant and bulk modulus of the TiN crystal. The local PWC density functional overestimates the lattice constant significantly and thus cannot be used in the study of surface chemistry.

Calculations of surface energies confirm the experimental conclusion that the (100) TiN surface has the lowest and the (111) surface the highest surface energy.

The surface of TiN was found to exhibit complex relaxation which affects the surface processes. The energetically most favorable adsorption of H at Ti is influenced the least by the relaxation effect. The binding energy for this system increases from 51.3 kcal/mol to 59.6 kcal/mol under surface optimization. Binding of hydrogen to N at the relaxed surface is 1.7 kcal/mol weaker. The calculated N-H bond length remains almost the same, while the Ti-H bond becomes shorter under surface relaxation. The optimized surface geometries show that the nitrogen bonded to hydrogen relaxes more with a smaller change in energy than titanium bonded to hydrogen. This can be explained in terms of the interstitial type of atom in the slightly expanded titanium lattice and implies that the nitrogen can move in the perpendicular direction without significant changes in energy. Adsorption of hydrogen above the surface hollow is about 13 kcal/mol energetically less favorable than the global minimum with H adsorbed at the Ti site.

The calculations of the $(TiClNH)_2$ cluster as a model of the TiN surface provide adsorption energies which are smaller than those obtained in periodic calculations. All bond lengths between hydrogen and adsorption sites are however significantly shorter. The molecular model for H location above the Ti-N bond was assigned as the late transition state in migration of hydrogen from the energetically less favorable nitrogen site to the titanium site. The calculated barrier for this migration is 36.9 kcal/mol and thus this process was not considered in the periodic calculations.

Both periodic and molecular studies predict adsorption of two hydrogen atoms (higher H covarage) at the Ti sites to be energetically the most favorable. Adsorption of one of the hydrogens at the N site of the TiN surface reduces the binding energy by more than 12 kcal/mol.

6. Summary

This work presents theoretical study of initial processes in the CVD of Ta_2O_5 and TiN from $TaCl_5/H_2O$ and $TiCl_4/NH_3$, respectively. The mechanism of gas phase reactions and hydrogen adsorption at a TiN (100) surface was studied by means of quantum chemistry. Termodynamical equilibrium and kinetics of leading processes in $TiCl_4/NH_3$ system were calculated using the element-potential method and the model of a well-mixed reactor. The detailed summaries and conclusions to studied processes are given in the corresponding chapters.

The results presented in this work can be considered under three aspects: mechanism of the gas phase reactions, the surface processes and the performance of the applied theoretical approaches.

For the calculated gas phase reactions in CVD of Ta_2O_5 from $TaCl_5/H_2O$ and TiN from $TiCl_4/NH_3$ systems the following conclusions can be drawn:

1. Both hydration ($TaCl_5$) and ammonolysis ($TiCl_4$) reactions occur in the gas phase with a low or without any barrier.
2. $TaCl_5$ and $TiCl_4$ form strong (~23 kcal/mol) adducts with electron donors, H_2O and NH_3, respectively, with following consequences on the chemistry of these systems during the CVD process:

· formation of donor-acceptor complexes provides the driving chemical force in formation of transition metal compounds.

· at low temperatures (<500K) adducts are stable and may form precipitates on the CVD reactor walls.

· since the energies of the donor-acceptor adducts are intermediate between weak physical adsorption (~2.3 kcal/mol) and typical chemical bond energies (70-100 kcal/mol) they are supposed to determine the mechanism of surface reaction

3. The formation of Ta=O and Ti=N double bonds is strongly endothermic for a 1:1 initial composition of precursors. However it becomes energetically favorable in excess of H_2O and NH_3, respectively.
4. The calculations provide thermochemical data and spectral "finger prints" for the intermediate species and a mechanism of the chemical reactions relevant for CVD processes of the new materials Ta_2O_5 and TiN.
5. The calculations provide a characterization of experimentally unknown Ta oxochlorides, TaO_2Cl and $TaOCl_3$.
6. The presented mechanisms for the gas phase reactions in the TiN formation give an explanation for the experimentally observed incomplete ammonolysis of $TiCl_4$.

The results obtained for the TiN surface phenomena emphasize the importance of the surface relaxation. It is shown for a H atom adsorption at the TiN (100) surface that the binding energy increases upon surface relaxation by ~8 kcal/mol for the global adsorption minimum at the Ti site and >11 kcal/mol for the energetically least favorable adsorption above the surface hollow. The applied $(TiClNH_2)_2$ molecular model of the TiN surface was found to provide reasonably good estimates to both binding energies and bond lengths for the considered adsorption process. The calculated adsorption energies and bond lengths for the adsorption of hydrogen at the TiN (100) surface cannot be compared with experimental values because there are no experimental data available. However, the theoretical results for the TiN lattice constant a=4.25 Å and bulk modulus B=277 GPa, as well as surface energies are in reasonable agreement with the experimental parameters (a=4.24 Å, B=288GPa) and the results of other sophisticated theoretical studies.

There is no definite answer which of the methods applied in the gas phase reaction study provide the most reliable results. The Hartree-Fock approach is not suited for calculations of transition state energies, since it does not include correlation effects. Application of the sophisticated and computationally demanding CCSD(T) method was limited to single points energy calculations. These results were used as a reference for two other methods: MP2 and B3LYP. In case of the $TaCl_5/H_2O$ system, B3LYP energies were very close to the CCSD(T) results. However, for the $TiCl_4/NH_3$ system, MP2 provided a better agreement. In the solid state calculations the situation is more evident since the non-local PW91 density functional gives better agreement with experiment than the local PWC functional. Comparison of these two density functionals was done only for the computed TiN lattice constant and bulk modulus. The large deviation of the PWC lattice constant from the experimental value excluded this functional for studies of any surface phenomena.

Zusammenfassung

Die vorliegende Arbeit beschäftigt sich mit theoretischen Untersuchungen von Initialprozessen beim CVD von Ta_2O_5 und TiN aus $TaCl_5/H_2O$ bzw. $TiCl_4/NH_3$. Der Mechanismus der Gasphasenreaktionen und die Adsorption von Wasserstoff an der TiN (100) Oberfläche wurde mit Hilfe quantenchemischer Methoden untersucht. Thermodynamische Gleichgewichte und Kinetiken der führenden Prozesse im $TiCl_4/NH_3$ System wurde anhand der *element-potential*-Methode und des Modells des „well-mixed" Reaktors berechnet. Ausführliche Zusammenfassungen und Diskussionen der durchgeführten Untersuchungen dieser Prozesse finden sich in den entsprechenden Kapiteln.

Die Ergebnisse dieser Arbeit können unter drei verschiedenen Aspekten beleuchtet werden: der Mechanismus der Gasphasenreaktionen, die Prozesse an der Oberfläche des TiN-Festkörpers und die Qualität der theoretischen Näherungsmethoden.

Für die berechneten Gasphasenreaktionen beim CVD von Ta_2O_5 aus $TaCl_5/H_2O$ und TiN aus $TiCl_4/NH_3$ können mehrere Schlußfolgerungen gezogen werden:

1. Sowohl die Hydrations- ($TaCl_5$) als auch die Ammonolysereaktionen ($TiCl_4$) zeigen in der Gasphase nur kleine oder fast keine Barrieren.
2. $TaCl_5$ und $TaCl_4$ formen starke Verbindungen (≈ 23 kcal/mol) mit den Elektronendonoren H_2O bzw. NH_3. Dies hat folgende Konsequenzen für die Chemie dieser Systeme während des CVD-Prozesses:

· Die Bildung eines Donor-Akzeptor-Komplexes stellt die chemische Triebkraft bei der Bildung der Übergangsmetallverbindungen.

· Bei niedrigen Temperaturen (< 500 K) sind die Addukte stabil und fallen als Niederschlag an den Wänden des CVD Reaktors aus.

· Da die Energien der Donor-Akzeptor-Addukte zwischen der schwachen physikalischen Adsorption (≈ 2.3 kcal/mol) und den typischen Energien chemischer Bindungen (≈ 70 - 100 kcal/mol) liegen, wird vermutet, daß sie den Mechanismus der Reaktion an der Oberfläche bestimmen.

3. Die Bildung von Ta=O- und Ti=N-Doppelbindungen ist stark endothermisch, wenn die Reaktanden anfänglich in einem Verhältnis von 1:1 vorliegen. Die Reaktion wird jedoch bei einem Überschuß von H_2O bzw. NH_3 energetisch begünstigt.
4. Die Berechnungen liefern thermochemische Kenndaten und spektrale „Fingerabdrücke" der intermediären Spezies sowie Mechanismen der chemischen Reaktionen, die für die CVD Prozesse der neuen Materialien, Ta_2O_5 und TiN, relevant sind.
5. Die Berechnungen erlauben weiterhin die Charakterisierungen der experimentell unbekannten Ta-Oxochloride, TaO_2Cl und $TaOCl_3$.
6. Der gegebene Mechanismus für die Gasphasenreaktionen bei der Bildung von TiN erklärt den experimentellen Befund der unvollständigen Ammonolyse von $TiCl_4$.

Die für die TiN-Oberflächenphänomene erhaltenen Resultate unterstreichen die Bedeutung der Oberflächenrelaxation. Für die Adsorption eines H-Atoms an einer TiN (100) Oberfläche wird gezeigt, daß die Bindungsenergie aufgrund der Oberflächenrelaxation um ca. 8 kcal/mol für das globale Minimum der Adsorption an einem Ti-Platz ansteigt und um mehr als 11 kcal/mol für die energetisch weniger günstige Adsorption über der Oberflächen-Zwischenraum. Das benutzte molekulare $(TiClNH_2)_2$-Modell der TiN-Oberfläche führt zu guten Näherungen sowohl der Bindungsenergien als auch der Bindungslängen für die betrachteten Adsorptionsprozesse. Die berechneten Adsorptionsenergien und Bindungslängen bei der Adsorption von Wasserstoff an einer TiN (100) Oberfläche können nicht mit experimentellen Werten verglichen werden, da diese nicht verfügbar sind. Jedoch sind die theoretischen Werte für die TiN-Gitterkonstante a von 4.25 Å und dem Kompressionsmodul B von 277 GPa sowie die berechneten Oberflächenenergien in guter Übereinstimmung mit experimentellen

Parametern (a = 4.24 Å, B = 288 GPa) und den Ergebnissen anderer theoretischer Studien.

Es kann nicht definitiv entschieden werden, welche der für die Berechnung der Gasphasenreaktionen verwendeten Methoden die verläßlichsten Resultate liefert. Die Hatree-Fock Methode ist für die Berechnung von Übergangszuständen nicht geeignet, da sie keine Korrelationseffekte berücksichtigt. Die CCSD(T)-Methode wurde wegen des hohen Rechenaufwands nur für *single-point*-Energieberechnungen verwendet. Die so erzielten Ergebnisse dienten als Referenz für die Berechnungen nach dem MP2- und B3LYP-Verfahren. Im Fall des $TaCl_5/H_2O$-Systems lagen die mit der B3LYP-Methode berechneten Energien sehr nahe bei den mit dem CCSD(T)-Verfahren erzielten Ergebnissen; im Fall des $TiCl_4/NH_3$-Systems ergab MP2 die bessere Übereinstimmung. Bei den Festkörperberechnungen ist die Situation klarer, da die Deckungsgleichheit mit dem Experiment nach dem nicht-lokalen PW91-Dichtefunktional größer ist als nach der lokalen PWC-Methode. Der Vergleich der beiden Dichtefunktionale war hierbei beschränkt auf die Gitterkonstante des TiN-Festkörpers und den Bulk-Modulus. Aufgrund der großen Abweichung der mit dem PWC-Funktional bestimmten Gitterkonstante vom experimentellen Wert ist dieses Funktional für die Untersuchung von Oberflächenphänomenen ungeeignet.

References

[1] Sawyer, W.E., and Mann, A. *U.S. Patent*, **1880**, *229*, 335.

[2] Mond, L., Langer,C.; Quincke, F. *J. Chem. Soc.* **1890**, *57*, 749.

[3] Schrödinger, E. a) *Ann. Physik*, **1926**, *79*, 361 b) *ibid* **1926**, *80*, 437 c) *ibid* **1926**, *81*, 109.

[4] Born, M.; Oppenheimer, J.R. *Ann. Physik* **1927**, *84*, 457.

[5] Slater, J.C. *Phys. Rev.* **1929**, *34*, 1293 b) *ibid* **1930**, *35*, 509

[6] Eckart, C.E. *Phys. Rev.* **1930**, *36*, 878.

[7] (a) Hartree, D.R. *Proc. Camb. Phil. Soc*. **1928**, *24*, 89, (b) Fock, V. *Z. Phys*. **1930**, *61*, 161.

[8] (a) Roothaan, C.C *Rev. Mod. Phys.* **1951**, *23*, 69, (b) Hall, G.G. *Proc. R. Soc. London* **1951**, *A 205*, 541.

[9] Slater, J.C. *Phys. Rev*. **1930**, *36*, 57.

[10] Boys, S.F. *Proc. Roy. Soc.* **1950**, *A200*, 542.

[11] Cohen, M.L.; Heine, V. *Solid State Phys.* **1970**, *24*, 38.

[12] Löwdin, P.-O. *Rev. Modern Phys*. **1955**, *27*, 1509.

[13] Møller, C.; Plesset, M.S. *Phys. Rev.***1934**, *46*, 618. .

[14] Binkley, J.S.; Pople, J.A. *Int. J. Quantum Chem*. **1975**, *9S*, 229.

[15] (a) Cizek, J.; *J. Chem. Phys.* **1966**, *45*, 4256; (b) Pople, J. A.; Krishnan, R.; Schlegel, H.B.; Binkley, J.S. *Int. J. Quantum Chem.* **1978**, *14*, 545; (c) Bartlett, R.J.; Purvis, G.D. *Ibid.* **1978**, *14*, 561; (d) Purvis, G.D; Bartlett, R.J. *J. Chem. Phys.* **1982**, *76*, 1910; (e)

Raghavachari, K.; Trucks, G.W.; Pople, J.A.; Head-Gordon, M. *Chem. Phys. Lett.* **1989**, *157*, 479; (f) Bartlett, R.J.; Watts, J.D.; Kucharski, S.A.; Noga, J. *Ibid.* **1990**, *165*, 513.

[16] Brilloiun, L. *Actualities Sci. Ind.* **1934**, *71*, 159.

[17] Hohenberg, P.; Kohn, W. *Phys. Rev. B*, **1964**, *136*, 864.

[18] Kohn, W., Sham, L.J. *Phys. Rev.* **1965**, *140*, A1133.

[19] Becke, A.D. *J. Chem. Phys.* **1993**, *98*, 5648.

[20] Monkhorst, H.J.; Pack, J.D. *Phys. Rev. B*, **1976**, *13*, 5188.

[21] McKinley, K.A.; and Sandler, N.P. *Thin Solid Films*, **1996**, *290-291* , 440.

[22] Rausch, N.; Burte, N.P. *Microelectronics Journal,* 1993, 421.

[23] Treichel, H.; Mitwalsky, A.; Sandler, N.P.; Tribula, D.; Kern, W.; Lane, A.P. *Advanced Materials for Optics and Electronics,* **1992**, *1,* 299.

[24] Tanimoto, S.; Matsui, M.; Aoyagi, M.; Kamisako, K.; Kuroiwa, K.; Tarui, Y. *Jpn. J. Appl. Phys.* **1991**, *30,* L330.

[25] Zaima, S.; Furuta, T.; Yasuda, Y.; Lida, M. *J Electrochem Soc*, **1990**, *137* , 1297.

[26] Nishioka, Y.; Shinriki, H.; Mukai, K. *J. Electrochem. Soc.* **1987**, *134,* 410.

[27] Ingrey, S.J.; Westwood, Y.C.; Cheng, Y.C.; Wei, J. *Appl. Opt.* **1975**, *14,* 2194.

[28] Devine, R.A.B.; Chaneliere, C.; Autran, J.L.; Balland, B.; Paillet, P.; Leray, J.L. *Microelectron. Eng.,* **1997**, *36,* 61.

[29] Koyama, H.; Tanimoto, S.; Kuroiwa, K.; Tarui, Y. *Jpn. J. Appl. Phys.* **1994**, *33,* 6291.

[30] (a) Aarik, J.; Aidla, A.; Kukli, K.; Uustare, T. *J. Cryst. Growth,* **1994**, *75,* 180. (b) Kukli, K.; Aarik, J.; Aidla, A.; Kohan, O.; Uustare, T.; Sammelselg, V. *Thin Solid Films,*

1995, *260,* 135. (c) Simon, H.; Aarik, J. *J. Physique iV.* **1995**, *5,* C5-277. (d) Aarik, J.; Kukli, K.; Aidla, A.; Pung, L. *Appl. Surf. Sci.* **1996**, *103,* 331.

[31] The preliminary results were presented at E-MRS 1999 Spring Meeting in Strasbourg, 1-4 June 1999.

[32] (a) Møller, C.; Plesset, M.S. *Phys. Rev.***1934**, *46*, 618. (b) Binkley, J.S.; Pople, J.A. *Int. J. Quantum Chem.* **1975**, *9S*, 229.

[33] Becke, A.D. *J. Chem. Phys.* **1993**, *98*, 5648.

[34] Gaussian 98, Revision A.3, Frisch, M.J.;Trucks, G.W.; Schlegel, H. B.; Secures, G. E.; Robb, M. A.; Cheeseman, J. R.; Zakrzewski, V.G.; Montgomery, Jr. J. A.; Stratmann, R. E.; Burant, J. C.; Dapprich, S.; Millam, J. M.; Daniels, A. D.; Kudin, K. N.; Strain, M. C.; Farkas, O.; Tomasi, J.; Barone, V.; Cossi, M.; Cammi, R.; Mennucci, B.; Pomelli, C.; Adamo, C.; Clifford, S.; Ochterski, J.; Petersson, G. A.; Ayala, P. Y.; Cui, Q.; Morokuma, K.; Malick, D. K.; Rabuck, A. D.; Raghavachari, K.; Foresman, J. B.; Cioslowski, J.; Ortiz, J. V.; Stefanov, B. B.; Liu, G.; Liashenko, A.; Piskorz, P.; Komaromi, I.; Gomperts, R.; Martin, R. L.; Fox, D. J.; Keith, T.; Al-Laham, M. A.; Peng, C. Y.; Nanayakkara, A.; Gonzalez, C.; Challacombe, M.; Gill, P. M. W.; Johnson, B.; Chen, W.; Wong, M. W.; Andres, J. L.; Gonzalez, C.; Head-Gordon, M.; Replogle, E. S.; Pople, J. A., Gaussian, Inc., Pittsburgh PA, 1998.

[35] Hehre, W.J.; Radom, L.; Pople, J.A.; Schleyer, P.v.R. *Ab Initio Molecular Orbital Theory*, Wiley, 1986

[36] (a) Cizek, J.; *J. Chem. Phys.* **1966**, *45*, 4256; (b) Pople, J. A.; Krishnan, R.; Schlegel, H.B.; Binkley, J.S. *Int. J. Quantum Chem.* **1978**, *14*, 545; (c) Bartlett, R.J.; Purvis, G.D. *Ibid.* **1978**, *14*, 561; (d) Purvis, G.D; Bartlett, R.J. *J. Chem. Phys.* **1982**, *76*, 1910; (e) Raghavachari, K.; Trucks, G.W.; Pople, J.A.; Head-Gordon, M. *Chem. Phys. Lett.* **1989**, *157*, 479; (f) Bartlett, R.J.; Watts, J.D.; Kucharski, S.A.; Noga, J. *Ibid.* **1990**, *165*, 513.

[37] Hay, P.J.; Wadt, W.R. *J. Chem. Phys.* **1985**, *82*, 299.

[38] Bergner, A.; Dolg, M.; Kuechle; W., Stoll, H.; Preuss, H. *Mol. Phys.* **1993** ,*80*, 1413.

[39] Huzinaga, S. *Gaussian basis sets for molecular calculations*, Elsevier Amsterdam, Oxford, New York, Tokyo 1984.

[40] (a) Ditchfield, R.; Hehre, W.J.; Pople, J.A. *J. Chem. Phys.* **1971**, *54*, 724. (b) Hariharan, P.C.; Pople, J.A. *Theor. Chim. Acta* **1973**, *28*, 213. (c) Francl, M.M.; Pietro, W.J.; Hehre, W.J.; Binkley, J.S.; Gordon, M.S.; DeFrees, D.J.; Pople, J.A. *J. Chem. Phys.* **1982**, *77*, 3654.

[41] Russo, T.V.; Martin, R.L; Hay, P.J. *J. Phys. Chem.* **1995**, *99*, 17085.

[42] Ischenko, A.A.; Strand, T.G.; Demidov, A.V.; Spiridonov, V.P. *J. Mol. Struc*t. **1978**, *43*, 227.

[43] Kang, S.K.; Tang, H.; Albright, T.A. *J. Am. Chem. Soc.*, **1993**, *115*, 1971

[44] Benson, M.T.; Cundari, T.R.; Li, Yu; Strohecker, L.A. *Int. J. Quant. Chem.: Quant. Chem. Symp.* **1994**, *28,* 181.

[45] Deng, L.; Ziegler, T. *Organometallics* **1996**, *15,* 3011.

[46] (a) *Spectroscopic Properties of Inorganic and Organometallic Compounds.* (The Royal Society of Chemistry, Garden City Press Limited, London, 1984), Vol. 16, p.762. (b) Dobs, K.D.; Hehre, W.J. *J. Comput. Chem.* **1987**, *8,* 861. (c) Benson, M.T.; Cundari, T.R.; Lim, S.J.; Nguyen, H.D.; Pierce-Beaver, K. *J. Am. Chem. Soc.* **1994**, *116*, 3966. (d) Sosa, C.; Andzelm, J.; Elkins, B.C.; Wimmer, E.; Dobbs, K.D.; Dixon, D.A. *J. Phys. Chem.* **1992**, *96,* 6630. (e) Russo, T.V.; Martin, R.L.; Hay, P.J. *J. Chem. Phys.* **1995**, *102,* 9315.

[47] Rosenkilde, C.; Voyiatzis, G.; Jensen, V.R.; Ystens, M.; ∅stvold, T. *Inorg. Chem.* **1995**, *34,* 4360.

[48] (a) *Structure Data of Free Polyatomic Molecules*, Springer, Berlin **1987** (b) *Modern Organic Chemistry*, Marcel Dekker, New York, **1973**, p. 421.

[49] Figueira, R.R.; Fournier, L.L.; Varetti, E.L. *Spectrochim Acta Part A* **1982***, 38,* 965.

[50] Beattie, I.R.; Livingstone, K.M.S.; Reynolds, D.J.; Ozin, G.A. *J. Chem. Soc. A.* **1970**, 1210.

[51] Landis, C.R.; Cleveland, T.; Firman, T.K *J. Am.Chem.Soc*. **1995**, *117*, 1859.

[52] Del Bene, J.E.; Person, W.B.; Szczepaniak, K. *J. Phys. Chem.* **1995**, *99,* 10705.

[53] Chase, M.W. *NIST-JANAF Thermochemical Tables, Fourth Edition,, J.Phys.Chem. Ref. Data, Monograph 9,* 1998.

[54] Lubin, L.; Liting, Li, Tobin, J.M. *J. Am. Chem. Soc.* **1997**, *119,* 8574.

[55] Acho, J.A.; Doerrer, L.H.; Lipppard, S.J. Inorg. Chem. **1995**, *34*, 2542.

[56] (a) Zielinski, J.J.; Poirier, R.A.; Peterson, M.R.; Csizmadia, I.G. *J. Comput. Chem.* **1983**, *4*, 419. (b) Nguyen, M.T.; Ha, T.-K. *J. Am. Chem. Soc.* **1984**, *106*, 599. (c) Nguyen, M.T.; Hegarty, A.F.; *J. Am. Chem. Soc.* **1984**, *106*, 1552. (d) McKee, M.L. *J. Phys. Chem.* **1993**, *97*, 13608.

[57] Hoffman, D.M. *Polyhedron,* **1994**, *13,* 1169.

[58] (a) Nicolet, M.-A. *Thin Solid Films,* **1978**, *52,* 415. (b) Wittmer, M.; Studer, B.; Melchior, H. *J. Appl. Phys.,* **1981**, *52,* 5722. (c) Anamori, S. *Thin Solid Films,* **1986**, *136,* 195. (d) Park, K.C.; Kim, K.B., *J. Electrochem.* **1995**, *142,* 3109.

[59] Kurtz, S.R.; Gordon, R.G. *Thin Solid Films,* **1986**, *140,* 277.

[60] Raaijmakers, I.J. *Thin Solid Films,* **1994**, *247,* 85.

[61](a) Dubois, L.H.; Zegarski, B.R. *J. Electrochem.Soc.* **1992**, *139,* 3603. (b) Prybyla, J.A.; Chiang, C.-M.; Dubois, L.H. *J. Electrochem. Soc.* **1993**, *140,* 2695. (c) Weiller, B.H. *J. Am. Chem. Soc.,* **1996**, *118,* 4975.

[62] Musher, J.N.; Gordon, R.G. *J. Electrochem. Soc.* **1996**, *143,* 736.

[63] Lee, J.G.; Choi, J.H.; Lee, C.; Hong, J.H., Lee, E.G. *Jpn. J.Appl. Phys.,* **1998**, *37,* 6942.

[64] (a) Fowles, G.W.A. In *Progress in Inorganic Chemistry. Ed. Cotton, F.A. Vol. 6,* Interscience Publishers, NY 1964, p. 1. (b) Clark, R.J.H. In *Comprehensive Inorganic Chemistry, Vol. 3., Eds, Bailer, J.C.,Jr.; Emeleus, H.J.; Nyholm, R.; Trotman-Dickenson, A.F., 1973, p.355.*

[65] Saeki, Y.; Matsuzaki, R.; Yajima, A.; Akiyama, M. *Bull Chem.. Soc. Jpn,* **1982**, *55,* 3193.

[66] Allendorf, M.D.; Janssen, C.L.; Colvin, M.E.; Melius, C.F.; Niesen, I.M.B.; Osterheld, T.H.; Ho, P. *Electrochem. Soc. Proc. PV95-4,* Pennington, NJ, p. 393.

[67] Baboul, A.G., Schelegel, H.B. *J. Phys. Chem. B*, **1998**, *102*, 5152.

[68] Winter, C.H.; Sheridan, P.H.; Lewkebandra, T.S.; Heeg, M. J.; Proscia, J.W. *J. Am. Chem. Soc*. **1992**, *114*, 1095.

[69] Fix, R.M.; Gordon, R.G.; Hoffman, D.M. *J. Am. Chem. Soc* **1990**, *112*, 7833.

[70] Bergner, A.; Dolg, M.; Kuechle; W., Stoll, H.; Preuss, H. *Mol. Phys.* **1993** ,*80*, 1413.

[71] Huzinaga, S. *Gaussian basis sets for molecular calculations*, Elsevier Amsterdam, Oxford, New York, Tokyo 1984.

[72] Russo, T.V.; Martin, R.L; Hay, P.J. *J. Phys. Chem.* **1995**, *99*, 17085.

[73] (a) Ditchfield, R.; Hehre, W.J.; Pople, J.A. *J. Chem. Phys.* **1971**, *54*, 724. (b) Hariharan, P.C.; Pople, J.A. *Theor. Chim. Acta* **1973**, *28*, 213. (c) Francl, M.M.; Pietro, W.J.; Hehre, W.J.; Binkley, J.S.; Gordon, M.S.; DeFrees, D.J.; Pople, J.A. *J. Chem. Phys.* **1982**, *77*, 3654.

[74] R. J. Kee, F. M. Rupley, J. A. Miller, M. E. Coltrin, J. F. Grcar, E. Meeks, H. K. Moffat, A. E. Lutz, G. Dixon-Lewis, M. D. Smooke, J. Warnatz, G. H. Evans, R. S. Larson, R. E. Mitchell, L. R. Petzold, W. C. Reynolds, M. Caracotsios, W. E. Stewart, and P. Glarborg, Chemkin Collection, Release 3.5, Reaction Design, Inc., San Diego, CA (1999).

[75] Cotton, F.A.; Wilkinson, G. *Advanced Inorganic Chemistry. Fourth Edition.* Wiley: NY, 1980, p. 700.

[76] Fowles, G.W.A.; Pollard, F.H. *J. Chem. Soc.* **1953**, *527*, 2588.

[77] Kurtz, S.R; Gordon, R.G.; Thin Solid Films, **1986**, *140*, 277.

[78] Morino, Y.; Uehara, H. *J. Chem.Phys*, **1966**, *45*, 4543.

[79] Jonas, V.; Frenking, G., Reetz, M.T., *J. Comp. Chem.* **1992**, *13*, 919.

[80] Krömer, R.; Thiel, W. *Chem. Phys. Lett.* **1992**, *189*, 105.

[81] Sosa, C.; Andzelm, J.; Elkin, B.C.; Wimmer, E.; Dobbs, K.D.; Dixon, .D.A., *J. Phys. Chem.* **1992**, *96*, 6630.

[82] Cundari, T.R.; Gordon, M.S. *J. Am. Chem.Soc.***1993**, *115*, 4210.

[83] Haaland, A.; Rypdal, K.; Volden, H.V.; Andersen, R.A. *J.Am. Chem. Soc.,Dalton Trans.* **1992**, 891.

[84] Lappert, M.F.; Power, P.P.; Sangerand, A.R.; Srivasta, R.C., Metal and Metalloid Amides; Ellis Horwood: Chichester, 1980, p 475.

[85] Beste, A.; Krämer, O.; Fischer, A.; Frenking, G. *Eur. J. Inorg. Chem.* **1999,** 2037-2045.

[86] Wells, A.F.,Structural Inorganic Chemistry, Clarendon Press, Oxford, 1975.

[87] (a) Szczesniak, M.M.; Kurnig, I.J.; Scheiner, S. *J. Chem. Phys.***,** **1988**, *89*, 3131. (b) Del Bene, J.E. *J. Comput. Chem.* **1989**, *10,* 603. (c) Chiport, C.; Rinaldi, D.; Rivail, J.-L. *Chem. Phys. Lett.* **1992**, *191,* 287.

[88] Holbrook, K.A., Pilling, M.J. and Robinson, P.J. *Unimolecular Reactions*, London: Wiley-Interscience, 1972.

[89] Quack, M. and Troe, J. *Ber. Buns. Phys. Chem.* **1977**, *81*, 329

[90] Umanskii, S.Ya.; Novoselov, K.P.; Minushev, A.Kh.; Siodmiak, M.; Frenking, G.; Korkin, A.A.

[91] Baboul, A.G, Schlegel, B. *J. Phys. Chem. B* **1998**, *102*, 5152.

[92] Nugent, W.A., Mayer, J.M. Metal-Ligand Mulitple Bonds, Wiley, New York, 1988.

[93] Cross, J.B. and Schlegel, H.B. , *Chem. Mater.* **2000**, *12,* 2466.

[94] a) Gasser, R.P.H. An Introduction to Chemisorption and catalysis by metals, Oxford University Press, New York, 1985. b) Somorjai, G.A., Introduction to Surface Chemistry and Catalysis, Wiley, New York, 1994.

[95]Pedrew, J.P., and Wang, Y., *Phys. Rev.* **1992**, *B 45*, 13244.

[96] Pewdrew, J.P.; Chevary, J.A.; Vosko, S.H.; Jackson, K.A., Pederson, M.R., Singh, D.J:, Fiolhais, C. *Phys. Rev.* **1992**, *B 46*, 6671.

[97] M. Dolg, U. Wedig, H. Stoll, H. Preuss, *J. Chem. Phys.* **1987**, *86*, 866.

[98] a) Delley, B., *J. Chem. Phys.* **1990**, *92*, 508 b) Delley, B. *ibid.* **1991**, *94*, 7245 c) Delley, B., *J. Phys. Chem.* **1996**, *100*, 6107.

[99] Neckel, A. in The Physics and Chemistry of Carbides, Nitrides and Borides, edited by R. Freer, Kluwer Academic, New York, 1990, p. 485

[100] Schoenberg, N., *Acta Chemica Scandinavica* **1954**, *8*, 213

[101] Pedrew, J.P., and Wang, Y., *Phys. Rev.* **1992**, *B 45*, 13244

[102] Gubanov, V.A.; Ivanovsky, A.L., and Zhukov, V.P., Electronic Structure of Refractory Carbides and Nitrides, Cambridge Univ. Press, 1994.

[103] Marlo, M., and Milman, V., *Phys. Rev.* In press.

[104] Zhao, J.P.; Wang, X.; Chen, Z.Y., Yang, S.Q.; Shi, T.S., Liu, X.H. *J.Phys. D*. **1997**, *30*, 5.

[105] Diedenhofen, M. MSc. Thesis, Fachbereich Chemie, Philipps-Universität Marburg, 1997.

[106] You, M.S.; Nakanishi, N., and Kato, E., *J. Electrochem. Soc.* **1991**, *138*, 1394.

[107] Hussain, M.S., and Schlemper, E.O., *Inorg. Chem.* **1979**, *18*, 2275.

[108] de Wolf, J.M.; Meetsma, A., and Teuben, J.H., *Organometallics* **1995**, *14*, 5466.

---

[94] a) Gasser, R.P.H. An Introduction to Chemisorption and catalysis by metals, Oxford University Press, New York, 1985. b) Somorjai, G.A., Introduction to Surface Chemistry and Catalysis, Wiley, New York, 1994.

[95]Pedrew, J.P., and Wang, Y., *Phys. Rev.* **1992**, *B 45*, 13244.

[96] Pewdrew, J.P.; Chevary, J.A.; Vosko, S.H.; Jackson, K.A., Pederson, M.R., Singh, D.J:, Fiolhais, C. *Phys. Rev*. **1992**, *B 46*, 6671.

[97] Dolg.M, Wedig, U.; Stoll, H.; Preuss, H. *J. Chem. Phys.* **1987**, *86*, 866.

[98] a) Delley, B., *J. Chem. Phys.* **1990**, *92*, 508 b) Delley, B. *ibid.* **1991**, *94*, 7245 c) Delley, B., *J. Phys. Chem.* **1996**, *100*, 6107.

[99] Neckel, A. in The Physics and Chemistry of Carbides, Nitrides and Borides, edited by R. Freer, Kluwer Academic, New York, 1990, p. 485

[100] Schoenberg, N., *Acta Chemica Scandinavica* **1954**, *8*, 213

[101] Pedrew, J.P., and Wang, Y., *Phys. Rev.* **1992**, *B 45*, 13244

[102] Gubanov, V.A.; Ivanovsky, A.L., and Zhukov, V.P., Electronic Structure of Refractory Carbides and Nitrides, Cambridge Univ. Press, 1994.

[103] Marlo, M., and Milman, V., *Phys. Rev.* In press.

[104] Zhao, J.P.; Wang, X.; Chen, Z.Y., Yang, S.Q.; Shi, T.S., Liu, X.H. *J.Phys. D*. **1997**, *30*, 5.

[105] Diedenhofen, M. MSc. Thesis, Fachbereich Chemie, Philipps-Universität Marburg

[106] You, M.S.; Nakanishi, N., and Kato, E., *J. Electrochem. Soc.* **1991**, *138*, 1394.

[107] Hussain, M.S., and Schlemper, E.O., *Inorg. Chem.* **1979**, *18*, 2275.

[108] de Wolf, J.M.; Meetsma, A., and Teuben, J.H., *Organometallics* **1995**, *14*, 5466.